# UNIVERSIDAD NACIONAL AUTÓNOMA DE MÉXICO
PROGRAMA DE MAESTRÍA Y DOCTORADO EN INGENIERÍA
ENERGÍA-PROCESOS Y USO EFICIENTE DE ENERGÍA


## GENERADOR ELÉCTRICO MAGNETOHIDRODINÁMICO PARA EL APROVECHAMIENTO DE LA ENERGÍA DE OLEAJE


**TESIS**
QUE PARA OPTAR POR EL GRADO DE:
**DOCTOR EN INGENIERÍA**


PRESENTA:
**JOSÉ CARLOS DOMÍNGUEZ LOZOYA**


TUTOR PRINCIPAL:
**DR. SERGIO CUEVAS GARCÍA**, IER-UNAM


COMITÉ TUTOR:
DR. EDUARDO RAMOS MORA, IER-UNAM
DR. RODOLFO SILVA CASARÍN, FACULTAD DE INGENIERÍA, UNAM
DR. RAÚL ALEJANDRO ÁVALOZ ZÚÑIGA, CICATA-IPN
DR. ALDO FIGUEROA LARA, UAEM


CIUDAD DE MÉXICO, FEBRERO 2019

**JURADO ASIGNADO:**

Presidente:        Dr. Eduardo Ramos Mora

Secretario:        Dr. Rodolfo Silva Casarín

Vocal:        Dr. Sergio Cuevas García

1$^{er.}$ suplente:        Dr. Aldo Figueroa Lara

2$^{do.}$ suplente:        Dr. Raúl Alejandro Ávaloz Zúñiga

Lugar o lugares donde se realizó la tesis: Instituto de Energías Renovables (IER-UNAM)

### TUTOR DE TESIS

Dr. Sergio Cuevas García

_____

**FIRMA**

# Resumen

En este trabajo se presenta el estudio teórico y experimental de la dinámica de flujo y el comportamiento eléctrico de un generador alterno magnetohidrodinámico (MHD) de metal líquido que tiene el potencial de aprovechar la energía del oleaje marino para su conversión en energía eléctrica. El principal propósito de esta tesis es la comprensión y el modelado físico de los fenómenos ocurridos en los generadores alternos MHD, así como el diseño, construcción y caracterización experimental de un prototipo de generador MHD a escala de laboratorio. Se presenta un panorama general de la energía del oleaje marino y las diferentes tecnologías para aprovecharla, enfatizando el potencial de los generadores MHD. Desde el punto de vista teórico se explora analíticamente mediante un tratamiento bidimensional el flujo del metal líquido dentro del generador alterno MHD en las zonas de campo magnético uniforme y no uniforme. Asimismo se utiliza el modelo analítico para analizar el comportamiento eléctrico del generador MHD. En el aspecto práctico, se presenta el diseño del prototipo de un generador alterno MHD de metal líquido haciendo una descripción detallada de los sistemas que lo componen (sistema impulsor, ducto de oscilación, sistema de medición y complementos). Posteriormente se describen las condiciones experimentales de interés y las técnicas utilizadas para realizar la caracterización del flujo y el comportamiento eléctrico del generador MHD. Más adelante se muestran los resultados experimentales del flujo para las diferentes condiciones de operación obtenidos mediante la técnica de Velocimetría Doppler Ultrasónica. También se muestran los resultados experimentales del comportamiento eléctrico del generador MHD para diferentes condiciones de operación. Con el fin de caracterizar el generador en condiciones de operación más realistas, se presenta un diseño a escala laboratorio de un generador alterno MHD de metal líquido acoplado a un convertidor de energía de oleaje que se pretende probar en un canal de olas. Finalmente se presentan las conclusiones de este trabajo.
.

# Abstract

In this work, the theoretical and experimental study of the flow dynamics and the electrical behavior of an alternate liquid metal magnetohydrodynamic (MHD) generator that has the potential to harness the energy of the marine waves for its conversion into electrical energy is presented. The main purpose of this thesis is the understanding and physical modeling of the phenomena occurring in the alternate MHD generators, as well as the design, construction and experimental characterization of a MHD generator prototype at laboratory scale. An overview of the energy of the marine waves and the different technologies to harness it, emphasizing the potential of the MHD generators is presented. From the theoretical point of view, the flow of the liquid metal inside the alternate MHD generator in the regions of uniform and non-uniform magnetic field is analytically explored by means of a two-dimensional treatment. The analytical model is also used to analyze the electrical behavior of the MHD generator. In the practical aspect, the design of the prototype of an alternate liquid metal MHD generator is presented, making a detailed description of the systems that compose it (impeller system, oscillation duct, measurement system and complements). Subsequently, the experimental conditions of interest and the techniques used to perform the characterization of the flow and the electrical behavior of the MHD generator are described. Later the experimental flow dynamics results for the different operating conditions obtained by the Ultrasonic Doppler Velocimetry technique are shown. The experimental results of the electrical behavior of the MHD generator for different operating conditions are also shown. In order to characterize the generator under more realistic operating conditions, a laboratory-scale design of an alternate liquid metal MHD generator coupled to a wave energy converter (WEC) that is intended to be tested in a wave channel is exposed. Finally, the conclusions of this work are presented.

# Contents

# List of Figures

# Introduction

The increasing population as well as changes in the lifestyle and greater comfort of a big part of humanity have led over the years to a significant increase in the energy consumption in the world. To supply the energy demands, nowadays the main source of energy comes from fossil fuels, such as coal, oil and natural gas, which although are available and relatively cheap, they are finite and may be exhausted soon. In addition, a side effects of the use of these fuels is the release of greenhouse gases in the combustion process which are harmful to the life on the planet. As greenhouse gases are the main responsible for global warming and climate change, it is expected that the replacement of fossil fuels by renewable energies sources will help to mitigate the emissions of greenhouse gases and to fight against climate change. For each source of renewable energy, say solar, eolic, ocean, gheothermal and bio energy, appropriate technologies have been developed or are under development to harvest and transform the energy for useful purposes [1]. Figure 1 shows a diagram of renewable energies and their different technologies. Electricity from renewable energies can be obtained from solar energy through photovoltaics and concentrating solar power, geothermal energy, hydro energy, wind energy, bioenergy and ocean energy. Renewable heat sources include geothermal heat, bioenergy, solar thermal heat and ocean thermal energy. From a technological perspective geothermal, hydroelectric and solar photovoltaic applications are among the most highly developed while others such as ocean energy technologies, in particular wave energy, are emerging from the research and development phase. Due to the huge potential of ocean energy it is of great importance to increase the efforts to achieve the application of these technologies in the short term.

Ocean waves are created by wind, which is a product of the atmosphere redistribution of solar energy. The wind interacts with the surface of the ocean generating ripples, which increase in size due to the sustained energy input [2]. Figure 2 shows a sketch of the generation of ocean waves. In fact, deep-water waves can travel thousands of kilometers without practically losing energy. On the other hand, when a wave approaches the coast (shallow water), energy losses appear, mainly due to the friction with the bottom of the sea and the breaking of the wave, so that a fraction of the wave energy reaches the shore [3]. The power density available in the waves is much larger than the wind and solar power densities [3, 4]. Waves can build up over oceanic distances to power densities averaging over $1 \times 10^5$ W/m

15
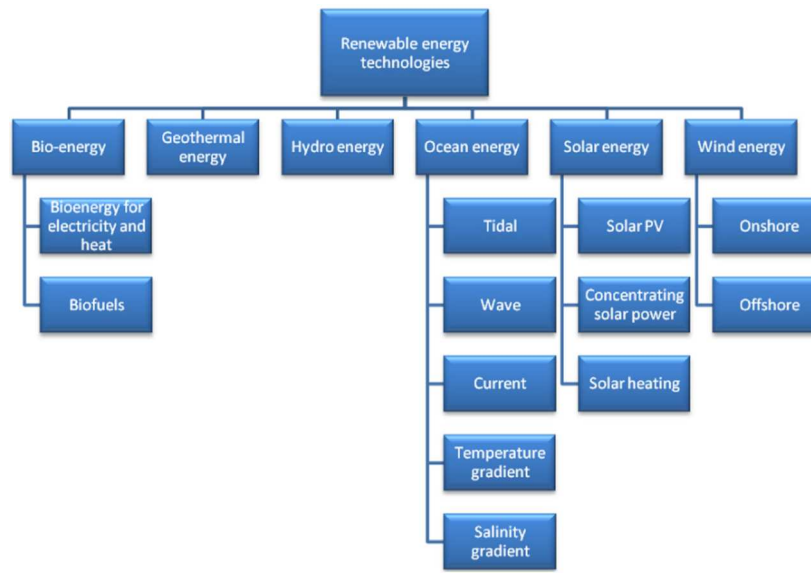
Fig. 1: Renewable energy sources and technologies [1] .

(note that the measure is power per meter width of wave front). Recent estimates indicate that the global wave energy potential of oceans is 32 PWh/yr, which is roughly equivalent to twice the world electricity supply in 2008 which was 17 PWh/yr [5, 6]. Due to the nature
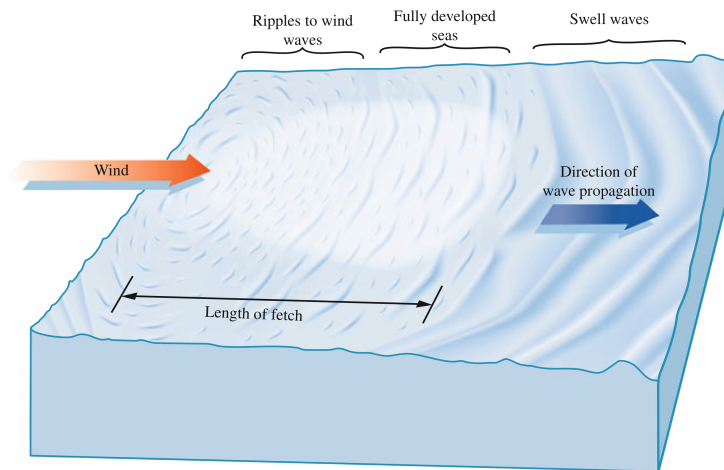


Fig. 2: The generation of ocean waves [2].

of marine waves, the largest wave power density is found in areas near the poles, above the Tropic of Cancer and below the Tropic of Capricorn (temperate zones). Figure 3 shows the global distribution of annual mean wave power density estimates in kW/m. Although the data shown in the figure are annual averages, in terms of consistency of wave resource is important to mention that the power density can vary in some regions drastically among

seasonal weathers. An important fact is that in the northern hemisphere winds are significantly less consistent than the winds in the southern hemisphere, so that the wave power density is much more variable [7, 8, 9].
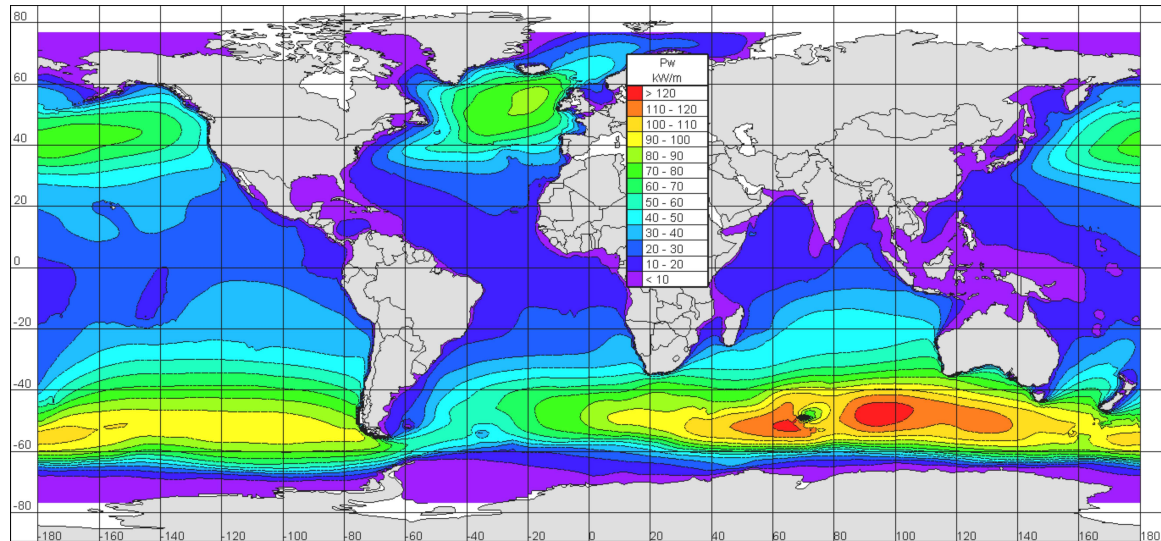


Fig. 3: Global distribution of annual mean wave power [7].

With the aim of harvesting the energy of the waves to be transformed into useful energy, different wave energy converter (WEC) designs have been proposed. Historically, the first patent of a wave converter dates from 1799 when the French Pierre-Simon Girard obtained a patent for a machine that mechanically captured the energy of the ocean waves [10]. The pionner of the modern WECs technology is Yoshio Masuda, who in 1940 developed the first floating oscillating water column incorporated into a navigation buoy [11]. Since then, different devices have been proposed, each one being defined by a particular design and power conversion system, which transforms the energy absorbed by the WEC into electricity. One of the main ways in which WECs are classified is by location zone, which corresponds to shoreline, nearshore and offshore. The shoreline clasification means that the location of the device is on the coast. The term nearshore corresponds to places relatively close to the shoreline, with water depths no greater than 50 meters. The offshore term means depth of water greater than 50 meters [10, 12, 13]. Therefore the principal devices can be characterized as belonging to six types, which are Point absorber (PA); Attenuator; Submerged pressure differential (SPD); Overtopping device (OD); Oscillating water column (OWC) and Oscillating wave surge converter (OWSC) (see fig. 4). In Titah et al (2015), a map showing the main classes of WECs and their location zone is provided. Another way to classify WECs is through the power conversion system. Roughly, they can be classified into two categories, direct conversion and indirect conversion. Power direct conversion systems transform the energy captured by the WECs into useful energy in a

Point absorber                          Attenuator                              SPD



Overtopping device                 Oscillating water colum                    OWSC
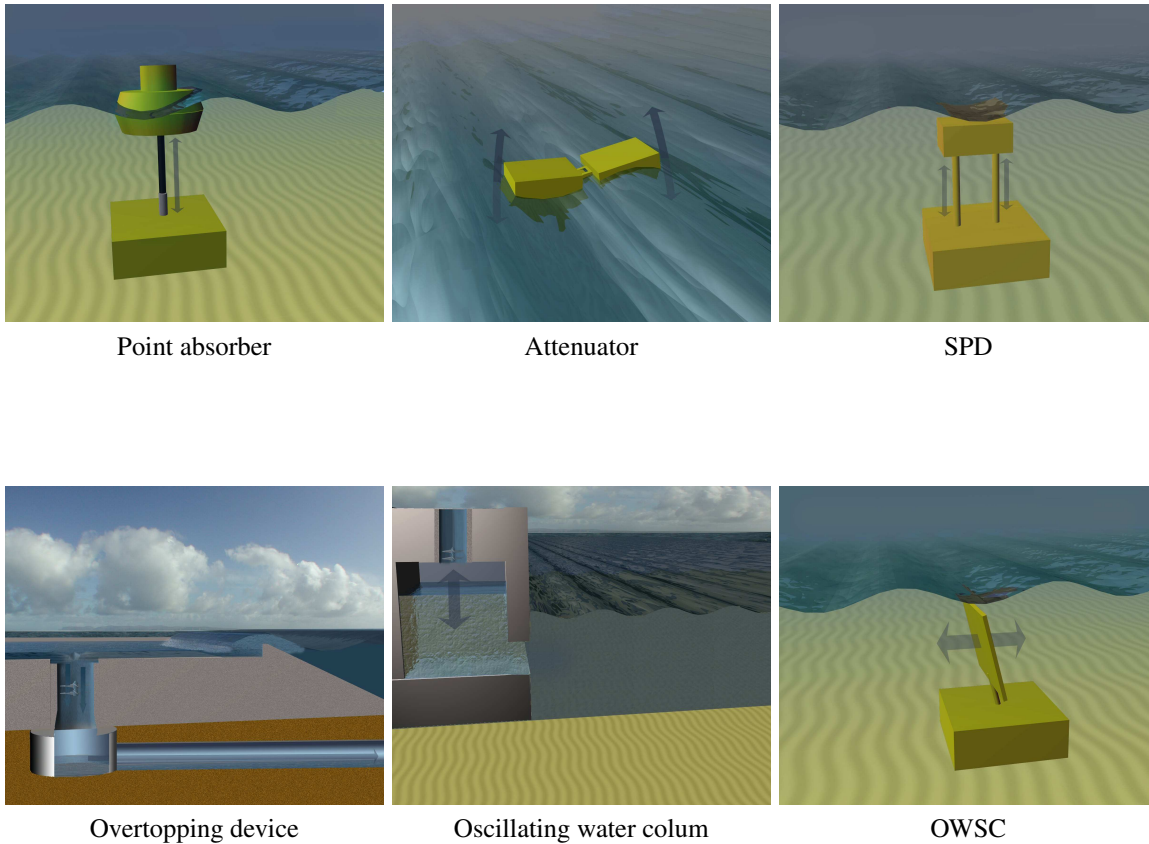
Fig. 4: Main classes of WECs [ © European Marine Energy Centre].

single step, for instance, the linear electric generator. On the other hand, power indirect conversion systems transform the energy coming from the WECs in two or more steps, for example, a system of air turbine coupled with a rotary electric generator is used to transform the energy captured by an oscillating water colum into electricity [14, 15, 16]. In some cases, such as point absorber and submerged pressure differential systems, where a linear reciprocal movement is obtained, it is convenient to use a direct energy conversion system, because the nature of the movement of the WECs fits perfectly with the movement of the direct energy conversion system. Currently, the vast majority of the designs and prototypes of WECs use indirect power generation systems, due to the infrastructure and technological development based on the use of rotatory generators. The major drawback of the indirect power generation system is that the overall system efficiency is affected by the turbines, gearboxes or hydraulic system used to couple the low frequency movement of ocean waves with the high frequency movement of the rotary generator. As a result, the power conversion systems are bulky and expensive. On the other hand, the power direct conversion systems reduce the mechanical complexity and therefore the overall system efficiency im-

proves. Power direct conversion system are characterized by a big force (depending on the size of the wave energy converter) and a low frecuency that match with the low frecuency of the wave. In terms of wave energy there are very few variants of direct power conversion systems. In a global context, almost all of the direct power conversion system devices are based on linear generators and their variants, which have great engineering and technological challenges, such as a high attractive force between translator and stator. This complicates the mechanical and the bearing designs [17, 18, 19, 20]. An alternative way to obtain useful energy from the WECs in a single step is to use a magnetohydrodynamic (MHD) generator. Although both linear generators and MHD generators have the same operating principle and are based on the use of permanent magnets, the main difference between them is that the induced current and voltage in the MHD generators are generated in an electrically conducting fluid instead of a solid conductor.

Magnetohydrodynamics (MHD) is the branch of physics which combines the subjects of fluid dynamics and electromagnetism to study the behavior of electrically conducting, non-magnetizable fluids interacting with magnetic fields. In nature, these kind of phenomena appear in a wide range of situations from geophysical phenomena, like the dynamo effect which originates the Earth's magnetic field, to the formation and evolution of stars and galaxies [21, 22]. From the technological point of view, MHD is applied in many technological developments, where electrically conducting working fluids are employed, for instace, ionized gas (plasma), liquid metals, electrolytes and molten salts. Electromagnetic effects can be used to control, stir, pump or levitate conducting fluids as well as for heat transfer enhancement or the generation of electric power.

An MHD generator is a device that converts the kinetic energy of an electrically conducting fluid, for instance a liquid metal, into electrical energy through the interaction with a static magnetic field. A common MHD generator consists of a duct with a rectangular cross-section immersed in a static magnetic field that is transversal to a pair of insulating walls. The walls parallel to the applied field are electrical conductors (electrodes). When a conducting fluid flows inside the duct, its motion within the imposed magnetic field induces an electric current perpendicular to both the fluid motion and the applied field that can be extracted through the electrodes connected to an external load. If the fluid motion is unidirectional, a DC current is induced while, if the fluid carries out an oscillatory motion, an AC current is generated. In this way, the kinetic energy of the fluid is converted directly into electric energy without the need of mechanical parts. Many research programs on MHD generation have been developed in different countries since the last century. MHD plasma generators received much attention for the production of electric energy at large scale although, among other technical problems, the requirement of working at high temperatures imposed severe restrictions in their development [23]. In turn, liquid metal MHD (LMMHD) generators were considered since the sixties as an alternative for energy production in the space [24]. In the seventies and eighties this technology was also explored

with the aim of developing small energy conversion systems that could use solar and low temperature heat sources [25]. Although at large scale MHD generators have not reached a definitive assessment, at small scale are considered as valuable options for specific applications due to particular advantages. For instance, alternate LMMHD generators avoid global fluid circulation and may be coupled to different sources of mechanical energy, such as thermoacoustic engines or WECs [26, 27, 28]. In the late eighties a proposal was made at Los Alamos National Laboratory to transform acoustic power into electrical power through a liquid metal MHD acoustic transducer [29]. In these devices, the thermoacoustic effect is used to generate an oscillatory motion of a conducting fluid in a duct immersed in an applied transverse magnetic field [30, 31, 32]. Alternate liquid metal MHD generators were later proposed to convert the oscillatory motion of ocean waves into electricity. In 1992 reciprocating magnetohydrodynamic generator for wave energy was first proposed by Rynne [33], where sea water passes through a duct under the presence of permanent magnets. The problem with this concept is that the conductivity of the sea water is extremly low compared with metals, so that the power output is very small. In 2005 Koslover patented a LMMHD power generation system coupled to a WEC and also performed the theoretical analysis about how to obtain the maximum power output [34]. In 2006 a laboratory scale of a LMMHD generator for wave energy was designed, manufactured and set up at the Institute of Electrical Engineering, Chinese Academy of Sciences [35, 36]. In 2008 Scientific Applications & Research Associates (SARA) designed, build and tested a 100 $kW$ laboratory demonstration LMMHD generator for wave energy conversion [37]. Recently in 2016 a LMMHD generator coupled with a WECs was proposed to recharge autonomus underwater vehicles, which are limited by their on-board energy storage capability [38, 39]. Since only limited efforts have been made to couple a LMMHD with a wave energy converter, it is necessary to perform more basic and technological research to determine the feasibility of using wave energy to produce electricity through MHD generators.

In this context, the Renewable Energy Institute of the National Autonomous University of Mexico (IER-UNAM) and the Center for Research in Applied Science and Advanced Techology - Querétaro, of the National Polytechnic Institute (CICATA-Querétaro, IPN), as part of the Mexican Center for Innovation in Ocean Energy (CEMIE-O), is developing a research program on LMMHD alternate generators for harnessing wave energy, which is one of the first programs in Mexico of this nature. In the present work, analytical and experimental studies of the LMMHD alternate generator are presented. Given the enormous potential of Mexico for the extraction of wave energy [40], it is worthwhile to understand deeply the different physical phenomena present in a LMMHD alternate generator and assess its potential in the conversion of the energy captured by the WECs into useful energy.

The structure of this thesis is as follows. In chapter 1 a theoretical analysis of the flow and electric features of a LMMHD alternate generator is presented. It starts by establishing the equations that govern the MHD phenomena, which include the fluyd dynamics equa-

tions coupled with the electromagnetic field equations. Then the flow behaviour in the MHD generator is explored in two different regions. First, asymptotic solutions for low and high oscillating frequencies in the uniform magnetic field region far from the magnet edges are used to explore the phase lag produced by the Lorentz force between the velocity and the axial pressure gradient. In addition, the analysis of the boundary layer flow in the non-uniform magnetic field region reveals that small non-linear effects lead to the appearance of steady streaming vortices superimposed on the harmonic flow. Finally, an analysis of the LMMHD alternate generator electrical behavior is performed. In chapter 2 the experimental design of a LMMHD alternate generator at laboratory scale is described. The experimental metodology used is detailed in chapter 3. Chapter 4 presents the experimental results of the flow dynamics and the electrical characterization of the MHD generator. The design of a new experimental device that couples an alternate LMMHD generator with a WEC and that will be tested in a wave channel, is also presented. Ultimately, the conclusions of the thesis are discussed in chapter 5.

# Chapter 1

# Theoretical analysis of a LMMHD alternate generator

In this chapter[§], an overview of the flow dynamics and electrical behavior of a liquid metal magnetohydrodynamic (LMMHD) alternate generator is presented with the purpose of having a better undertanding of the involved physical phenomena. A two-dimensional model of an MHD generator is used to investigate analytically the laminar liquid metal flow created by an oscillatory pressure gradient (for instance, produced by either thermoacoustic effect or ocean waves) imposed at the extremes of the generator duct. We analyze the flow in two different regions. In the first region, we consider the flow far from the edges of the generator where the magnetic field is uniform. With the aim of understanding the interplay of the imposed pressure gradient and the braking Lorentz force created by the interaction of the induced current with the applied magnetic field, asymptotic solutions are derived in the limits of low and high oscillating frequencies. The second analyzed flow region is where the applied magnetic field is non-uniform, that is, the region where the flow enters or leaves the magnetic field. We pay a particular attention to the behavior of the oscillatory boundary layers immersed in the spatially varying magnetic field. These layers, which are a combination of the Stokes and Hartmann layers, determine the flow dynamics to a large extent. Using a perturbation solution, it is found that non-linear effects give rise to a steady streaming vortices in the fringing magnetic field. In addition, a simplified model that allows to characterize the electrical behavior of the LMMHD generator is presented.

## 1.1   Governing equations

MHD studies the motion of electrically conducting (non-magnetizable) fluids in the presence of magnetic fields. The motion of a conducting fluid in an existing magnetic field

---

[§]Part of this chapter is based on the paper: Domnguez-Lozoya, J. C., Perales, H. and Cuevas, S. "Analysis of the oscillatroy liquid metal flow in an alternate MHD generator", Rev. Mex. Fs. (In press).

induces electric currents in the medium. In turn, these currents produce an induced magnetic field which modifies the existing field. Additionally, the interaction of induced and applied magnetic fields with electric currents circulating in the fluid generates a body force, the Lorentz force, that affects the main flow. In general, the main characteristic of MHD phenomena is the coupling of the velocity and electromagnetic fields. Therefore, the fundamental equations that govern MHD flows arise from the coupling of the fluid dynamics and electromagnetic field equations and will be presented next.

### 1.1.1    Fluid Dynamic equations

Since liquids metals can be considered incompressible in most practical applications, the mass conservation equation reduces to

$$\nabla \cdot \mathbf{u} = 0, \tag{1.1}$$

where $\mathbf{u}$ is the velocity field. Far from the melting point liquid metals present a Newtonian behavior [41], therefore the momentum balance leads to the Navier-Stokes equation which is given by

$$\frac{\partial \mathbf{u}}{\partial t} + (\mathbf{u} \cdot \nabla)\mathbf{u} = -\frac{1}{\rho}\nabla p + \nu \nabla^2 \mathbf{u} + \frac{1}{\rho}\mathbf{f}, \tag{1.2}$$

where $p$ is the pressure field while $\mathbf{f}$ is the electromagnetic body force (Lorentz force) per unit volume which will be defined below. In addition, $\rho$ and $\nu$ are the mass density and kinematic viscosity of the fluid, respectively. The energy conservation equation or heat transfer equation when a electromagnetic interaction is present can be expressed as

$$\rho C_p \left[ \frac{\partial T}{\partial t} + (\mathbf{u} \cdot \nabla)T \right] = \nabla \cdot (k_t \nabla T) + \frac{\mathbf{j}^2}{\sigma} + \Phi_\nu, \tag{1.3}$$

where T is the temperature, $\mathbf{j}$ is the electric current density vector, $\Phi_\nu$ denotes the viscous disipation that involves quadratic terms of the velocity gradients, $C$ is the specific heat, $k$ is the thermal conductivity and $\sigma$ is the electric conductivity. The second term on the rigth-hand side denote the Joule dissipation in the fluid due to the circulation of currents in the medium. Notice that the energy conservation equation is not coupled with the momentum and mass conservation equations. Evidently, the above equations are insufficient to describe the phenomenon completely if the electromagnetic interaction is considered. Therefore, they must be complemented with the equations of the electromagnetic field, which in addition to the Maxwell equations and the equation for the Lorentz force, comprise the constitutive equations that characterize the fields in different media.

### 1.1.2    Electromagnetic field equations

The laws of electromagnetism are summarized in a series of expressions known as Maxwell's equations, which are a set of four equations that include the Gauss's law for the electric

field, the Gauss's law for the magnetic field, the Faraday's law of induction and Ampere-Maxwell law, which synthesize the behavior of electromagnetic phenomena.The Maxwell macroscopic equations in a homogeneous, isotropic and linear medium are briefly described below.

Gauss's law for the electric field indicates that the electric field flux through a closed surface is equal to the total charge enclosed in the volume limited by this surface. In differential form the Gauss's law is expressed as

$$\nabla \cdot \mathbf{E} = \frac{\rho_e}{\epsilon}, \tag{1.4}$$

wherer $\mathbf{E}$ is the electric field, $\rho_e$ is the electric charge density, and $\epsilon$ is the electric permittivity of the medium. The Gauss's law for magnetism expresses the nonexistence of isolated magnetic charges, or as they are usually known, magnetic monopoles. Distributions of magnetic sources are always neutral in the sense that they have a north and south poles, so their flux through any closed surface is zero, so that in differential form we have

$$\nabla \cdot \mathbf{B} = 0, \tag{1.5}$$

where $\mathbf{B}$ is the magnetic induction field. Faraday's law of induction establishes that the electromotive force induced in a circuit is directly proportional to the rate of change of the magnetic flux that crosses the circuit. In other words, it establishes the possibility of producing electric fields from time varying magnetic fields. At every point in space Faraday's law can be expressed in the form

$$\nabla \times \mathbf{E} = -\frac{\partial \mathbf{B}}{\partial t}. \tag{1.6}$$

The Ampère-Maxwell law or generalized Ampère's law, establishes that the magnetic fields can be produced by electrical currents or due to the time variation of electric fields. The differential expression takes the form

$$\nabla \times \mathbf{B} = \mu_m \mathbf{j} + \mu_m \epsilon \frac{\partial \mathbf{E}}{\partial t}, \tag{1.7}$$

where $\mu_m$ is the magnetic permeability of the medium. Since liquid metals are non magnetic materials, their magnetic permeability is approximately equal to the magnetic permeability of the vacuum $\mu_0$. When applying the divergence operator to equation (1.7) and using the Gauss law (1.4), we obtain the equation of conservation of the electric charge or continuity equation, which establishes that there is no destruction or creation of electric charge, and that in any electromagnetic process the total charge of an isolated system is conserved. In its differential form, the charge conservation equation has the following form

$$\nabla \cdot \mathbf{j} + \frac{\partial \rho_e}{\partial t} = 0. \tag{1.8}$$

Maxwell's equations must be complemented by including a constitutive equation that relates the electric current density in the medium with the fields **E** and **B**. The most common equation, valid for conductive liquids and gases, is the so-called Ohm's law. In a resting conductor it is found that the electric current density **j** is proportional to the force experienced by the free charges [41]

$$\mathbf{j} = \sigma \mathbf{E_r}, \tag{1.9}$$

where **E_r** is the electric field from a reference frame at rest. If the electrically conductive material moves with respect to the laboratory system with speed **u**, Ohm's law takes the form

$$\mathbf{j} = \sigma(\mathbf{E} + \mathbf{u} \times \mathbf{B}) + \rho_e \mathbf{u}, \tag{1.10}$$

where the second term of the right side is known as the convective current. Finally, we must consider the electromagnetic force exerted on the medium. In a continuous medium with charge density $\rho_e$ and electric current density **j**, the electromagnetic force (Lorentz force) has the form

$$\mathbf{f} = \rho_e \mathbf{E} + \mathbf{j} \times \mathbf{B}. \tag{1.11}$$

### 1.1.3   MHD approximation

The coupling of the fluid dynamics equations and the electromagneticfield equations require some considerations. The fluid dynamics equations are not relativistic which means that are invariant before Galilean transformations. In turn, electromagnetic field equations are relativistic which implies that are invariant before Lorentz transformations. Mixing equations with different invariance properties could lead to an erroneous description of the phenomenon. To solve this incompatibility we use what is known as the MHD approximation , which is based on the simplification of the electromagnetic equations using the following assumptions:

- All considered phenomena are not relativisitc This means that the speed of the electrically conducting fluid and any material object is much lower than the speed of light (c), i.e. $c^2 \gg u^2$. This assumption allows us to neglect the convective current ($\rho_e \mathbf{u}$) in the Ohm's law and the electric term in the Lorentz force ($\rho_e \mathbf{E}$).

- The flows take place in quasi-stationary or low frequency electromagnetic fields, thus implying that the displacement current ($\mu_0 \epsilon \frac{\partial \mathbf{E}}{\partial t}$) of the Ampère-Maxwell law is negligible.

- The induced electric fields are of order **u**×**B**, which is equivalent to assuming that the induced magnetic field is much smaller than the applied magnetic field. This implies that the magnetic field is the same in any frame of reference.

Under this approximation the electromagnetic field equations are simplified so that they recover the Galilean invariance, making it possible to merge them with the equations of the fluid dynamics and giving rise to the equations that govern the MHD phenomena. The resulting set of equations under the MHD aproximation has the following form

$$\nabla \cdot \mathbf{u} = 0, \tag{1.12}$$

$$\frac{\partial \mathbf{u}}{\partial t} + (\mathbf{u} \cdot \nabla)\mathbf{u} = -\frac{1}{\rho}\nabla p + \nu\nabla^2\mathbf{u} + \frac{1}{\rho}\mathbf{j} \times \mathbf{B}, \tag{1.13}$$

$$\nabla \times \mathbf{E} = -\frac{\partial \mathbf{B}}{\partial t}, \tag{1.14}$$

$$\nabla \cdot \mathbf{B} = 0, \tag{1.15}$$

$$\nabla \times \mathbf{B} = \mu_0 \mathbf{j}, \tag{1.16}$$

$$\mathbf{j} = \sigma(\mathbf{E} + \mathbf{u} \times \mathbf{B}). \tag{1.17}$$

Note that the energy conservation equation is not included owing to the fact that the determination of the thermal behavior of the system is not the goal of this work. The Gauss equation for the electric field has been ignored since the charge density is not of interest and the electric field is completely defined by Faraday's law (1.14), Ampère's law (1.16) and Ohm's law (1.17). The Lorentz's force equation is implicit in the Navier-Stokes equations as the relevant body force. From equations (1.14)-(1.17) it is possible to obtain a transport equation for the magnetic field, known as the induction equation, which describe the magnetic field transport by diffusion and convection. This equation is expressed as

$$\frac{\partial \mathbf{B}}{\partial t} = \nu_m\nabla^2\mathbf{B} + \nabla \times (\mathbf{u} \times \mathbf{B}), \tag{1.18}$$

where $\nu_m = 1/\mu_0\sigma$ is known as the magnetic diffusivity. The diffusive transport is represented by $\nu_m\nabla^2\mathbf{B}$, while the convective transport is given by $\nabla \times (\mathbf{u} \times \mathbf{B})$. The dominant transport mechanism (convective or diffusive) in a given problem is determined to a great extent by the value of the electrical conductivity of the fluid. In more general terms, the dominance of diffusive or convective mechanisms is determined by the magnetic Reynolds number defined as $R_m = UL/\nu_m = \mu_0\sigma UL$ where $U$ and $L$ are characteristic scales of velocity and length. When $Rm << 1$, the transport of magnetic field is dominated by diffusion while for $Rm >> 1$ convective transport is the dominant one. Most MHD phenomena at the laboratory and industrial scales take place under conditions where $R_m << 1$.

## 1.2 Oscillatory flow in an MHD generator

We now consider the oscillatory flow of a liquid metal in a duct of rectangular cross-section under a transverse magnetic field. The walls perpendicular to the applied field are electrical

insulators while those parallel to the field are perfect conductors connected to an external load (see Fig.1.1). The oscillatory flow is driven by a zero mean, time-periodic pressure gradient imposed at the extremes of the duct. The system of equations that govern the un-
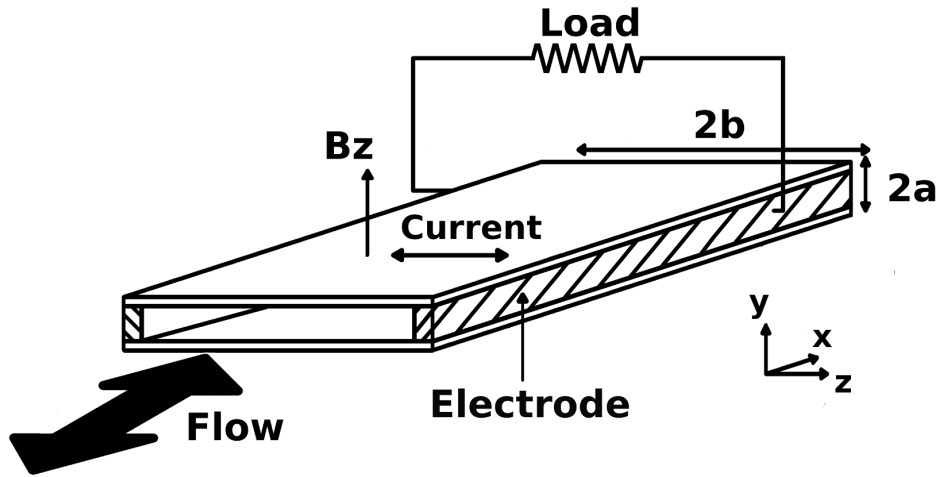


Fig. 1.1: Sketch of the alternate MHD generator.

steady flow of an incompressible, electrically conducting viscous fluid in the presence of a magnetic field are the continuity equation, Navier-Stokes equation, Faraday's law of induction, Ampère's law, Gauss's law for the magnetic field and Ohm's law which, respectively, can be conveniently written in the following dimensionless form

$$\nabla \cdot \mathbf{u} = 0, \tag{1.19}$$

$$\frac{\partial \mathbf{u}}{\partial t} + \frac{R}{R_\omega^2}(\mathbf{u} \cdot \nabla)\mathbf{u} = -\nabla p + \frac{1}{R_\omega}\nabla^2 \mathbf{u} + \frac{Ha^2}{R_\omega}\mathbf{j} \times \mathbf{B}, \tag{1.20}$$

$$\nabla \times \mathbf{E} = -\frac{R_\omega^2}{R}\frac{\partial \mathbf{B}}{\partial t}, \qquad \nabla \times \mathbf{B} = R_m \mathbf{j}, \tag{1.21}$$

$$\nabla \cdot \mathbf{B} = 0, \qquad \mathbf{j} = \mathbf{E} + \mathbf{u} \times \mathbf{B}, \tag{1.22}$$

where the flow velocity $\mathbf{u}$, the pressure $p$, the magnetic field $\mathbf{B}$, the electric field $\mathbf{E}$ and the current density $\mathbf{j}$ are normalized by $U_o = G/\rho\omega$, $Gh$, $B_o$, $U_oB_o$ and $\sigma U_o B_o$, respectively. Here, $G$ and $\omega$ are the amplitude and frequency of the imposed oscillatory pressure gradient, $\rho$ and $\sigma$ are the mass density and the electrical conductivity of the fluid, $h$ is the distance between the walls transverse to the magnetic field, and $B_o$ is the maximum strength of the applied field, respectively. The coordinates $(x, y, z)$ and time $t$, are normalized by $h$ and $1/\omega$, respectively. Further, the dimensionless parameters $R_\omega = \omega h^2/\nu$, $R = Gh^3/\rho\nu$ and $Ha = B_o h \sqrt{\sigma\rho\nu}$, are the frequency parameter (or oscillation Reynolds number), the amplitude parameter and the Hartmann number, respectively, where $\nu$ is the kinematic viscosity. Assuming that the physical and geometrical properties of the system remain unchanged, these dimensionless parameters express, correspondingly, the influence of the oscillation frequency, the amplitude of the pressure gradient and the magnetic field strength. In turn, $R_m = \mu_0 \sigma U_o h$ is the magnetic Reynolds number that in this context gives an estimation of the induced magnetic field compared with the applied field [42].

The oscillatory motion of the fluid inside the magnetic field induces an electric current density in the spanwise ($z$) direction. The current, in turn, interacts with the applied field originating a braking Lorentz force in the axial $x$-direction. Usually, in liquid metal MHD flows the low magnetic Reynolds number approximation holds which means that the magnetic field induced by the fluid motion is much smaller than the applied field and can be neglected [42]. Hence, the magnetic field is uncoupled from the fluid motion and governed by the magnetostatic equations.

## 1.3   Flow in the uniform magnetic field region

We now assume that the aspect ratio of the generator is very large, that is, $w/h \gg 1$ (see Fig. 1.1) so that the conducting walls (electrodes) are located at distant positions $z = \pm z_o$, connected to an external electrical circuit. Under this approximation, we can consider that the oscillatory flow is two-dimensional, confined between the insulating walls transverse to the magnetic field (see Fig. 1.2). Since the current is induced in the direction perpendicular to the plane of motion, there must exist an electric field, $E_z$, the value of which depends on the external electrical load. As the magnetic field remains unperturbed, Faraday's law of induction reduces to $\nabla \times \mathbf{E} = 0$ and the electric field becomes potential. In fact, it can be shown that under the present assumptions $E_z$ is spatially constant and it is at most a function of time [43].
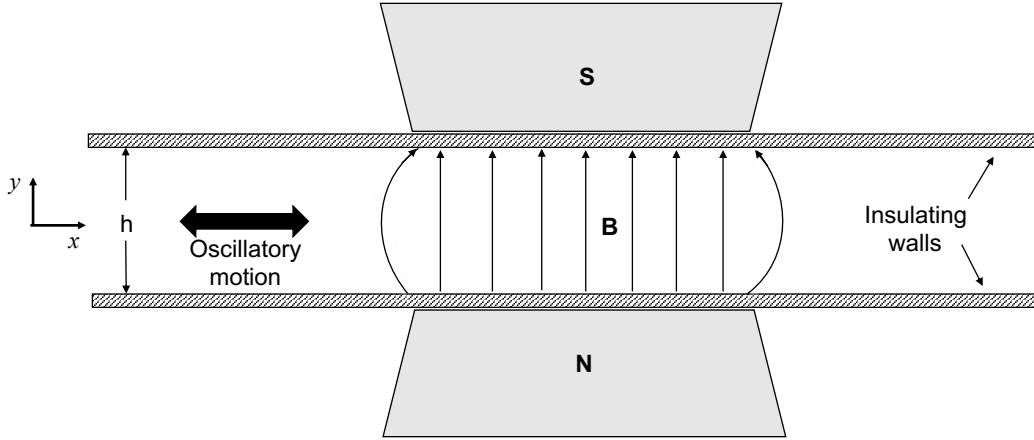
Fig. 1.2: Two-dimensional model of the flow in an MHD alternate generator.

We now restrict to the region where the applied field is uniform so that, in dimensionless terms, $\mathbf{B} = \hat{\mathbf{y}}$. In this region the flow is fully developed, therefore, $\mathbf{u} = u(y,t)\,\hat{\mathbf{x}}$ and the Navier-Stokes equation reduces to

$$\frac{\partial u}{\partial t} = -\frac{\partial p}{\partial x} + \frac{1}{R_\omega}\frac{\partial^2 u}{\partial y^2} - \frac{Ha^2}{R_\omega}(E_z + u). \tag{1.23}$$

We disregard transient solutions and consider that the harmonic axial pressure gradient that drives the flow is given by the real part of $-\partial p/\partial x = e^{it}$. Assuming that the axial velocity component and the electric field are also harmonic functions of time, $u = u_0(y)e^{it}$ and $E_z = -Ke^{it}$, with $K$ a constant known as the load factor [44], a solution to the Eq. (1.23) that satisfies the no-slip boundary conditions can be found, namely,

$$u(y,t) = U_m e^{it} \lambda \left( \frac{\cosh\lambda - \cosh\lambda y}{\lambda\cosh\lambda - \sinh\lambda} \right), \tag{1.24}$$

where $\lambda = \sqrt{Ha^2 + iR_\omega}$ and $U_m$ is the dimensionless spatial average of the velocity profile in the cross-section. From this solution it is possible to establish a model of the alternate MHD generator that allows to assess the electrical performance of the device [44], as it will be shown in section 1.5.

In the present section the attention is focused in the interplay of inertia and the braking Lorentz force. The explicit form of the velocity profile (1.24) is, however, not particularly insightful. In order to get a better understanding of the physical behavior of this oscillatory MHD flow, we look for asymptotic solutions in the limits $R_\omega \ll 1$ and $R_\omega \gg 1$, which correspond to the low and high frequency oscillatory motions, respectively.

### 1.3.1 Low-frequency solution: $R_\omega \ll 1$

In the low frequency limit it is possible to obtain a regular asymptotic solution in the flow domain [45]. Since we are interested in the limit when $R_\omega$ takes very small values, it is convenient to use the rescaled variables $\hat{u} = u/R_\omega$ and $\hat{E}_z = E_z/R_\omega$, so that Eq. (1.23) becomes

$$R_\omega \frac{\partial \hat{u}}{\partial t} = -\frac{\partial p}{\partial x} + \frac{\partial^2 \hat{u}}{\partial y^2} - Ha^2(\hat{E}_z + \hat{u}). \tag{1.25}$$

Substituting the harmonic pressure gradient and assuming solutions given as the real part of the expressions $\hat{u} = \hat{g}(y)e^{it}$ and $\hat{E}_z = -\hat{K}e^{it}$, an equation for the function $\hat{g}(y)$ is found. We expand this function as a perturbation series on the small parameter $R_\omega$, namely,

$$\hat{g}(y) = \hat{g}_o(y) + R_\omega \hat{g}_1(y) + O(R_\omega^2), \tag{1.26}$$

and solve the corresponding equations with no-slip boundary conditions at each order on the parameter $R_\omega$. After taking the real part, the final result is

$$
\begin{aligned}
\hat{u}(y,t) = {} & \hat{u}_{op} \left\{ \left[ 1 - \frac{\cosh Ha\, y}{\cosh Ha} \right] \cos t + R_\omega \left[ \frac{1}{2Ha} \left( y \frac{\sinh Ha\, y}{\cosh Ha} \right.\right.\right. \\
& \left.\left.\left. - \tanh Ha \frac{\cosh Ha\, y}{\cosh Ha} \right) + \frac{1}{Ha^2} \left( 1 - \frac{\cosh Ha\, y}{\cosh Ha} \right) \right] \sin t \right\} \\
& + O(R_\omega^2),
\end{aligned}
\tag{1.27}
$$

where $\hat{u}_{op} = Ha^{-2} + \hat{K}$. At zero-order in $R_\omega$, a quasi-steady Hartmann flow in phase with the pressure gradient oscillation, is obtained. As usual, the profile is flattened as $Ha$ increases [42]. An out of phase contribution is also found at $O(R_\omega)$, but it is modulated by terms of $O(Ha^{-1})$ and $O(Ha^{-2})$ which become negligible the higher the $Ha$ values are. When the Hartmann number is very small, $i.e.\ Ha \to 0$, a purely hydrodynamic flow is recovered

$$\hat{u}(y,t) = \left[ \frac{(1-y^2)}{2} \cos t + \frac{R_\omega}{24}(1-y^2)(5-y^2) \sin t \right], \tag{1.28}$$

which shows an in-phase Poiseuille flow contribution. The phase angle between the pressure gradient and the velocity is given by

$$\theta = \arctan \left[ \frac{-R_\omega \left[ \frac{1}{2Ha} \left( y \frac{\sinh Hay}{\cosh Ha} - \tanh Ha \frac{\cosh Hay}{\cosh Ha} \right) + \frac{1}{Ha^2} \left( 1 - \frac{\cosh Hay}{\cosh Ha} \right) \right]}{\left[ 1 - \frac{\cosh Hay}{\cosh Ha} \right]} \right]. \tag{1.29}$$

Note that when $Ha \to 0$ viscosity originates a non-zero phase angle, namely, $\theta = -\arctan[R_\omega(5-y^2)/12]$. In turn, when $Ha \to \infty$, the phase angle reduces to zero indicating that the flow is frozen by the strong magnetic field interaction.

## 1.3.2   High-frequency solution: $R_\omega \gg 1$

At high frequencies a uniform asymptotic solution for the whole domain does not exist. Therefore, matching asymptotic solutions in the core and the boundary layer has to be sought. For the core, we start from Eq. (1.23) and introduce the variables $u = g(y)e^{it}$ and $E_z = -Ke^{it}$, assuming that $-\partial p/\partial x = e^{it}$. Hence, we get the equation

$$ig - 1 = \frac{1}{R_\omega}\left[\frac{d^2g}{dy^2} - Ha^2(g - K)\right]. \tag{1.30}$$

We now look for a solution $g(y)$ as an expansion in the small parameter $R_\omega^{-1}$, namely,

$$g(y) = g_o(y) + \frac{1}{R_\omega}g_1(y) + O(R_\omega^{-2}). \tag{1.31}$$

Here, we assume that $Ha^2 = \gamma R_\omega$, where $\gamma$ is a positive real number. Then in the limit $R_\omega \to \infty$, from Eq. (1.30) and (1.31), the first order solution in the core is $g_o = (1 + \gamma K)/(\gamma + i) = (1 + \gamma K)(\gamma - i)/(\gamma^2 + 1)$. Therefore, the core velocity field is

$$u_c = \frac{(1 + \gamma K)}{(\gamma^2 + 1)}(\gamma \cos t + \sin t) + O(R_\omega^{-2}). \tag{1.32}$$

This represents a uniform time-periodic flow that lags behind the imposed pressure gradient according to the value of $\gamma$, where the phase angle between the pressure gradient and the core velocity is $\theta_c = -\arctan[1/\gamma]$. For $\gamma \ll 1$, a purely hydrodynamic flow is obtained. In this case, the Lorentz force is negligible and there is a lag of $-\pi/2$ in the motion of the core with respect to the pressure gradient. In turn, if $\gamma = 1$, the Lorentz force is of the same order of magnitude as the inertial acceleration and the core flow presents a phase difference of $-\pi/4$ with respect to the pressure gradient. When $\gamma \gg 1$, the Lorentz force is dominant, therefore, the phase lag is negligible and the core follows the pressure gradient oscillation.

Let us now consider the boundary layer flow. We introduce the stretched variable $Y = R_\omega^{1/2}(1 + y)$ in the bottom boundary layer, hence at the wall, $Y = 0$ and $u(0, t) = 0$. Then Eq. (1.30) becomes

$$\frac{d^2g_b}{dY^2} - ig_b + 1 = \gamma(g_b - K). \tag{1.33}$$

for the corresponding function $g_b$ in the boundary layer. Expressing $g_b$ as a series like (1.31), the solution of Eq. (1.33) that satisfies no-slip boundary conditions and that matches with the core flow ($g_b|_{Y\gg1} = (1 + \gamma K)/(\gamma^2 + 1)$) within an error of order $O(R_\omega^{-1})$, leads to the boundary layer flow

$$\begin{aligned}
u(Y, t) &= \frac{(1 + \gamma K)}{(\gamma^2 + 1)}\{[\gamma - \exp(-\alpha Y)(\gamma \cos\beta Y - \sin\beta Y)]\cos t \\
&\quad + [1 - \exp(-\alpha Y)(\cos\beta Y + \gamma \sin\beta Y)]\sin t\} + O(R_\omega^{-2}),
\end{aligned} \tag{1.34}$$

where

$$\left.\begin{array}{c} \alpha \\ \beta \end{array}\right\} = \left[\frac{\sqrt{\gamma^2 + 1} \pm \gamma}{2}\right]^{\frac{1}{2}}, \tag{1.35}$$

The phase angle between the boundary layer and the pressure gradient is given by

$$\theta_b = \arctan\left\{\frac{-[1 - \exp(-\alpha Y)(\cos\beta Y + \gamma\sin\beta Y)]}{\gamma - \exp(-\alpha Y)(\gamma\cos\beta Y - \sin\beta Y)}\right\}. \tag{1.36}$$

Again, in-phase and out-of-phase contributions are obtained in the boundary layer, the structure of which depends on the value of $\gamma$. Provided $\gamma \ll 1$, a purely hydrodynamic (Stokes) boundary layer is found [45]. When $\gamma = 1$, a mixture of Stokes and Hartmann layers results. Finally, in the case $\gamma \gg 1$, magnetic forces dominate and a Hartmann layer oscillating in phase with the pressure gradient ($\hat{u} \approx (1/R_\omega)[1 - e^{-\sqrt{\gamma}Y}]\cos t$) is obtained.

An illustrative way of visualizing the phase lag produced by the Lorentz force between the velocity and the pressure gradient is by noticing that these quantities satisfy the parametric equations of an ellipse in the plane $u$ vs. $-\partial p/\partial x$ [46]. If we define $X = -\partial p/\partial x$ and $Y = u$, we get for either the core or the boundary layer flows

$$\left(\frac{a^2}{b^2} + 1\right)X^2 - \frac{2a}{fb^2}XY + \frac{Y^2}{f^2b^2} = 1, \tag{1.37}$$

where $f(\gamma) = (1 + \gamma K)/(\gamma^2 + 1)$. For the core flow, $a = \gamma$ and $b = 1$, while for the boundary layer flow, we have $a = \gamma - \exp(-\alpha Y)(\alpha\cos\beta Y - \sin\beta Y)$ and $b = 1 - \exp(-\alpha Y)(\cos\beta Y + \gamma\sin\beta Y$. In Figures 1.3 and 1.4, equation (1.37) is plotted during a whole cycle for the case $R_\omega = 30$, $K = 0.8$, and different $\gamma$ values. Some interesting information can be extracted from these plots, particularly because they clearly compare the velocity amplitude before and after the pressure gradient inversion. In fact, the vertical coordinate axis indicates the precise moment at which the pressure gradient is inverted. In the second and fourth quadrants, the pressure gradient acts in favor of the fluid motion, while in the first and third quadrants it acts against the fluid motion. Figure 1.3 shows the curves corresponding to the core flow. As it was shown, in the laminar hydrodynamic regime ($\gamma = 0$, *i.e.* $Ha = 0$) the core flow presents a phase difference of $-\pi/2$ with respect to the pressure gradient when $R_\omega \gg 1$, and the corresponding curve is a circle. For increasing values of $\gamma$, the curve is distorted and rotated clockwise as a result of stronger magnetic interaction which changes the phase difference between the velocity and the pressure gradient. When the Lorentz force is of the same order of magnitude as the inertial acceleration ($\gamma = 1$), a tilted ellipse is obtained while in the case $\gamma \gg 1$ ($Ha \to \infty$), no phase difference exists between the flow and the pressure gradient, therefore, the curve reduces to a straight line. The corresponding curves for the boundary layer flow are shown in Figure 1.4. Although similar ellipses are formed note that they are not the same as in the core flow since, in addition to the magnetic interaction, viscosity also affects the phase difference between the velocity and the pressure

gradient. In fact, no circle is formed even when $Ha = 0$. However, when $\gamma \gg 1$ $(Ha \to \infty)$ a straight line is formed indicating that the phase difference disappears.
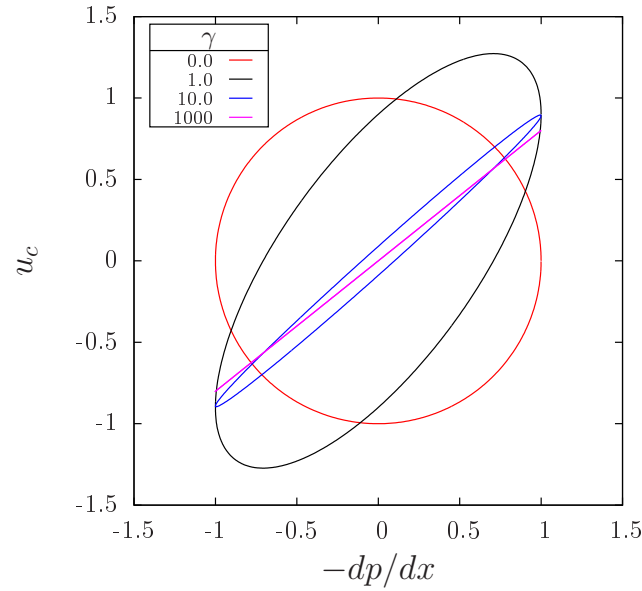


Fig. 1.3: The phase-like plane for the core velocity solution for different $\gamma$ values and $K = 0.8$.
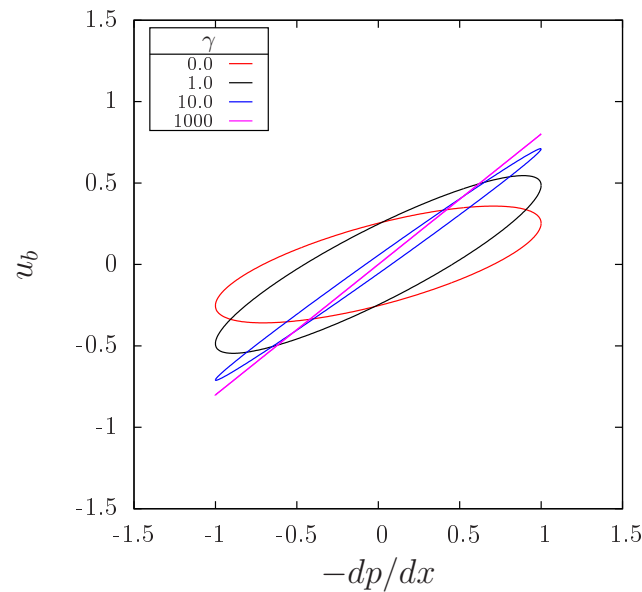


Fig. 1.4: The phase-like plane for the boundary layer velocity solution for different $\gamma$ values, $Y = 0.5$ and $K = 0.8$.

### 1.3.3 Summary

We have explored the zero-mean oscillatory two-dimensional flow of a liquid metal in an alternate MHD generator driven by an imposed harmonic pressure gradient. In the uniform field region, characteristic flows were explored through asymptotic solutions for a small ($R_\omega \ll 1$) and high ($R_\omega \gg 1$) oscillation frequencies and arbitrary Hartmann numbers. For small frequencies, a first order quasi-steady Hartmann flow in phase with the pressure gradient is obtained, while an out of phase contribution is found at $O(R_\omega)$. For high frequencies a solution for the core and boundary layer was obtained. The core solution represent a uniform time periodic flow that lags from the imposed pressure gradient according to the strength of the magnetic field. When the magnetic field is negligible, a purely hydrodynamic flow is obtained and the lag between the core and the pressure gradient is $\pi/2$. For very strong magnetic field, the lag is negligible and the core follows the pressure gradient oscillation. Out of phase and in phase contributions were also found in the boundary layer, where a purely hydrodynamic (Stokes) boundary layer is obtained for negligible field while a Hartmann layer, oscillating in phase with the pressure gradient, is obtained for strong fields. These results can be conveniently synthesized graphically.

## 1.4    Flow in the non-uniform magnetic field region

In this section, we address the oscillatory flow of the liquid metal close to the edges of the magnets where the magnetic field is non-uniform. In this region, the transverse magnetic field varies from its maximum strength to zero as the $x$ distance to the edge of the magnet increases. Although the cross-section of the duct does not change, this can be considered as an entrance flow problem due the non-homogeneity of the magnetic field. Forced oscillations produced by the imposed pressure gradient in the outer flow produce an oscillatory flow in the Stokes-Hartmann boundary layer, however, due to the action of viscosity, the flow oscillations in this layer do not average to zero but a net steady flow is produced, known as steady streaming [47, 48]. The steady streaming is induced by the non-linear Reynolds stresses in the boundary layer that appear due to the axial dependence of the streamwise velocity, produced in this case by the existence of the non-uniform field. In hydrodynamic flows, steady streaming appears, for instance, at the entrance of a rigid tube when a zero-mean oscillatory flow is imposed [49] or in the classic problem of oscillating bluff bodies [48, 50]. The most relevant characteristic feature of this kind of oscillatory flows is the persistence of the steady streaming motion beyond the boundary layer [51]. The action of a uniform transverse magnetic field on the steady streaming produced by an oscillatory laminar boundary layer close to an insulating curved wall was previously studied using a perturbation expansion taking the inverse of the Strouhal number as a small parameter [52]. Following a similar procedure, we explore here the appearance of steady streaming in the boundary layers of the MHD generator promoted by the non-uniformity of the applied transverse magnetic field.

As in section 1.3, we consider the oscillatory motion of the liquid metal limited by two infinite insulating plane walls at rest under a transverse magnetic field. We are now focused on the region close to the edges of the magnets, so the transverse magnetic field is expressed in the form $\mathbf{B} = B_y(x)\hat{\mathbf{y}}$ , where the variation of the field in the axial direction is given in dimensionless form as [53, 54]

$$B_y(x) = \frac{1}{1 + e^{-x/x_0}}. \tag{1.38}$$

Here $x_0$ is a positive constant whose magnitude governs the magnetic field gradient. Figure 1.5 shows the magnetic field distribution for different vales of $x_0$. We can observe that $B_y \to 0$ as $x \to -\infty$ and $B_y \to 1$ as $x \to \infty$. Although this field is not curl-free, it is a reasonable approximation that take into account the streamwise variation of the magnetic field [53, 54].

We assume that far from the walls (outer flow) the fluid presents an irrotational zero-mean oscillatory motion in the axial direction produced by the imposed pressure gradient which in dimensionless form can be expressed as the real part of $U(x,t) = U_0(x)e^{it}$. Due to continuity, the component of the velocity in the direction normal to the wall is $-(y+c)(dU/dx)e^{it}$ where $c$ is a complex constant. In dimensionless form, the outer flow is
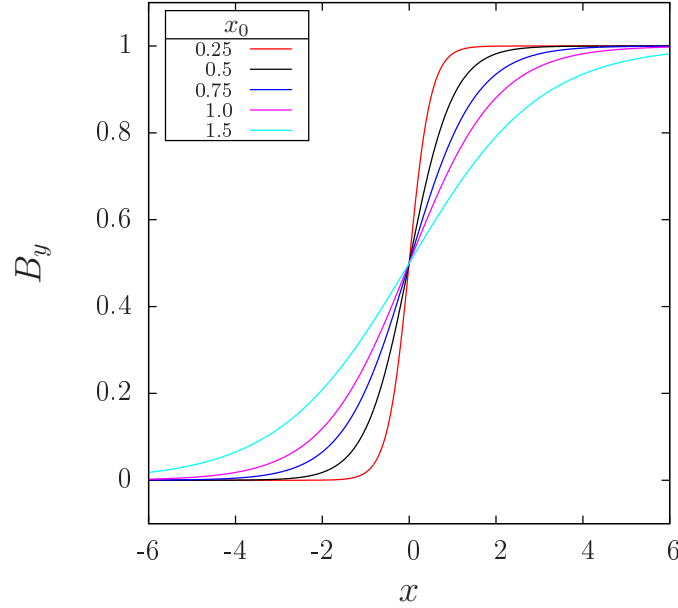
Fig. 1.5: Dimensionless applied magnetic field distribution as a function of the axial coordinate $x$ in the magnet edge region for different values of the $x_0$ parameter.

governed by the equations

$$\frac{\partial U}{\partial t} + \epsilon_s U \frac{\partial U}{\partial x} = -N_\omega \frac{\partial p}{\partial x} - N_\omega J_z B_y, \tag{1.39}$$

$$J_z = E_z + U B_y, \quad \frac{\partial J_z}{\partial z} = 0, \tag{1.40}$$

where the outer velocity $U$, the pressure $p$, the outer current density $J_z$ and the electric field $E_z$ are normalized by $U_\infty$, $\sigma U_\infty B_0^2 h$, $\sigma U_\infty B_0$ and $U_\infty B_0 h$, respectively. Here $U_\infty$ is the amplitude of the outer flow velocity. Likewise, the coordinates $(x, y, z)$ and time $t$ are normalized by $h$ and $1/\omega$, respectively. In addition the dimensionless parameters,

$$\epsilon_s = \frac{U_\infty}{\omega h}, \quad N_\omega = \frac{Ha^2}{R_\omega} = \frac{\sigma B_0^2}{\rho \omega}, \tag{1.41}$$

are respectively, the inverse of the Strouhal number and the oscillation interaction parameter [52]. $\epsilon_s$ and $N_\omega$ may be interpreted as the ratio of the amplitude of the oscillation to the characteristic length $h$ and the ratio of the magnetic to the inertial forces, respectively. Equation (1.39) corresponds to the Euler equation while equations (1.40) express the Ohm's law and conservation of current in the outer flow. We assume that the small amplitude of oscillation approximation applies, that is $\epsilon_s \ll 1$, which ensures that boundary-layer separation will not arise.

From equations (1.39) and (1.40), the explicit form of the function $U_0(x)$ can be determined at the lowest order in $\epsilon_s$, namely,

$$U_0(x) = \frac{N_\omega(1 + B_y K)}{i + N_\omega B_y^2} \tag{1.42}$$

where the harmonic variation of the electric field was assumed.

The governing equations for the inner layer flow are

$$\frac{\partial u}{\partial x} + \frac{\partial v}{\partial y} = 0 \tag{1.43}$$

$$\frac{\partial u}{\partial t} + \epsilon_s \left( u \frac{\partial u}{\partial x} + v \frac{\partial u}{\partial y} \right) = -N_\omega \frac{\partial p}{\partial x} + \frac{1}{R_\omega} \frac{\partial^2 u}{\partial y} - N_\omega j_z B_y \tag{1.44}$$

$$j_z = E_z + u B_y, \quad \frac{\partial j_z}{\partial z} = 0, \tag{1.45}$$

where the velocity components in $x-$ and $y-$directions, $u$ and $v$, respectively, are normalized with $U_\infty$ while the inner current density, $j_z$, is normalized with $\sigma U_\infty B_0$. In order to ensure the validity of the boundary-layer approximation for the inner flow, it is assumed that $R_\omega \gg 1$. The boundary conditions to be satisfied by the inner flow are

$$u(x, 0, t) = 0, \tag{1.46}$$

$$v(x, 0, t) = 0, \tag{1.47}$$

$$u(x, y, t) \longrightarrow U(x, t); \quad \text{as} \quad y \longrightarrow \infty, \tag{1.48}$$

where (1.46) and (1.47) represent the no-slip condition of the velocity components at the wall and condition (1.48) matches the inner flow to the outer flow.

## 1.4.1   First order solution

We now look for a solution of the boundary layer problem as a perturbation expansion in the small parameter $\epsilon_s$. From the incompressible condition, the velocity components are

$$u = \frac{\partial \psi}{\partial y}, \quad v = -\frac{\partial \psi}{\partial x}, \tag{1.49}$$

where $\psi$ is the stream function that can be expressed in the form

$$\psi(x, y, t) = \psi_0(x, y, t) + \epsilon_s \psi_1(x, y, t) + O(\epsilon_s^2). \tag{1.50}$$

where subindexes 0 and 1 denote the first and second approximations, respectively. By eliminating the pressure gradient and current densities in Eq. (1.44) with the substitution

of equations (1.39), (1.40), (1.45), and using (1.49) and (1.50), we find that $\psi_0$ satisfies the equation

$$\frac{\partial^2 \psi_0}{\partial t \partial y} - \frac{1}{R_\omega} \frac{\partial^3 \psi_0}{\partial y^3} + N_\omega B_y^2 \frac{\partial \psi_0}{\partial y} = \frac{\partial U}{\partial t} + N_\omega B_y^2 U, \tag{1.51}$$

with boundary conditions

$$\frac{\partial \psi_0}{\partial y}(x, 0, t) = 0, \tag{1.52}$$

$$\frac{\partial \psi_0}{\partial x}(x, 0, t) = 0, \tag{1.53}$$

$$\frac{\partial \psi_0}{\partial y}(x, y, t) \longrightarrow U(x, t); \quad \text{as} \quad y \longrightarrow \infty. \tag{1.54}$$

Assuming that

$$\psi_0(x, y, t) = U_0(x) \xi_0(x, y) e^{it}, \tag{1.55}$$

the function $\xi_0$ satisfies

$$\frac{\partial^3 \xi_0}{\partial y^3} - \frac{\partial \xi_0}{\partial y} \left[ iR_\omega + Ha^2 B_y^2 \right] = -(Ha^2 B_y^2 + iR_\omega), \tag{1.56}$$

with boundary conditions

$$\xi_0(x, 0) = \frac{\partial \xi_0(x, 0)}{\partial y} = 0, \quad \frac{\partial \xi_0(x, y)}{\partial y} \longrightarrow 1 \quad \text{as} \quad y \longrightarrow \infty. \tag{1.57}$$

The solution of (1.56) that satisfies conditions (1.57) is

$$\xi_0(x, y) = y - \frac{1}{\alpha + i\beta}(1 - e^{-(\alpha + i\beta)y}), \tag{1.58}$$

where

$$\alpha(x) = \left[ \frac{\sqrt{Ha^4 B_y^4 + R_\omega^2} + Ha^2 B_y^2}{2} \right]^{\frac{1}{2}}, \quad \beta(x) = \left[ \frac{\sqrt{Ha^4 B_y^4 + R_\omega^2} - Ha^2 B_y^2}{2} \right]^{\frac{1}{2}}.$$

From the solution (1.58) it is possible to estimate the thickness of the Stokes-Hartmann boundary layer, namely, $\delta \approx 1/[\alpha(x)^2 + \beta(x)^2]^{1/2}$. Notice that due to the streamwise variation of the magnetic field, the layer thickness is not uniform in this region. The layer is much thinner where the magnetic field is strong ($B_y \approx 1$). If $Ha^2 \gg R_\omega$, the layer thickness is of the order of the Hartmann layer, namely, $\delta \approx Ha^{-1}$ [42]. Far enough from the magnet edges, say $x < 10x_0$, the magnetic field vanishes so that $Ha = 0$, and the velocity components reduce to

$$u_0 = U_0(x) e^{it}(1 - e^{-(1+i)\eta}),$$

$$v_0 = -\frac{dU_0}{dx}e^{it}\left(\eta - \frac{1}{2}(1-i)\left[1 - e^{-(1+i)\eta}\right]\right),$$

which coincide with the ordinary hydrodynamic limit [47], where $\eta = y\sqrt{R_\omega/2}$. In that region, the layer thickness reduces to that of the Stokes layer, that is $\delta \approx 1/R_\omega^{1/2}$.

## 1.4.2 Second order approximation

To $O(\epsilon)$, the equation for the second order approximation $\psi_1$ has the form

$$\frac{\partial^2 \psi_1}{\partial t \partial y} - \frac{1}{R_\omega}\frac{\partial^3 \psi_1}{\partial y^3} + N_\omega B_y^2 \frac{\partial \psi_1}{\partial y} = U\frac{\partial U}{\partial x} - \frac{\partial \psi_0}{\partial y}\frac{\partial^2 \psi_0}{\partial x \partial y} + \frac{\partial \psi_0}{\partial x}\frac{\partial^2 \psi_0}{\partial y^2}. \tag{1.59}$$

Note that the products of the harmonic functions and derivatives on the right-hand side of (1.59) introduce terms proportional to $\sin 2t$ and $\cos 2t$, as well as steady-state terms. Therefore, the non-linear convective contribution gives rise to time independent terms that are responsible of the steady streaming phenomenon. In order to solve Eq. (1.59) we assume that

$$\psi_1(x, y, t) = U_0\frac{dU_0}{dx}\left(\xi_{1t}(x, y)e^{2it} + \xi_{1s}(x, y)\right), \tag{1.60}$$

where the real part of $U_0(x)$ must be taken. Function $\xi_{1t}$ satisfies the equation

$$\frac{\partial^3 \xi_{1t}}{\partial y^3} - (Ha^2 B_y^2 + 2iR_\omega)\frac{\partial \xi_{1t}}{\partial y} = -\frac{R_\omega}{2}\left[1 - \left(\frac{\partial \xi_0}{\partial y}^2 + \frac{\partial \xi_0}{\partial y}\frac{\partial^2 \xi_0}{\partial x \partial y}\frac{U_0(x)}{U_0'(x)}\right)\right.$$

$$\left. + \xi_0\frac{\partial^2 \xi_0}{\partial y^2} + \frac{U_0(x)}{U_0'(x)}\frac{\partial \xi_0}{\partial x}\frac{\partial^2 \xi_0}{\partial y^2}\right], \tag{1.61}$$

with boundary conditions

$$\xi_{1t}(x, 0) = \frac{\partial \xi_{1t}}{\partial y}(x, 0) = 0 \quad \text{and} \quad \frac{\partial \xi_{1t}}{\partial y} \longrightarrow 0 \quad \text{as} \quad y \longrightarrow \infty. \tag{1.62}$$

The solution is given in the form

$$\xi_{1t}(x, y) = \frac{R_\omega}{4U_0'(x)}\left[\kappa_{t1}e^{-\lambda y} + \kappa_{t2}e^{-\gamma y} + \kappa_{t3}e^{-2\gamma y} + \kappa_{t4}\right], \tag{1.63}$$

with $\gamma = \alpha(x) + i\beta(x)$ and $\lambda = \alpha_t(x) + i\beta_t(x)$, where

$$\alpha_t(x) = \left[\frac{\sqrt{Ha^4 B_y^4 + 4R_\omega^2} + Ha^2 B_y^2}{2}\right]^{\frac{1}{2}}, \quad \beta_t(x) = \left[\frac{\sqrt{Ha^4 B_y^4 + 4R_\omega^2} - Ha^2 B_y^2}{2}\right]^{\frac{1}{2}}.$$

The constants $\kappa_{t1}$, $\kappa_{t2}$, $\kappa_{t3}$, and $\kappa_{t4}$ in (1.63) are defined in the Appendix.

In the limit of a vanishing magnetic field, (1.63) correctly reduces to the hydrodynamic solution [47]. In particular, the contribution to the tangential velocity takes the form

$$\frac{\partial \xi_{1t}(x,y)}{\partial y} = \frac{1}{2}\left[-ie^{-(1+i)\sqrt{2}\eta} + ie^{-(1+i)\eta} - (i-1)\eta e^{-(1+i)\eta}\right]. \tag{1.64}$$

The steady state contribution, $\xi_{1s}$, satisfies the boundary value problem

$$\frac{\partial^3 \xi_{1s}}{\partial y^3} - \lambda_s^2 \frac{\partial \xi_{1s}}{\partial y} = \frac{R_\omega}{4}\left[2 - 2\frac{\partial \xi_0}{\partial y}\frac{\overline{\partial \xi_0}}{\partial y} + \xi_0\frac{\overline{\partial^2 \xi_0}}{\partial y^2} + \overline{\xi_0}\frac{\partial^2 \xi_0}{\partial y^2} + \frac{U_0(x)}{U_0'(x)}\right.$$
$$\left.\left(-\frac{\partial \xi_0}{\partial y}\frac{\overline{\partial^2 \xi_0}}{\partial x \partial y} - \frac{\overline{\partial \xi_0}}{\partial y}\frac{\partial^2 \xi_0}{\partial x \partial y} + \frac{\partial^2 \xi_0}{\partial y^2}\frac{\overline{\partial \xi_0}}{\partial x} + \frac{\overline{\partial^2 \xi_0}}{\partial y^2}\frac{\partial \xi_0}{\partial x}\right)\right], \tag{1.65}$$

$$\xi_{1s} = \xi_{1s}' = 0, \quad \text{at} \quad y = 0, \tag{1.66}$$

$$\xi_{1s}' \longrightarrow 0, \quad \text{as} \quad y \longrightarrow \infty, \tag{1.67}$$

where the overbar stands for complex conjugate quantities and $\lambda_s = Ha^2 B_y(x)$. The solution of equation (1.65) that satisfies the required boundary conditions is

$$\xi_{1s}(x,y) = \frac{R_\omega}{U_0'(x)\kappa_{s6}}\left(\kappa_{s1}e^{-2\alpha y} + 2\kappa_{s2}e^{-\lambda_s y} - e^{-\alpha y}(\kappa_{s4}e^{i\beta y} + \kappa_{s5}e^{-i\beta y}) + \kappa_{s3}\right), \tag{1.68}$$

where constants $\kappa_{sj}(j = 1 \text{ to } 6)$ are defined in the appendix.

When the magnetic field vanishes, Eq. (1.68) and its derivative reduce to

$$\xi_{1s} \approx \frac{13}{8} - \frac{3}{4}\eta - \frac{1}{8}e^{-2\eta} - \frac{3}{2}e^{-\eta}\cos\eta - e^{-\eta}\sin\eta - \frac{1}{2}\eta e^{-\eta}\sin\eta, \tag{1.69}$$

$$\frac{\partial \xi_{1s}}{\partial \eta} = -\frac{3}{4} + \frac{1}{4}e^{-2\eta} + 2e^{-\eta}\sin\eta + \frac{1}{2}e^{-\eta}\cos\eta - \frac{1}{2}\eta e^{-\eta}(\cos\eta - \sin\eta), \tag{1.70}$$

which coincide with the corresponding expressions of ordinary hydrodynamic case [47]. The second order steady velocity component parallel to the wall for the inner layer is

$$u_{1s} = \epsilon_s U_0 \frac{dU_0}{dx}\frac{\partial \xi_{1s}}{\partial y},$$

where $\partial \xi_{1s}/\partial y$ can be obtained from Eq. (1.68) for the MHD case and by Eq. (1.70) for the hydrodynamic case. The latter presents the peculiarity that $u_{1s}$ does not vanish as the distance from the wall tends to infinity. Actually, in the hydrodynamic problem it is impossible to satisfy both the condition $u_{1s} \to 0$ as $\eta \to \infty$ and the no-slip condition at the wall [47, 51]. Therefore, the condition at infinity must be relaxed, making that $u_{1s}$ remains finite when $\eta \to \infty$. Then, the inner velocity at the outer edge becomes

$$\lim_{\eta \to \infty} u_{1s} = -\frac{3}{4}\epsilon_s U_0 \frac{dU_0}{dx}. \tag{1.71}$$
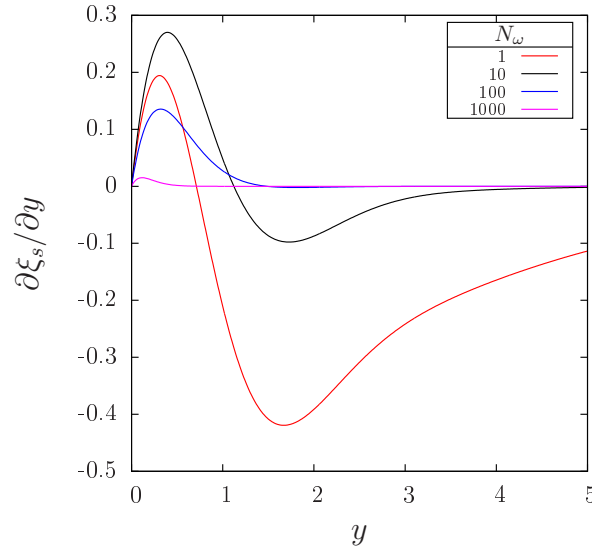
Fig. 1.6: $\partial \xi_{1s}/\partial y$ as a function of the $y$-coordinate for different values of $N_\omega$ at a fixed position within the fringing field ($x = 0.5$). $R_\omega = 10$, $K = 0.8$ and $x_0 = 0.5$.

This means that the steady streaming motion extends beyond the boundary layer into the potential flow. The finite velocity given by (1.71) may be considered as the inner boundary condition for the outer flow [51]. Although far form the magnet edges $\partial \xi_{1s}/\partial y$ tends to the hydrodynamic limit ($-3/4$) as $y \to \infty$, notice that $dU/dx \to 0$ when the magnetic field is negligible. Therefore, the steady streaming disappears in the purely hydrodynamic region. Evidently, $dU/dx$ is also zero in the uniform magnetic field region.

Unlike the hydrodynamic case, when a magnetic field is present the steady solution (1.68) does satisfy the vanishing of the streaming flow as the distance from the walls tends to infinity. This means that the streaming motion does not penetrates from the boundary layer into the potential flow. Figure 1.6 shows the contribution to the tangential velocity $\partial \xi_{1s}/\partial y$ as a function of the $y$-coordinate at a fixed position within the fringing field ($x = 0.5$) for increasing values of $N_\omega$, with $R_\omega = 10$, $K = 0.8$ and $x_0 = 0.5$. It can be observed that as $N_\omega$ increases $\partial \xi_{1s}/\partial y \to 0$ and therefore the steady streaming becomes weaker as the strength of the field grows. This means that the disturbance created by streaming vortices at the extremes of the generator should not affect its performance drastically.

The steady part of the stream function, $\psi_{1s}(x, y) = U_0 \frac{dU_0}{dx}\xi_{1s}$, is shown in Fig. 1.7 as a function of the $x-$coordinate for different values of the constant $x_0$ that modulates the magnetic field gradient. The influence of the fringing region is clearly shown, the largest values of $\psi_{1s}$ occur when the field gradient is more pronounced. This shows that the stronger the

magnetic field gradient the more confined the streaming vortices are and the more intense the flow is. In Fig. 1.8, the streamlines in the fringing field region are displayed for the cases $x_0 = 0.5$ and $x_0 = 1.5$. Two steady recirculations are observed which extend, accordingly to the value of $x_0$, across the zone where the magnetic field passes from a uniform value to zero.
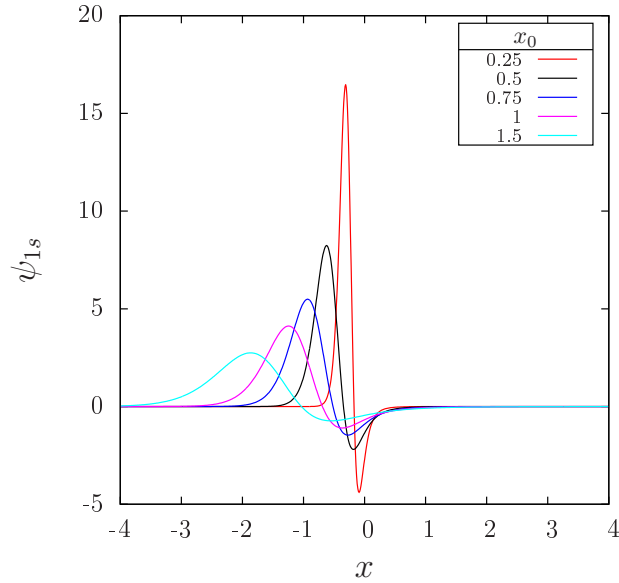
Fig. 1.7: Steady part of the stream function, $\psi_{1s}(x, y) = U_0 \frac{dU_0}{dx} \xi_{1s}$ as a function of the $x$-coordinate at $y = 1$, for different values of the constant $x_0$ that modulates the magnetic field gradient. $R_\omega = 10$, $N_\omega = 10$, $K = 0.8$.
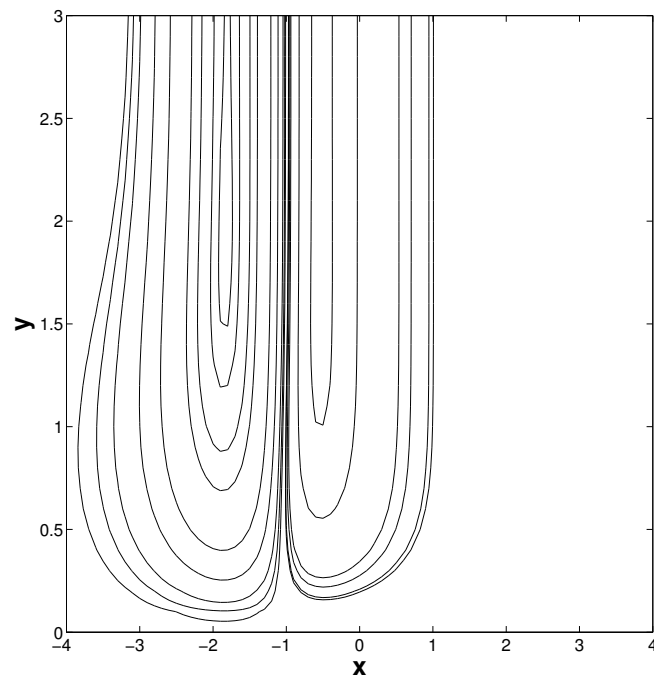
(a)
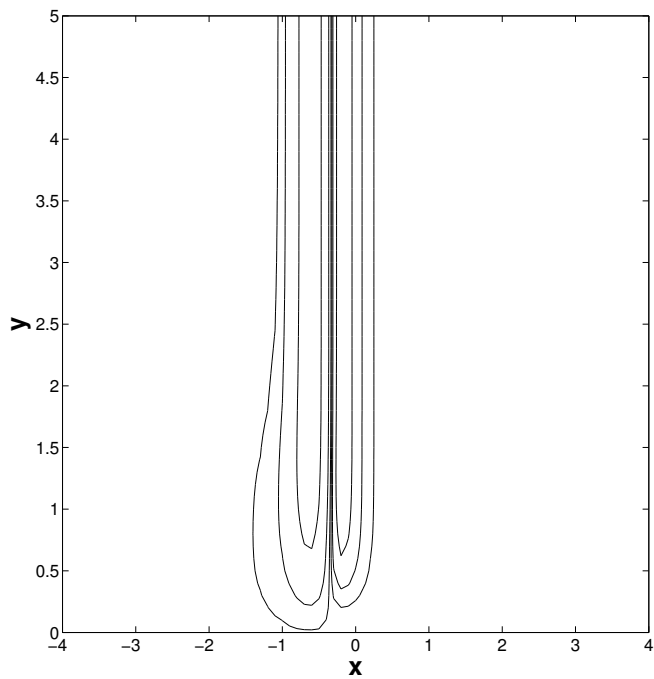


(b)

Fig. 1.8: Stream lines of the steady streaming flow $\psi_{1s}(x,y) = U_0 \frac{dU_0}{dx} \xi_{1s}$ in the region of non-uniform magnetic field. $R_\omega = 10$, $N_\omega = 10$ and (a) $x_0 = 0.5$ and (b) $x_0 = 1.5$.

### 1.4.3   Summary

The finite extension of the applied magnetic field transverse to the electrically insulating duct walls was considered for exploring the flow behavior. The analysis of the entrance oscillatory flow in the fringing field region at the edges of the MHD generator was carried out for high oscillation frequencies using a perturbation method, assuming the small amplitude of oscillation approximation. From the first order solution, the thickness of the boundary layer was estimated, and it resulted a combination of the Stokes and Hartmann layers, each of which are recovered in the corresponding limits. The second order solution revealed that, superimposed to the primary oscillatory flow, a secondary flow composed by a time periodic motion oscillating with twice the original frequency and a steady streaming contribution exist. A pair of steady streaming vortices emerges in the fringing field region as a consequence of non-linear effects caused by the spatial variation of the magnetic field. The extension and intensity of the vortices grow as the magnetic field gradient increases. Unlike the hydrodynamic case, these vortices do not penetrate into the potential flow but remain confined in the boundary layer and, moreover, their strength decreases as the magnetic field becomes stronger. Although the disturbance created by the steady streaming vortices is not expected to affect the performance of the MHD generator, one could conveniently consider a smooth magnetic field gradient for design purposes.

## 1.5  Analytical model of the MHD generator

Now, in order to have a better understanding of the electrical behavior of an alternate MHD generator, an analytical model is presented in this section. The model is focused on determining the behavior of the electric current, the voltage, the electric output power and the electric efficiency of the generator. The starting point is the dimensional system of Eqs. 1.12 - 1.17 simplified by considering a two-dimensional problem. Here we follow the equivalent circuit approach as presented in Ref. [55] for the case of a DC MHD generator. As in the previous sections, it is considered a two-dimensional oscillatory flow of an incompressible, electrically conducting, viscous fluid confined between two insulating parallel walls of infinite length (i.e. we consider only the region where the applied field is uniform) and separated by a distance h=2D under a uniform magnetic field $\mathbf{B} = B_0\hat{\mathbf{y}}$, where $B_0$ is the magnitude of the magnetic field and $\hat{\mathbf{y}}$ is the unit vector in the y-direction, transverse to the walls. We consider the existence of perfectly conducting walls at the distant positions $z = \pm z_0$, connected to an external electric circuit; therefore, there must exist an electric field $E_z$ the value of which depends on the electric circuit conditions. As the magnetic field remains unperturbed, Farady's law of induction reduces to $\nabla \times E = 0$ and the electric field becomes potential. We also assume that there is only an axial velocity component which depends on the transversal coordinate and time $\mathbf{u} = (u(y,t), 0, 0))$, so that continuity equation satisfies identically. The flow is driven by a periodic presure gradient set at the extremes of the duct which can be expressed as the real part of $-dp/dx = Ge^{i\omega t}$. Therefore, we assume that the velocity and electric field are also harmonic fuctions of $t$, that is, $\mathbf{u} = (u_0(y)e^{i\omega t}, 0, 0)$ and $\mathbf{E} = (0, 0, E_{z0}e^{i\omega t})$, where $E_{z0}$ is a constant. Neglecting the transient flow, the solution of momentum equation that satisfies no-slip boundary conditions, $u(-D) = 0$ and $u(D) = 0$ is

$$u(y,t) = u_0 e^{i\omega t} = U_m \lambda_1 \left( \frac{\cosh \lambda_1 - \cosh \lambda_1 \frac{y}{D}}{\lambda_1 \cosh \lambda_1 - \sinh \lambda_1} \right) e^{i\omega t} \tag{1.72}$$

where $\lambda_1 = \sqrt{Ha^2 + iR_\omega}$ and $U_m$ is the spatial average of the velocity profile in the cross-section given by

$$U_m = \frac{1}{2D} \int_{-D}^{+D} u_0 dy = \frac{D^2}{\lambda_1^2} \left( \frac{G}{\mu} + \frac{Ha}{D} \sqrt{\frac{\sigma}{\mu}} E_{z0} \right) \left( \frac{\tanh \lambda_1}{\lambda_1} - 1 \right) \tag{1.73}$$

The current induced in the generator due to the interaction of the oscillating conducting liquid and the applied magnetic field is given by Ohm's law, that is

$$J_z = J_{z0} e^{i\omega t} = \left( \sigma E_{z0} + \sigma u_0 B_0 \right) e^{i\omega t}, \tag{1.74}$$

$$J_{z0} = \sigma E_{z0} + \sigma B_0 U_m \lambda_1 \left( \frac{\cosh \lambda_1 - \cosh \lambda_1 \frac{y}{D}}{\lambda_1 \cosh \lambda_1 - \sinh \lambda_1} \right), \tag{1.75}$$

or, in terms of the Hartmann number

$$J_{z0} = \sigma E_{z0} + \frac{Ha U_m \lambda_1 \sqrt{\sigma\mu}}{D}\left(\frac{\cosh\lambda_1 - \cosh\lambda_1\frac{y}{D}}{\lambda_1\cosh\lambda_1 - \sinh\lambda_1}\right). \tag{1.76}$$

The total induced electric current per unit length that can be extracted from the generator through an external electrical load resistance, $R_c$, connected to the terminals of the generator, is given by

$$\frac{I}{L} = \frac{I_0 e^{i\omega t}}{L}, \tag{1.77}$$

$$\frac{I_0}{L} = \int_{-D}^{D} J_{z0}dy = \int_{-D}^{D}\left(\sigma E_{z0} + \frac{Ha U_m \lambda_1 \sqrt{\sigma\mu}}{D}\left(\frac{\cosh\lambda_1 - \cosh\lambda_1 y/D}{\lambda_1\cosh\lambda_1 - \sinh\lambda_1}\right)\right)dy, \tag{1.78}$$

$$\frac{I_0}{L} = 2D\sigma E_{z0} + 2Ha U_m \sqrt{\sigma\mu}, \tag{1.79}$$

where $I$ is the total current passing through the external circuit and $L$ is the length of the electrodes. The terminal voltage between the electrodes that are located at $z = -b$ and $z = b$ is given by

$$\Phi_T = \Phi_{T0}e^{i\omega t} = -\int_{-b}^{b} E_0 e^{i\omega t}dz, \tag{1.80}$$

$$\Phi_{T0} = -\int_{-b}^{b} E_{z0}dz, \tag{1.81}$$

$$\Phi_{T0} = -2bE_{z0}. \tag{1.82}$$

Taking $E_{z0}$ from equation (1.79) and substituting it in equation (1.82), we get

$$\Phi_{T0} = \left(\frac{-bI_0}{LD\sigma} + \frac{2Ha U_m b\sqrt{\mu/\sigma}}{D}\right). \tag{1.83}$$

A common approach to model an MHD generator is to visualize it as an equivalent circuit so that the relevant electrical parameters are easily calculated . The equivalent circuit can be determined from the Thevenin's theorem which states that any array of batteries and resistances with two output terminals can be replaced by an internal resistance and a battery (voltage source) in series [55]. The equivalent voltage source is the electric potential in the output terminals when the electric current is zero, that is, the open circuit voltage. In turn, the equivalent or internal resistance is obtained as the ratio of the equivalent voltage to the electric current when the load resistance is zero, that is, to the short circuit current. Hence, if $I_0 = 0$ we obtain the equivalent voltage source (open circuit voltage) in the form

$$\Phi_{0oc} = \frac{2Ha U_m b\sqrt{\mu/\sigma}}{D}. \tag{1.84}$$

In turn, if the terminal voltage is zero, $\Phi_{T0} = 0$, we get the short circuit current that is

$$I_{0sc} = 2HaU_mL \sqrt{\mu\sigma}. \tag{1.85}$$

Therefore, the equivalent or internal resistance of the MHD generator can be obtained as follows

$$R_i = \frac{\Phi_{0oc}}{I_{0sc}} = \frac{b}{DL\sigma}. \tag{1.86}$$

Applying the Kirchhoff's law of voltages to the equivalent circuit we obtain

$$\Phi_{0oc} - I_0(R_i + R_c) = 0, \tag{1.87}$$

and therefore,

$$I_0 = \frac{2HaU_mb \sqrt{\mu/\sigma}}{D} \left( \frac{1}{R_i + R_c} \right), \tag{1.88}$$

where $R_c$ is the external resistance of the circuit. Combining equations (1.79) and (1.88) we can obtain the value of $E_{z0}$ in the form

$$E_{z0} = -\frac{HaU_m \sqrt{\mu/\sigma}}{D}K, \tag{1.89}$$

where $K$ is the load factor of the generator defined by

$$K = \frac{1}{1 + R_i/R_c}. \tag{1.90}$$

Since $E_{z0}$ depends on the total ohmic resistance of the circuit, the load factor offers a measure of the relative importance of the electrostatic field caused by the external load and the electromotive force induced by the motion of the liquid in the magnetic field. When $K = 1$, the open circuit condition is obtained, which means that the load resistance is much larger than the internal resistence ($R_c \to \infty$) and the current closes its trajectories inside the generator, that is, the current circulates within the liquid metal. If $K = 0$, the short circuit condition is obtained, which means that the load resistance is much smaller than the internal resistence ($R_c \to 0$) and the current circulates without restriction through the circuit. In terms of the load factor, the total current and the current density can be expressed in the form

$$I_0 = \frac{2HaU_mb \sqrt{\mu/\sigma}}{DRi}(1 - K), \tag{1.91}$$

$$J_{z0} = \frac{HaU_m \sqrt{\mu\sigma}}{D} \left[ -K + \lambda_1 \left( \frac{\cosh \lambda_1 - \cosh \lambda_1 y/D}{\lambda_1 \cosh \lambda_1 - \sinh \lambda_1} \right) \right]. \tag{1.92}$$

We can calculate now the total output power of the generator that is given by

$$Pe = \int_V \mathbf{J} \cdot \mathbf{E}dV = \int_v \mathfrak{R}[J_z]\mathfrak{R}[E_z]dV \tag{1.93}$$

where $V$ denotes the volume and $\Re[]$ indicates the real part of the expression in brackets. Explicitly, the output power takes the form

$$P_e = \frac{\Phi_{oc}^2}{R_i}[1 - K]K\cos^2\omega t. \tag{1.94}$$

From the equations expressed above, it can be seen that both the voltage and the total electric current are directly proportional to the spatial average velocity of the fluid and the magnitude of the magnetic field. It can also be seen that the electrical output power is proportional to the square of the averaged velocity and the square of the magnetic field. The maximum electrical output power is obtained when $K = 0.5$, or in other words, when the internal resistance of the generator equals the load resistance ($R_c = R_i$). On the other hand, the mechanical flow power necessary to counteract the Lorentz force exerted on the fluid due to its motion under the applied magnetic field is given by the real part of the integral

$$P_f = \int_V (\mathbf{J} \times \mathbf{B}) \cdot \mathbf{u} dV \tag{1.95}$$

It is common to define the electrical isotropic efficiency of the generator as the ratio of the output electric power, $P_e$, and the push power, $P_f$, integrated over the total volume V of the MHD channel. In the case of an alternate MHD generator, time integration over a whole period, (or an integer number of periods) must also be performed, namely [44]

$$\eta_e = \frac{\frac{\omega}{2\pi}\int_0^{2\pi/\omega} P_e dt}{\frac{\omega}{2\pi}\int_0^{2\pi/\omega} P_f dt}. \tag{1.96}$$

$\eta_e$ gives the fraction of the mechanical work done by the fluid in overcoming the magnetic force that is converted into useful electric power. Eq. (1.96) involves integration over the total volume V. Since $P_e$ and $P_f$ contain products of harmonic functions of time, both a time harmonic contribution and a steady part exist. The former disappears after time integration, while the latter gives a non-zero value. Figures 1.9, 1.10 and 1.11 show the electric isotropic efficiency as a function of the oscillatory Reynolds number ($R_\omega$), the Hartmann number ($Ha$) and the load factor ($K$), respectively. In figure 1.9 the electrical efficiency, Eq. (1.96), as a function of $R_\omega$ is shown for maximum output power conditions, i.e., $K = 0.5$, and different Hartmann numbers (1, 10, 50, 100). The scale in the ordinate axis is amplified to observe the slight changes in $\eta_e$ that take place from $R_\omega = 10^1$ to $10^6$. The behavior of the four curves is very similar, the efficiency $\eta_e$ tending to the asymptotic value 0.5 for $R_\omega$ larger than $10^6$. In fact, this behavior is typical of an ideal MHD Faraday generator at high Hartmann numbers where the electrical efficiency tends to the load factor value, $\eta_e \to K$. This is also observed in figure 1.10, where $\eta_e$, scaled by $K$, is plotted versus the Hartmann number for different load factor conditions and $R_\omega = 15$. Figure 1.11 displays $\eta_e$ versus the load factor for four Hartmann number values (1, 10, 50, 100) and $R_\omega = 15$. It can

be observed that the maximun output power ($K = 0.5$) does not coincide with maximum efficiency.
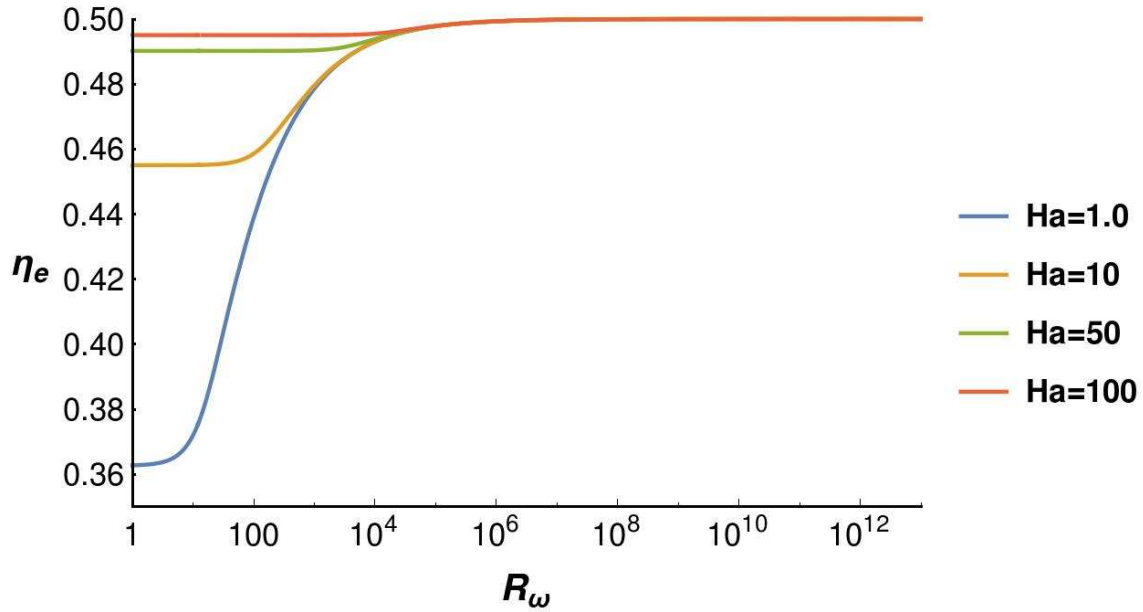


Fig. 1.9: Electric isotropic efficiency of the alternate MHD generator as a function of $R_\omega$ for maximum output power condition ($K = 0.5$) and different Hartmann numbers.
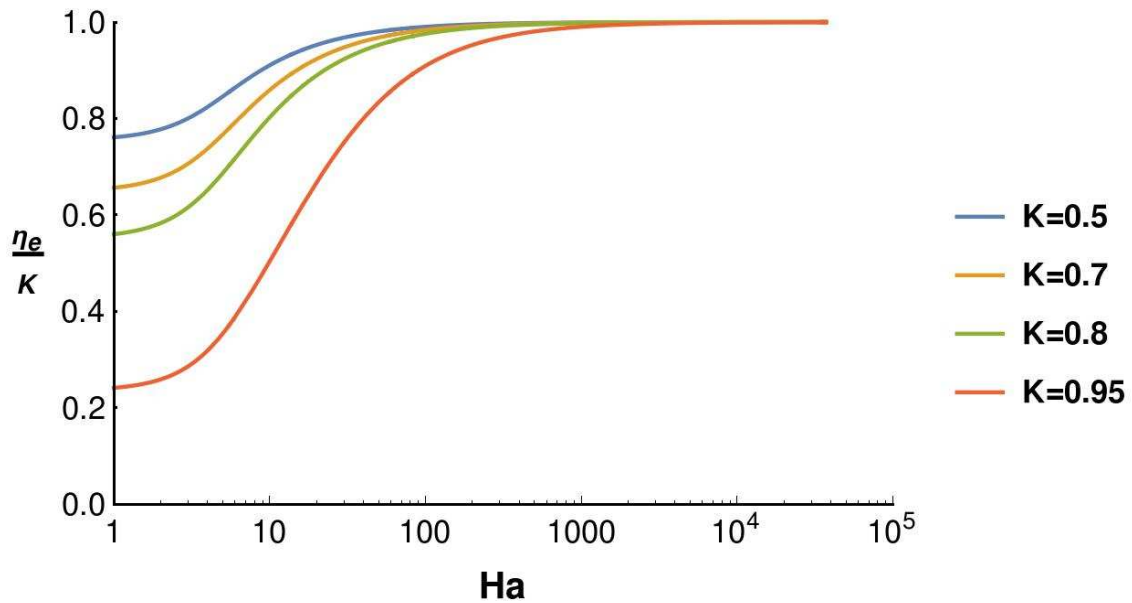


Fig. 1.10: Electric isotropic efficiency of the alternate MHD generator as a function of $Ha$ for different load factors and $R_\omega = 15$ .
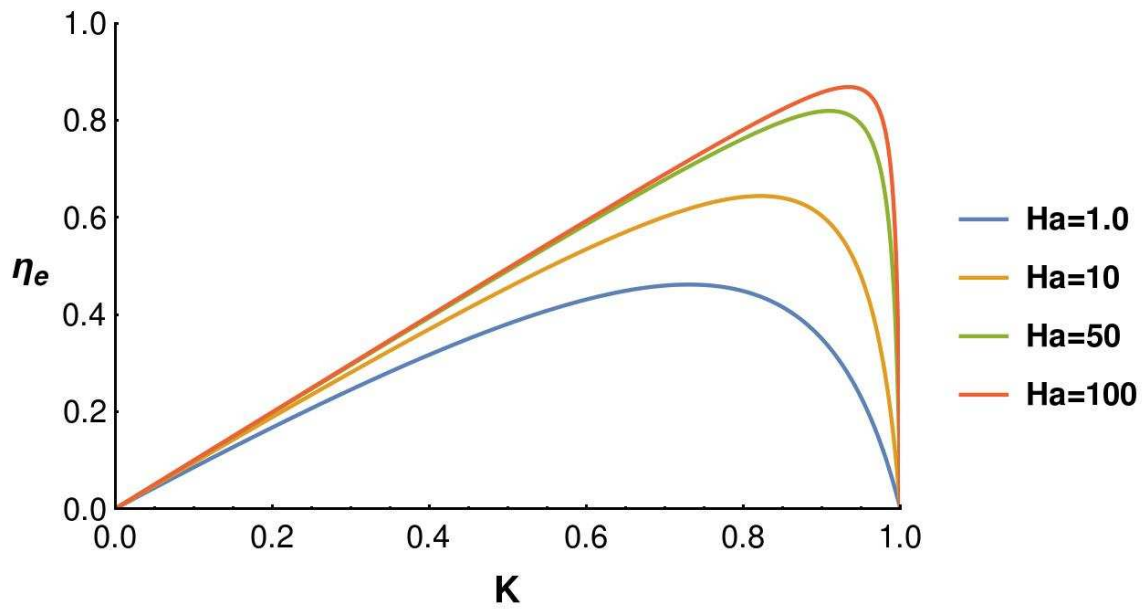
Fig. 1.11: Electric isotropic efficiency of the alternate MHD generator as a function of $K$ for different Hartmann numbers and $R_\omega = 15$.

Despite the simplifications introduced, the analytical model offers a suitable description of the electrical behavior of the generator and provides a better undertstanding of the underlying physical phenomena.

# Chapter 2

# Experimental design

This chapter presents the design of a laboratory-scale alternate LMMHD generator. The prototype involves three main systems: the impeller system, the oscillation duct and the measurement system. The impeller system generates the oscillatory motion that is transferred to the liquid metal, simulating the periodic motion of the waves. The oscillation duct is where the oscillatory liquid metal is confined and comprises the MHD generator that transform the oscillatory motion of the conducting fluid into electricity. In addition, the measurememnt system includes the adaptations made in the prototype with the aim of analyzing quantitatively the flow dynamics of the oscillating liquid metal as well as performing the electrical characterization of the device. The complementary devices include the drain and the leveling system.

## 2.1   Impeller system

The impeller system transfers the oscillatory motion to the working fluid. This can be accomplished by transforming the angular motion of an electric motor into a linear oscillatory motion through a connecting rod-crank-sliding mechanism. For this purpose, an electric motor Baldor AP7401 with 1725 RPM and 0.13 HP was used. With the aim of improving the control of the RPM delivered by the electric motor, it was required to couple it with a gearbox with a ratio of 1/60. The gearbox decreases the RPM and increases the torque, allowing to overcome the friction of the piston at low revolutions. The gearbox is connected to a rod-crank mechanism which has a special design so that the amplitude of the movement can vary bettwen 5 cm - 10 cm. The crank is 22 cm long and is attached to a piston with 2 inches in diameter which is in direct contact with the working fluid, enabling to transfer the linear oscillatory movement to the liquid metal contained in the MHD duct. The piston housing has a flange on one of its ends with the purpose of joining mechanically the MHD duct with the impeller system. Since a fluid is involved, avoiding leaks in the whole device is of vital importance, therefore, the piston and the joint flange have

mechanical seals which prevent spills. Figure 2.1 shows a sketch of the impeller system.
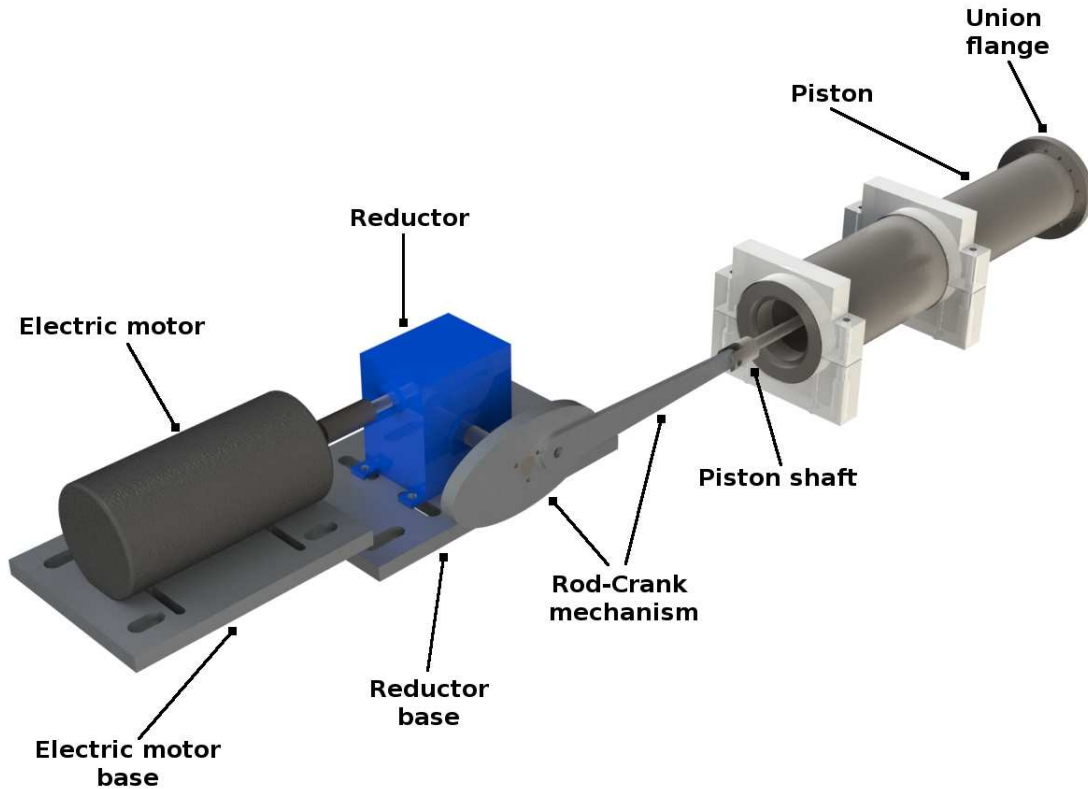


Fig. 2.1: Experimental impeller system

## 2.2   Oscillation duct

The liquid metal in oscillatory motion is confined in a duct with a rectangular cross section. The duct is 755 mm long and is composed of two acrylic plates one on top of the other and joined by screws. In the bottom plate, a cavity of rectangular cross-section of 60 mm width and 12 mm height was engraved. A linear seal was placed between the two plates along the whole duct so that when the two plates are attached by screws the linear seal is pressed creating a mechanical seal to prevent leakage. The flange-union, which joins the oscillation duct with the impeller system, is located at one end of the duct. The measuring zone, which consists of an area open to the atmosphere where the UDV probe can be entered into the

liquid metal, is located at the other end of the duct. To ensure the absence of splilling, this area has vertical walls that allow the liquid metal to oscillate in the vertical direction, as an oscillating column. In the middle zone of the duct the MHD generator (or MHD transducer) is located, which transforms the energy of the oscillating conductive fluid into electrical energy. The main components of the MHD transducer include two permanent magnets with the shape of a rectangular prism 120 mm long, 80 mm wide and 7 mm high, and magnetized in the direction normal to the larger face. The magnets are placed in special receptacles engraved on the top and bottom walls of the duct so that they remain parallel forming a magnetic field configuration with north and south poles in the gap between them. In addition, copper electrodes also with a shape of rectangular prisms 130 mm long, 100 mm wide and 12 mm high are inserted on the duct forming the lateral walls that constitute the electrodes of the generator. Figure 2.2 shows the oscillation duct in isometric view while Fig. 2.3 shows a cross-section view of the MHD transducer.
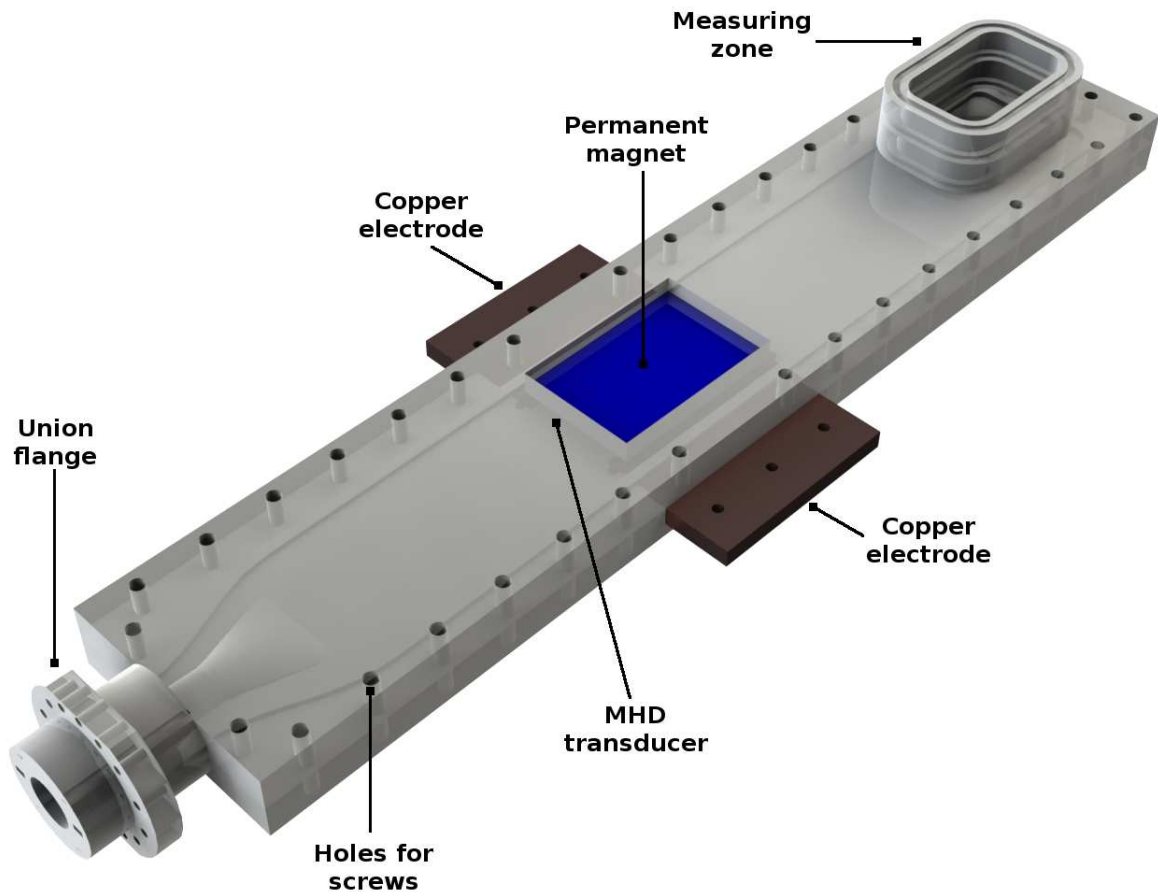
Fig. 2.2: Isometric view of the oscillation duct.
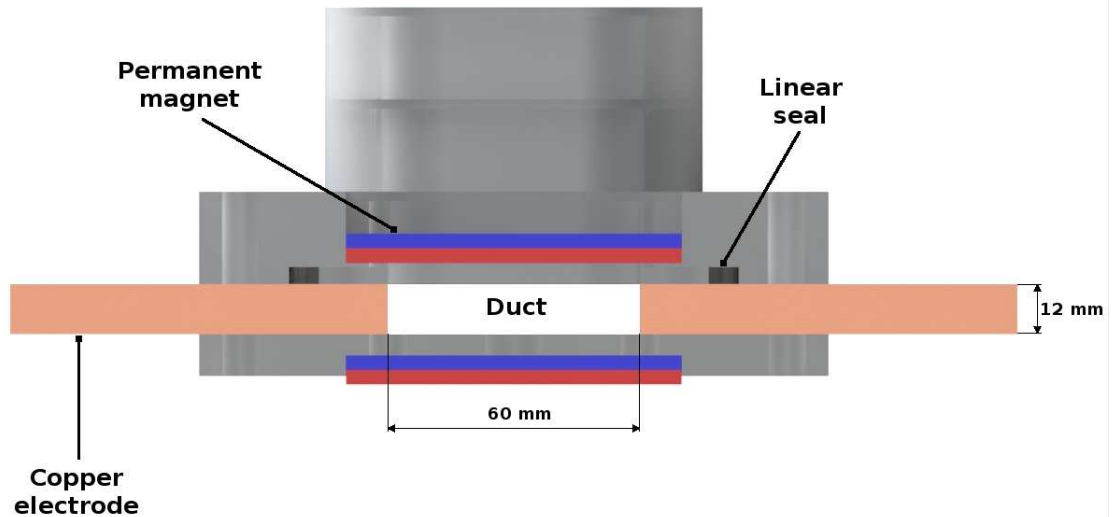
Fig. 2.3: Cross-section view of the MHD transducer. Blue and red colors in the permanent magnets indicate the north and south polarities, respectively.

## 2.3   Measuring system

In order to perform the flow and electrical characterization of the experimental device, it was necessary to design implements which allow to carry out detailed measurements. Since the liquid metal is an opaque medium, it is not possible to use optical techniques to measure the velocity field. A suitable alternative is the use of acoustic techniques such as the Ultrasound Doppler Velocimetry (UDV) applied in the present work, that in the last decades has consolidated as the most used technique for velocity measurements in liquid metals [56, 57]. UDV is based on the pulse-echo method and the measurement requires acoustic inhomogeneities in the fluid such as oxides found in pure metals or alloys. In the simplest implementation, as the one used in the present work, an ultrasonic measuring

system utilizes a single ultrasound transducer that serves as emitter as well as receiver of acoustic waves. It emits short ultrasonic pulses which propagate in direction of the normal of the transmission plane (the acoustic axis) as a longitudinal wave with the sound velocity of the media. By registering the differences in transit time of the scattering echos between consecutive pulse emissions, resulting from a finite shift of particle position, the movement of the scattering particles and consequently a profile of the axial velocity component in the propagation direction can be determined. A detailed explanation of the operation principle of UDV can be found in Ref. [58] from where the previous synthesis was extracted. To implement this technique, it was necessary to design a tool able to hold the UDV transducer and to vary the position of the transducer acoustic axis to perform the measurements in the liquid metal. This implement consists of a fixed base, a rotating mount and a support for the transducer. The fixed base is secured to the duct by screws. The rotating mount allows to vary the angle of the measurement axis (acoustic axis) with respect to the main longitudinal axis of the oscillation duct, making possible to measure at different transverse positions (i.e along the width of the duct). The transducer support is the link between the UDV transducer and the rotating mount. Figure 2.4 shows in detail the device used for the velocity measurement in the liquid metal.
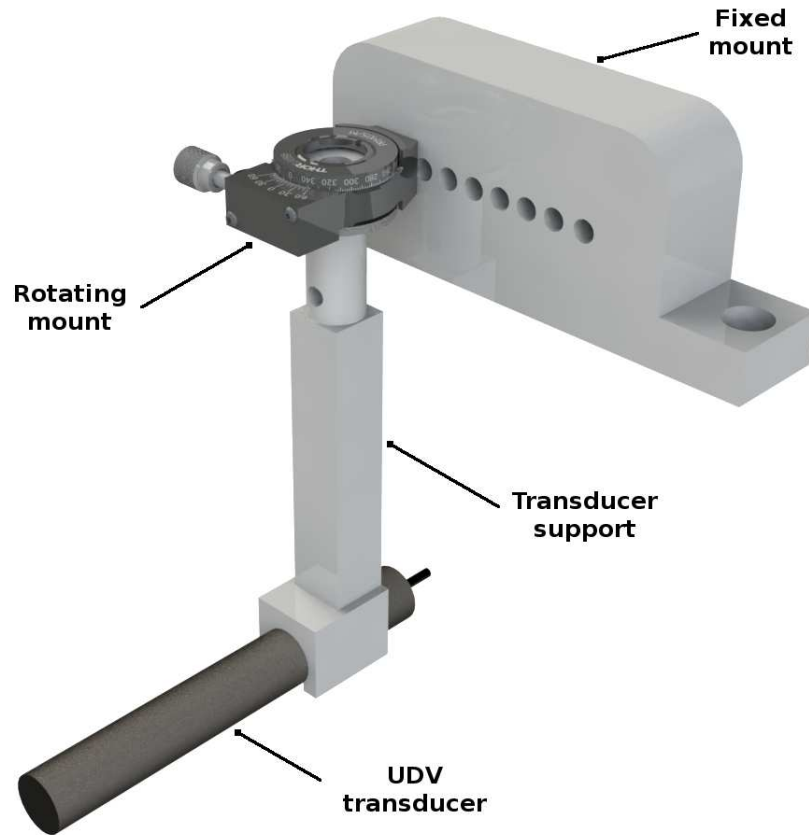
Fig. 2.4: Isometric view of the measuring device for the velocity measurement of the liquid metal using the UDV transducer.

The electrical output of MHD generators is characterized by delivering low voltages and high currents, which results problematic when making measurements with traditional devices (multimeters). The main complication arises when measuring currents, since the resistance of multimeters is much greater than the internal resistance of the generator ($K \approx 1$), causing the currents to short-circuit inside the generator while only a small portion of them is measured by the multimeter. To avoid this problem the current is inferred by a Hall effect sensor, whose output voltage is related to the induced magnetic field in a conductor (variable electric load ) through which the electric current delivered by the MHD generator passes. An array of copper bars (one of which can be varied) were used as electric load so that its electric resistance was approximately of the same order of magnitude as the internal resistance of the generator, allowing the measurement of considerable electric current values. Figure 2.5 shows an isometric view of the external electric load with the Hall effect
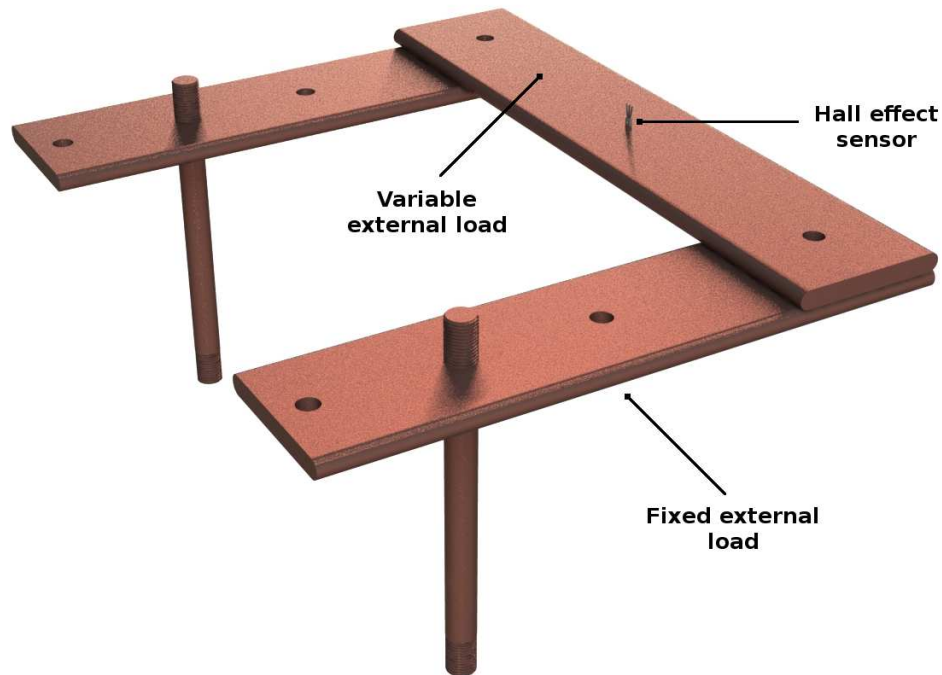
sensor.



Fig. 2.5: Isometric view of the total external electric load with the Hall effect sensor.

## 2.4 Complementary devices

An important part of the experimental prototype is the drain, since it allows to remove all the liquid from the oscillation duct and thus be able to clean the experiment or make any required change. The drain of the oscillation duct is made through a gate valve, which is located near the measurement zone. Another important issue is the leveling of the entire experimental device which is accomplished by means of special supports that can modify the vertical position of the oscillation duct and piston as well as of the reductor and the electric motor. The oscillation duct and the piston are supported by five equal bases, while the electric motor and the gearbox are supported by two similar bases. Figure 2.6 and 2.7 show the two different supports used to level the experimental device.
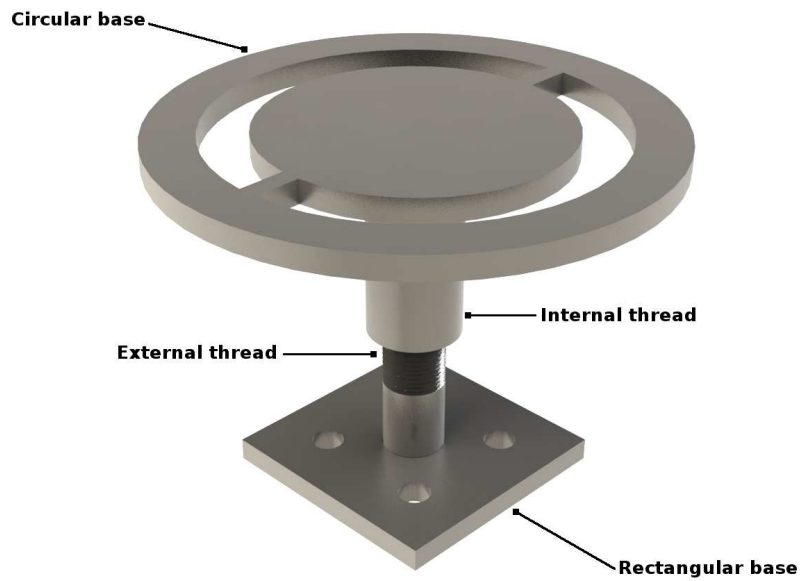
Fig. 2.6: Isometric view of the leveling mechanism of the duct and the piston.
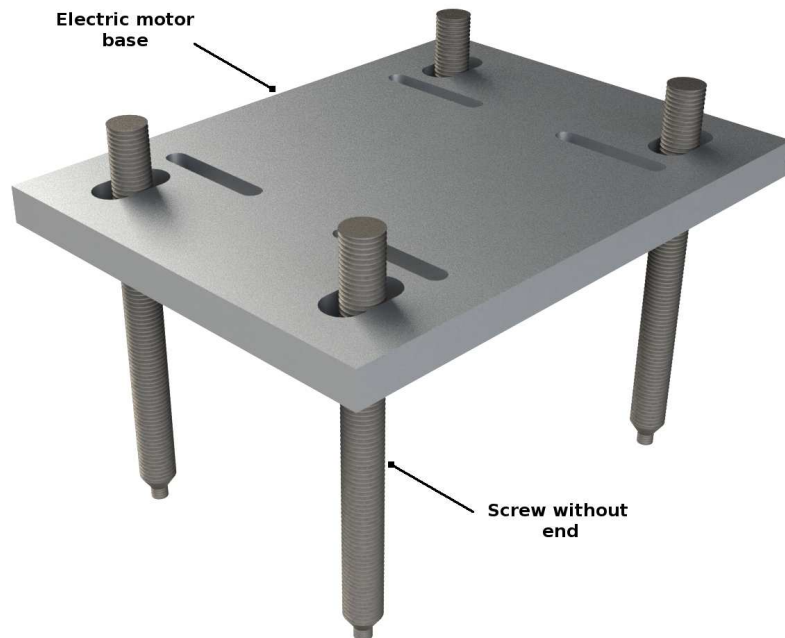


Fig. 2.7: Isometric view of the leveling mechanism of the reductor and the electric motor.
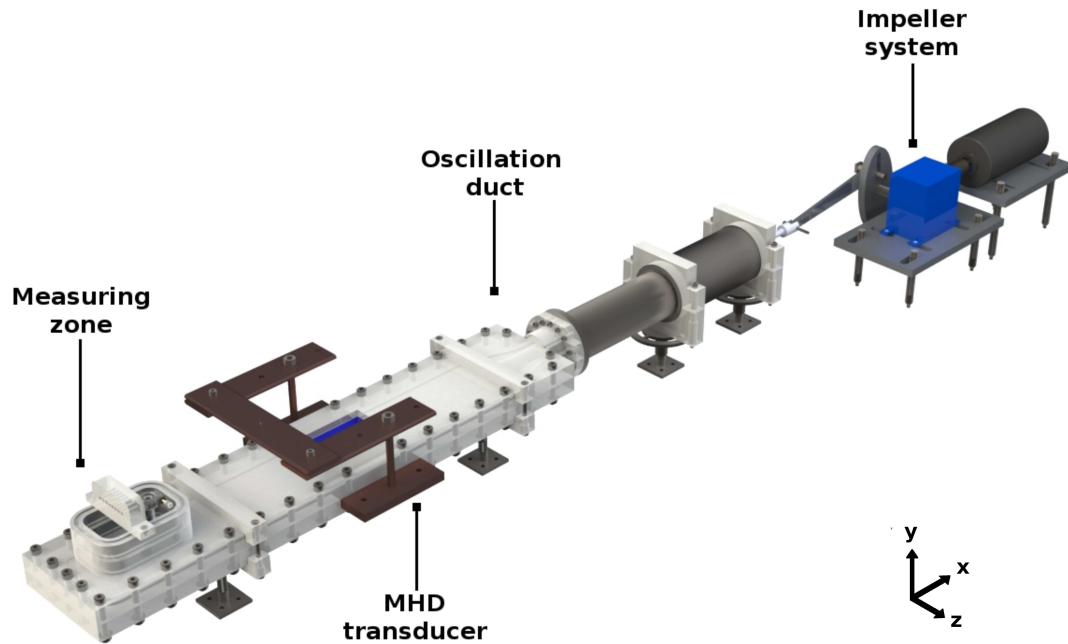
Fig. 2.8: Isometric view of the design of the complete experimental prototype of an alternate LMMHD generator at laboratory scale.

Figure 2.8 shows the integration of the different systems of the prototype of the alternate LMMHD generator at laboratory scale. Based on this design, all the components were built and assembled in the MHD Laboratory of the Renewable Energy Institute, UNAM. A photograph of the prototype, mounted on an optical table, is shown in figure 2.9.
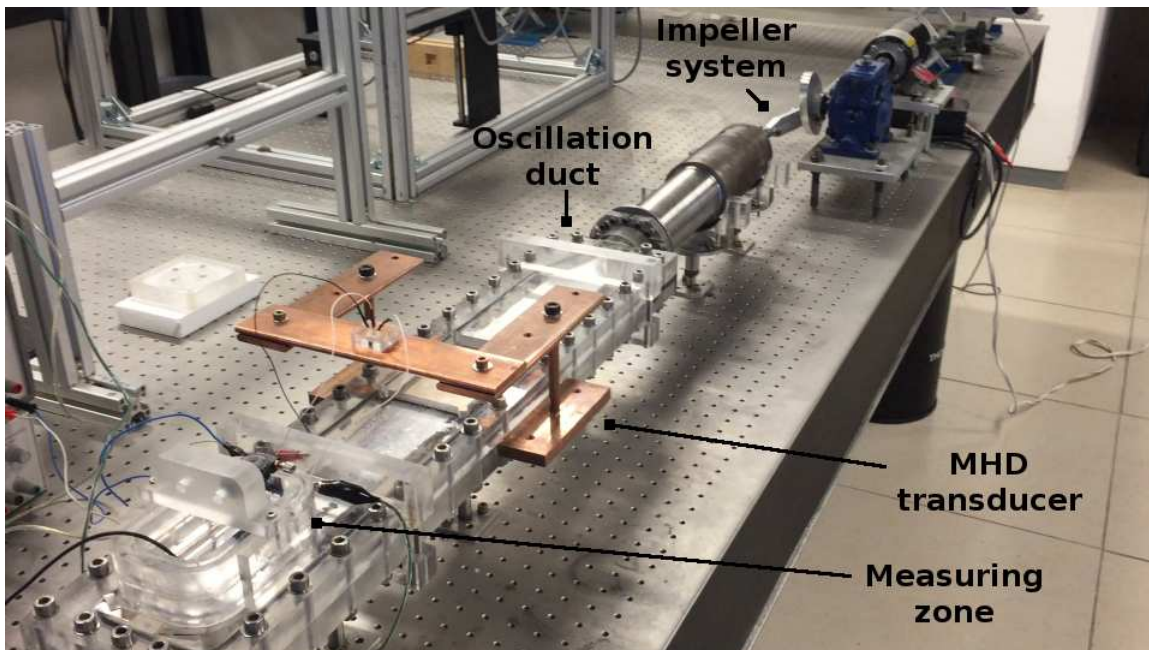
Fig. 2.9: Photograph of the experimental prototype of the alternate LMMHD generator assembled at the MHD laboratory of the Renewable Energy Institute of UNAM.

# Chapter 3

# Experimental methodology

As previously mentioned, the purpose of the experimental prototype is to characterize both the electrical response of the alternate LMMHD generator as well as the flow dynamics that take place in the oscillation duct. In this chapter a description of the experimental methodology implemented to perform the aforementioned characterizations is presented.

## 3.1   Experimental conditions

According to the experimental design presented in the previous chapter, the results obtained from the operation of the prototype are in function of different parameters, such as the oscillation frequency and amplitude of the piston, the magnitude and distribution of the applied magnetic field, the external electrical load and the physical properties of the electrically conductive liquid. It has to be mentioned that due to the nature of the rod-crank-slide mechanism, the motion transmitted to the liquid metal in the oscillation duct is not a fully uniform periodic motion. As previously mentioned, the impeller system is responsible for transforming the rotary movement of an electric motor into linear oscillatory motion, which is transferred to the electrically conductive liquid by a piston. Given the specifications of the components of the impeller system, it is possible to reach oscillation frequencies in the range of 0.02-0.5 Hz. This range of experimental frequencies comprises values that can be found in waves of the Mexican coasts [59, 60]. In turn, the amplitudes of the oscillating motion that can be obtained with the experimental device are in the range of 5-10 cm.

On the other hand, the applied magnetic field is provided by a pair of parallel neodymium permanent magnets of rectangular shape separated by a distance of 22 mm. This magnetic field configuration grants a maximum magnetic field strength of 180 mT at a distance of 11 mm from the surface of the magnets (center of the duct). Figure 3.1 shows the distribution of the magnetic field configuration at the mid plane of the duct. Note that although the permanent magnets are suposed to have a uniform magnetization, the distribution of mag-

netic field is not homogeneous, the stronger intensities being confined at the corners while
a weaker intensity is found at the central zone.
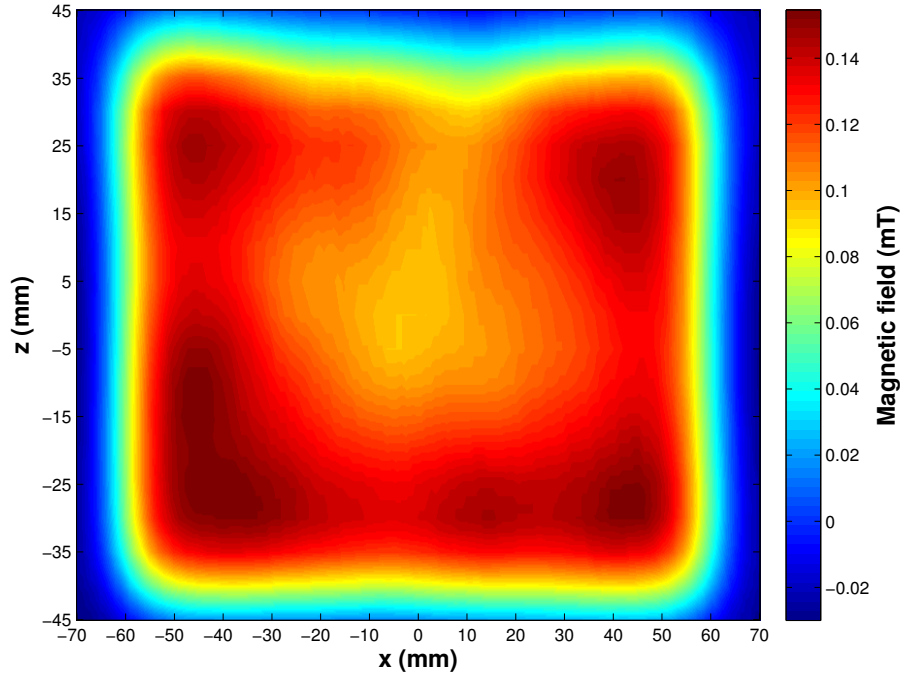


Fig. 3.1: Magnetic field distribution obtained at the mid plane of the duct with two parallel
neodymium magnets of rectangular shape.

The liquid metal used to perform the characterization of the experimental device is an
eutectic alloy based on gallium, indium and tin (Galinstan) that remains in the liquid phase
at room temperature. Table (3.1) shows the physical properties of Galinstan.

| | |
|---|---:|
| Density [$kg\ m^{-3}$] | 6360 |
| Dynamic viscosity [$kg\ m^{-1}s^{-1}$] | $2.2 \times 10^3$ |
| Kinematic viscosity [$m^2\ s^{-1}$] | $3.3 \times 10^{-7}$ |
| Surface tension [$N\ m^{-1}$] | 0.533 |
| Electrical conductivity [$\Omega^{-1}\ m^{-1}$] | $3.46 \times 10^6$ |
| Sound velocity [$m\ s^{-1}$] | 2725 |
| Magnetic permeability [$N\ A^{-2}$] | $4\pi \times 10^{-7}$ |
| Melting temperature [$^\circ C$] | 10.5 |

Table 3.1: Physical properties of $Ga^{68\%}In^{20\%}Sn^{12\%}$ at 20 $^\circ C$.

In order to have an idea of the physical conditions prevailing in the experiment, it is convenient to estimate the relevant dimensionless parameters defined in section 1.2. For instance, the oscillatory Reynolds number is given by $R_\omega = \omega h^2/\nu$, where $\omega = 2\pi f$ is the angular frequency, while $f$ is the forcing frequency and $h$ is the characteristic length scale of the flow. Taking into account the range of the experimental forcing frequency ( 0.02-0.5 Hz) and considering the characteristic length scale as half the distance between the upper and lower walls transverse to the magnetic field ($h = 6$ mm), we get that the oscillation Reynolds number varies in the range $R_\omega = 14 - 300$. In turn, considering the spatial average of the magnetic field strength at the mid plane of the duct and in the area of the electrodes ($B_0 = 100$ mT) the Hartmann number can be estimated as $Ha = B_0 h \sqrt{\sigma/\rho\nu} = 24$, confirming the dominance of magnetic forces over viscous forces. Finally, it can be estimated that the amplitude parameter varies in the range $R = Gh^3/\rho\nu = 0.003 - 0.84$, where the amplitude of the pressure gradient, $G$, can be deduced from the volumetric flow rate $Q$. Since the nonlinear term in the equation of motion is of the order $R/R_\omega^2$ (see equation 1.20) the variation range of the oscillation Reynolds number and the amplitude parameter indicates that nonlinear effects are small ($< 10^{-5}$) and, therefore, result negligible under the experimental conditions.

## 3.2   Experimental measurements

In the following subsections, the methodology used to perform the characterization of the flow dynamics and electrical performance of the alternate LMMHD generator is presented.

### 3.2.1   Flow measurements

To carry out the axial velocity measurements in the experimental device, the technique of Ultrasonic Doppler Velocimetry (UDV) was applied. The UDV 3010 Signal Processing system with the transducer TR0810LS of 8 MHz were used [61]. The trasducer is attached to the flow measurement implement described in the previous chapter that can move along the width of the duct, so that the axial velocity can be measured in the central region as well as close to the lateral walls. Acoustic reflection problems were found when measurements were made in the central area of the oscillation duct, so it was not possible to make quality measurements in this zone. These problems are produced by the acoustic waves reflected in the metal face of the piston, which is aligned normal to the direction of the sound wave. To avoid the reflections, measurements were made near the side walls of the channel by placing first the transducer in the normal direction to the main flow and then varying the direction of the transducer (acoustic axis) with a certain angle with respect to the main flow direction. By taking the projection in this direction, the axial velocity component is obtained. Figure 3.2 shows the initial location of the UDV transducer near the side wall of the oscillation duct and the measuring or acoustic axis (dotted line) along the duct. Note

that measurements are taken not only in the region affected by the magnetic field but also outside of this region. The variation of the angle between the transducer acoustic axis and the direction of the main flow allows to have values of the axial velocity component for different positions in the transversal $z$-direction, making it possible to calculate the average axial velocity of the flow. Figure 3.3 shows examples of the trajectory of the acoustic axis for different measurement angles in the oscillation duct. Measurements were made by placing the transducer close to both side walls of the duct while eight different measuring angles were used on each side, which correspond to 0°, 1°, 2°, 3°, 4°, 5°, 6° and 7°. Flow measurements were made for different oscillation frequencies and amplitudes of the piston.
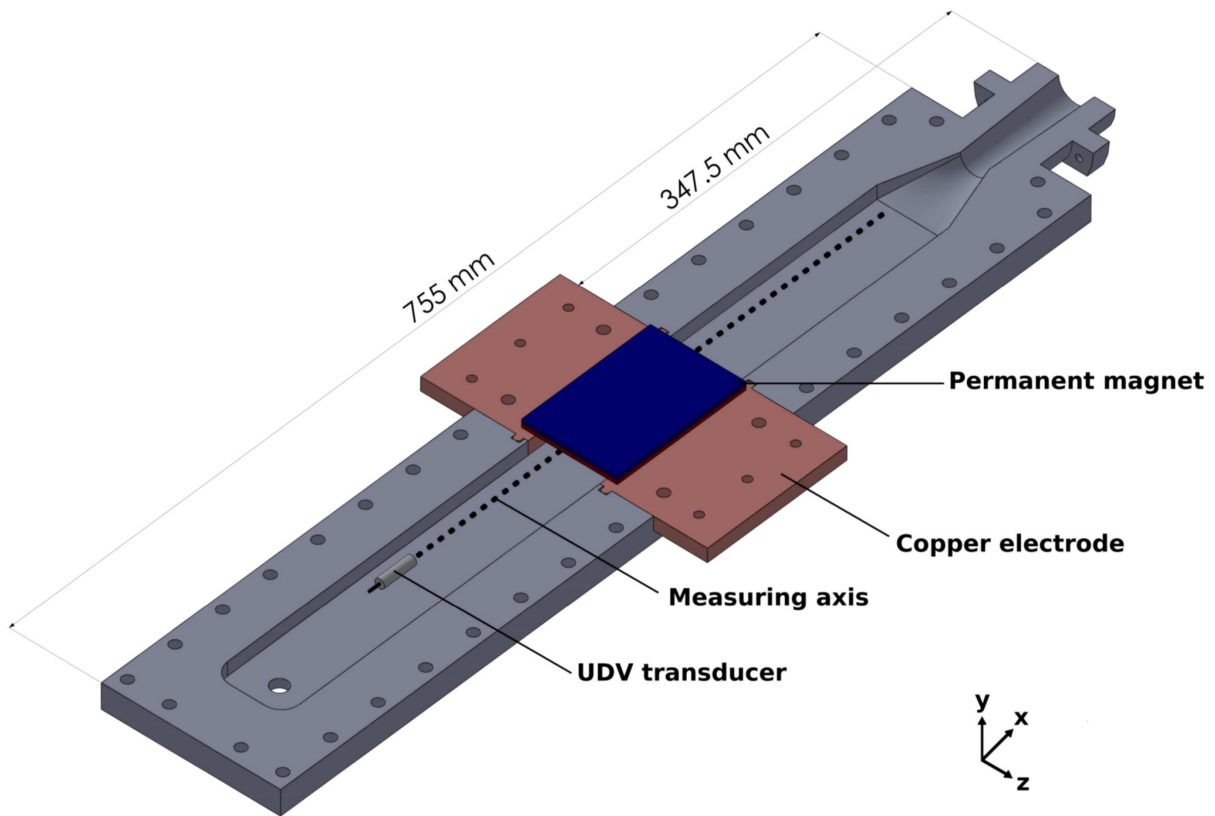


Fig. 3.2: Sketch of the location of the UDV transducer to perform axial velocity measurements.
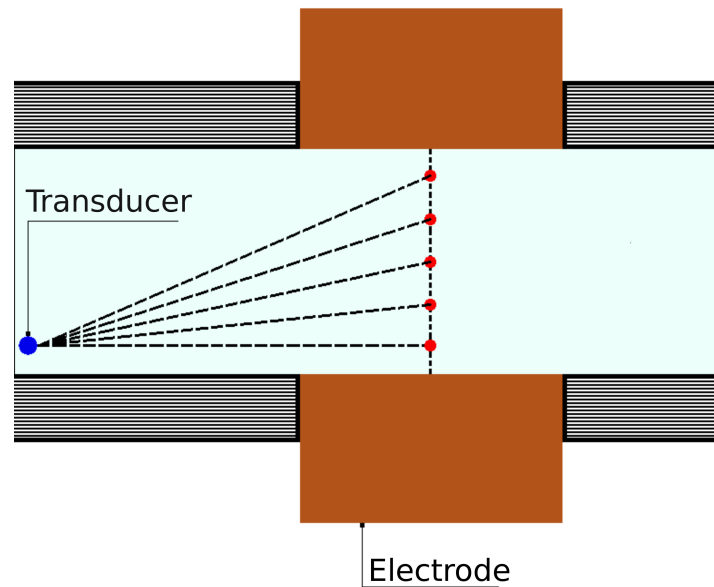
Fig. 3.3: Sketch of the angle variation of the UDV transducer to perform axial velocity measurements.

## 3.2.2 Electrical characterization

Due to the electrical output conditions of the generator that involves low voltages and high currents, it is necessary to use non-conventional measurement methods, since it is practically impossible to get reliable measurements with ordinary devices. To overcome this complication, the current is inferred from a Hall effect sensor, where its output voltage is related to the induced magnetic field in a conductor (variable electric load) through which the electric current of the MHD generator passes. With the aim of varying the load factor of the generator, three different electric loads were used. As we mentioned before, the load factor is a relevant parameter, which relates the internal resistance of the generator ($R_i$) and the total resistance of the external load $R_c$. The internal resistance of generator measured experimentally is equal to $R_i \approx 1.0 \times 10^{-5}$ ohm. The total load resistance ($R_c$) is the sum of the resistence of all the components of the external load, that include a fixed electric load plus a variable load (see figure 2.5). For the majority of the explored cases the fixed electric load is composed of two copper electrodes in contact with the liquid metal (lateral walls), two copper circular bars (3/8 in diameter and 10 cm long) and two rectangular copper bars (20 cm long and a rectangular cross section of 2 in $\times$ 1/4 in). Adding the resistance of each component the fixed resistance has a value of $R_f = 9.1 \times 10^{-5}$ ohm. The variable electric

resistance consisted of three metallic bars of different materials with a rectangular cross section and 25 cm long. Table 3.2 shows the material of each bar, its electric resistance, the total load resistance and the corresponding value of the load factor. Resistances were measured using the four-wire method [62]. In order to improve the operation of the MHD generator, in addition to conditions shown in Table 3.2, a special configuration of fixed electrical resistance was used, which is based on reducing the resistance of the circular copper bars, putting in parallel other resistances. This special configuration allowed to obtain a fixed resistance value of $R_f = 6.7 \times 10^{-5}$ ohm and a total resistance of $R_c = 8.6 \times 10^{-5}$ ohm with a load factor $K = 0.88$.

| Material | Variable resistance | Toltal resistance | $K = 1/(1 + R_i/R_c)$ |
|---|---|---|---|
| Copper | $1.9 \times 10^{-5}\Omega$ | $1.1 \times 10^{-4}\Omega$ | 0.916 |
| Aluminum | $2.51 \times 10^{-5}\Omega$ | $1.16 \times 10^{-4}\Omega$ | 0.920 |
| Steel | $36.36 \times 10^{-5}\Omega$ | $4.6 \times 10^{-4}\Omega$ | 0.978 |

Table 3.2: Properties of the different variable electric load.

The Hall effect sensor Allegro A1324 was used to estimate the total current that passes through the external electrical load, with a sensitivity of 5 $mV/G$. Since the response of the sensor depends on the magnetic field induced in the metal bar and, in turn, the magnetic field induced is a function of the characteristics of the bar, such as geometry, it was necessary to perform the calibration of the metal bars used to carry out the characterization of the MHD generator. The calibration was done by applying electric currents provided by a power supply to each of the variable external loads. Each of the applied currents corresponds to a voltage value of the sensor output, which behaves linearly with respect to the current. Figures 3.4 and 3.5 show the calibration for the aluminum and the steel bar used as variable loads, respectively, where the slope change between figures is due to the polarization of the injected current used to perform the characterization.
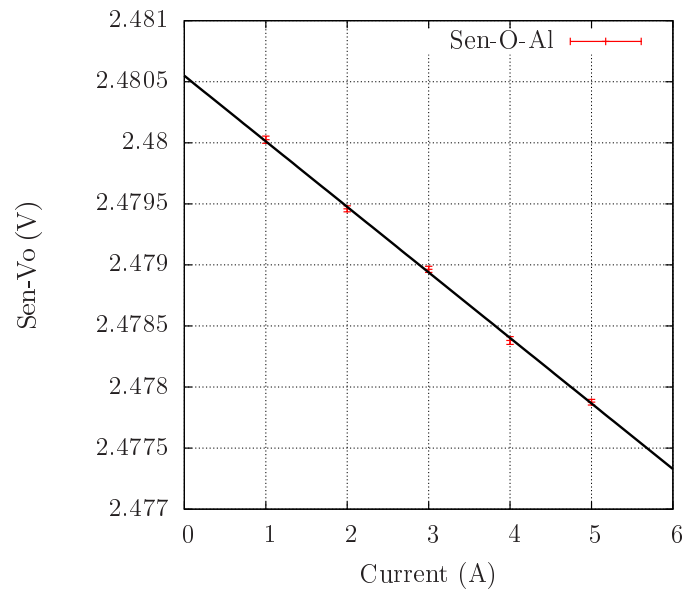
Fig. 3.4: Calibration of the aluminum bar
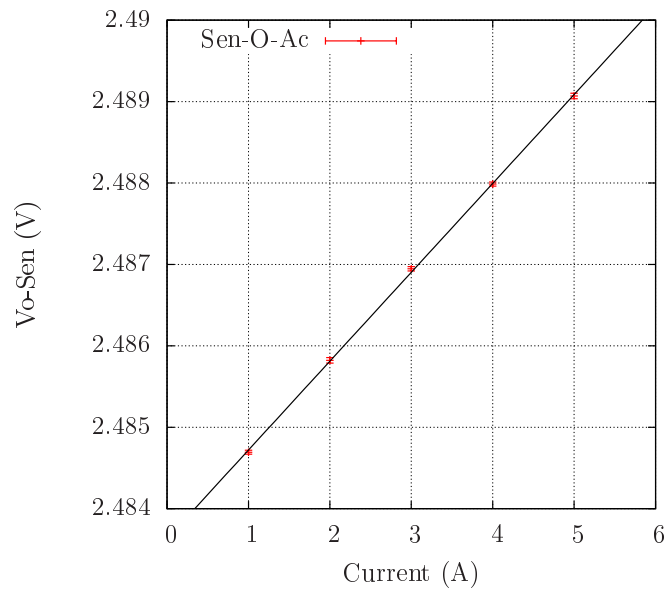


Fig. 3.5: Calibration of the steel bar

# Chapter 4

# Experimental results

This chapter presents the experimental results obtained from the laboratory prototype of the alternate LMMHD generator. The results comprise the analysis of the flow dynamics of the liquid metal in the oscillation duct as well as the electrical characterization of the MHD generator. The flow analysis include the measurements of the axial velocity of the liquid metal performed with the Ultrasonic Doppler Velocimetry under different conditions. For the electrical characterization, output currents and voltages obtained for different electric loads and oscillation frequencies are shown. In addition, the behavior of both the electrical power output and the isotropic electrical efficiency are presented as functions of the oscillation frequency and the load factor.

## 4.1 Flow dynamics in the oscillation duct

The liquid metal impelled by the piston in the oscillation duct describes essentially an oscillatory motion with a zero mean that comprises regions exterior to the applied magnetic field, where the flow behaves hydrodynamically, and a region affected by the magnetic field where MHD flow effects are important. Owing to the prescribed experimental conditions, that is, the ranges of oscillation frequencies and amplitudes, non-linear effects are negligible and therefore, the explored flow is in laminar regime (see Section 3.1). Nevertheless, small non-linear effects that may lead to steady streaming flows exist in the edges of the magnets where the magnetic field is strongly non-uniform, as it was analyzed theoretically in chapter 1. Although oscillatory liquid metal MHD flows in ducts have been studied in the past analytically and numerically, it appears that no experimental results have been reported in the literature for this kind of flows.

Since the motion of the liquid metal in the oscillation duct is mainly unidirectional, only the velocity component parallel to the symmetry axis of the duct was measured using the Ultrasound Doppler Velocimetry technique. Figures 4.1, 4.2 and 4.3 show examples of

the axial velocity maps of the liquid metal near the wall with a direction normal to the main flow as a function of the axial distance (penetration depth) and time, for the cases $R_\omega$ =14.2, 29.9 and 62.1, respectively, while the Hartmann number ($Ha$ = 24) and the oscillation amplitude (9.2 cm) remained fixed. The axial distance equal to zero corresponds to the location of the transducer while different colors represent the magnitude of the axial velocity. The red color (positive direction) indicates that the flow moves away from the transducer and the blue color (negative direction) indicates that the flow approaches the transducer. The vertical alternating colored regions show that the axial velocity behaves in a periodic way. The black horizontal lines represent the location of the edges of the magnets, where the electromagnetic effects are more intense. Observe that as the oscillation Reynolds number (i.e. the oscillation frequency) increases, the vertical alternating colored regions become narrower and more clearly defined. Figure 4.4 shows the axial velocity componet as a function of time at a distance of 15 mm from the side wall ($z$ = 15 mm) and at the axial distance $x$ = 209 mm (which corresponds to the center of the magnets), for $Ha$ = 24, amplitude of 9.2 cm and different oscillation Reynolds numbers (i.e. oscillating frequencies); it can be observed that the magnitude of the axial velocity increases as $R_\omega$ increases. Notice that the variation of $R_\omega$ involves also a phase shft. Figure 4.5 shows a comparison of the axial velocity profiles at the center of the oscillation duct ($z$ = 30 mm) along the symmetry axis in the hydrodynamic region ($x$ = 340 mm) and at the mid point of the permanent magnets ($x$ = 209 mm) as a function of time for $R_\omega$ = 29.9, $Ha$ = 24 and amplitude of 9.2 cm. Since the Lorentz force brakes the flow within the magnetic field, the velocity within this region is smaller than the velocity outside the magnetic field (hydrodynamic region). In the present case the reduction is about 11.3 %. In figure 4.6 the axial velocity component as a function of the axial distance at a distance of 15 mm from the side wall of the oscillation duct ($z$ = 15 mm) and at different times during half cycle is shown. As usual, the position $x$ = 0 corresponds to the position of the transducer while the vertical red lines represent the zone affected by the magnetic field. Note that the higher values (either positive or negative) of the axial velocity are found upstream of the magnetic field region, that is, when the liquid metal is entering this region.
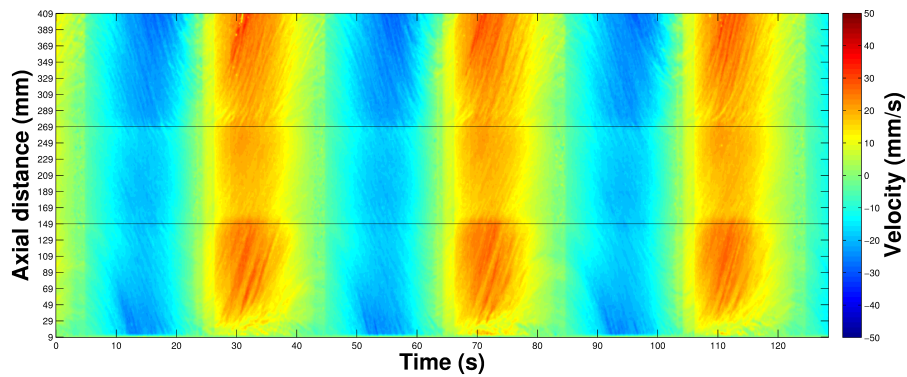
Fig. 4.1: Axial velocity map obtained with UDV as a function of the axial distance and time for an oscillation amplitude of 9.2 cm with $Ha = 24$ and $R_\omega = 14.2$.
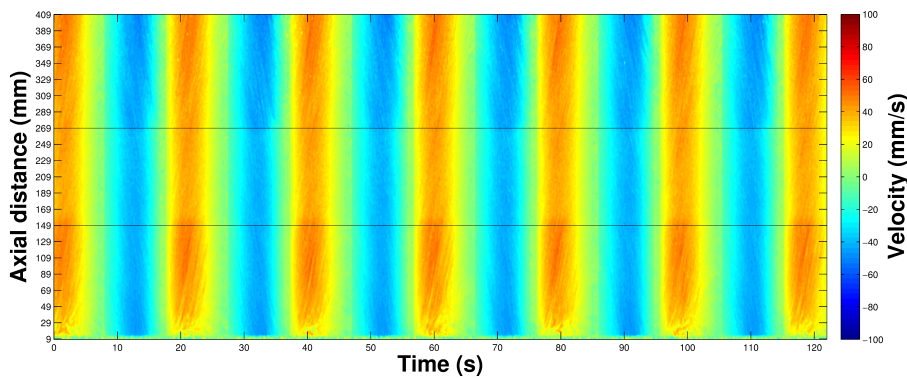


Fig. 4.2: Axial velocity map obtained with UDV as a function of the axial distance and time for an oscillation amplitude of 9.2 cm with $Ha = 24$ and $R_\omega = 29.9$.
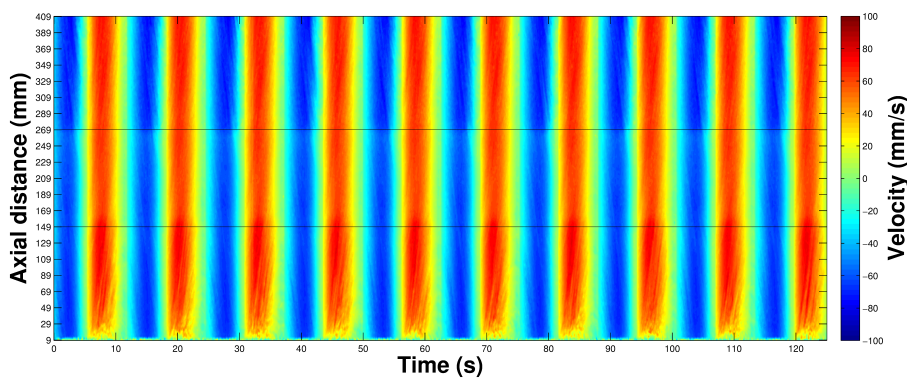


Fig. 4.3: Axial velocity map obtained with UDV as a function of the axial distance and time for an oscillation amplitude of 9.2 cm with $Ha = 24$ and $R_\omega = 62.1$.
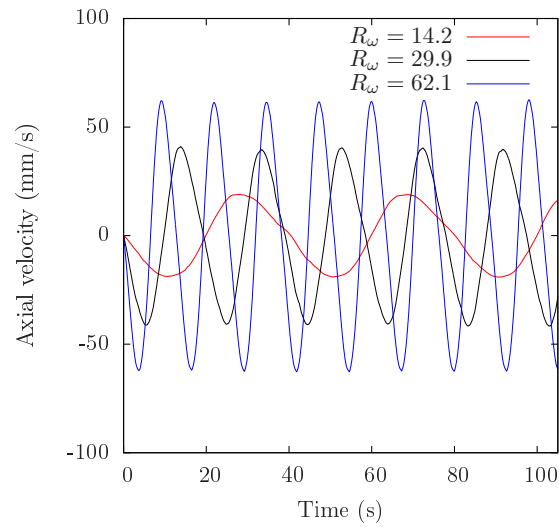
Fig. 4.4: Axial velocity as a function of time at the fixed axial distance $x = 209$ mm (center of the magnets ) and at the fixed transversal position $z = 15$ mm (15 mm from the lateral wall) for different oscillation Reynolds numbers (i.e. oscillation frequencies) with an oscillation amplitude of 9.2 cm and $Ha = 24$.
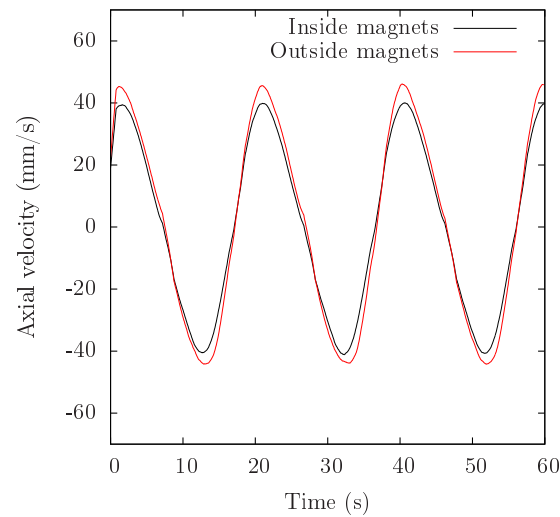


Fig. 4.5: Axial velocity component as a function of time for $R_\omega = 29.9$, $Ha = 24$, and an oscillation amplitude of 9.2 cm at the center of the oscillation duct ($z = 30$ mm) and at two different axial locations. The black line corresponds to an axial distance $x = 209$ mm (at the mid point of the magnetic field region) and the red line corresponds to an axial distance $x = 340$ mm (far from the magnetic field region).
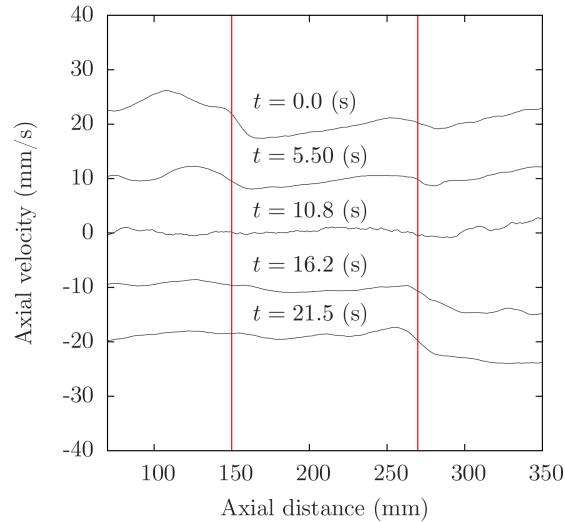
Fig. 4.6: Axial velocity component as a function of the axial distance at the fixed transversal position $z$ = 15 mm (15 mm from the lateral wall) for different times during half cycle with $R_\omega$ = 14.2 and $Ha$ = 24.

In order to estimate the volumetric flow rate in the oscillation duct, measurements were made by varying the angle of the transducer acoustic axis with respect to the direction of the main flow. In this way, it was possible to estimate the average axial velocity of the liquid metal in the oscillation duct and thereby infer the volumetric flow. Figure 4.7 shows the axial velocity map as a function of the axial distance and time for different measurement angles, where it can be observed the change of the axial velocity distribution as the measurement angle changes.

From the measurements at different angles it is possible to obtain axial velocity profiles at a given axial distance for different positions in the transverse $z$-coordinate. Figure 4.8 shows axial velocity profiles as a function of the $z$-coordinate with $R_\omega$ = 14.2, $Ha$ = 24, oscillation amplitude 9.2 mm and a fixed axial distance of 209 mm (center of the magnets) for different times during approximately one cycle. Figures 4.8(a) and 4.8(b) show, respectively, the first and second half cycles. Note that the laterals walls of the oscillation duct are located at $z$ = 0 and $z$ = 60 mm. At the axial distance of 209 mm (center of the magnets) the measurements closest to the wall that allowed the used technique corresponded to positions $z$ = 10 mm and $z$ = 50 mm. The almost overlaped pair of values shown in the velocity profiles at different times correspond to measurements from each of the side walls with the same experimental conditions. This gives confidence in the reproducibility of profiles independently of the side wall from which measurements are taken. The inversion of the axial velocity from positive to negative values as the oscillation cycle advances is also observed. Since the side walls are parallel to the applied magnetic field, the boundary lay-

ers attached to these walls should be a combination of Stokes layer and Shercliff layer [42]. Unfortunately the precise thickness of this layer has not been determined yet. Therefore, with the aim of giving an approximate estimate of the involved boundary layer we consider it as if it were a Stokes layer. The thickness of the Stokes boundary layer can be estimated as $LR_\omega^{-1/2}$, where $L$ correspond to the distance between the copper electrodes. Then, taking $L = 60$ mm and $R_\omega = 14.2$ the Stokes boundary layer for the particular experimental conditions shown in figure 4.8 is 15.93 mm, which means that the two measured points closest to the side walls of the oscillation duct are inside of the Stokes layer. Evidently, as the $R_\omega$ increases the thickness of the Stokes layer becomes smaller and for an $R_\omega = 300$ the thickness of the Stokes layer is approximately 3.4 mm.

(a)



(b)



(c)
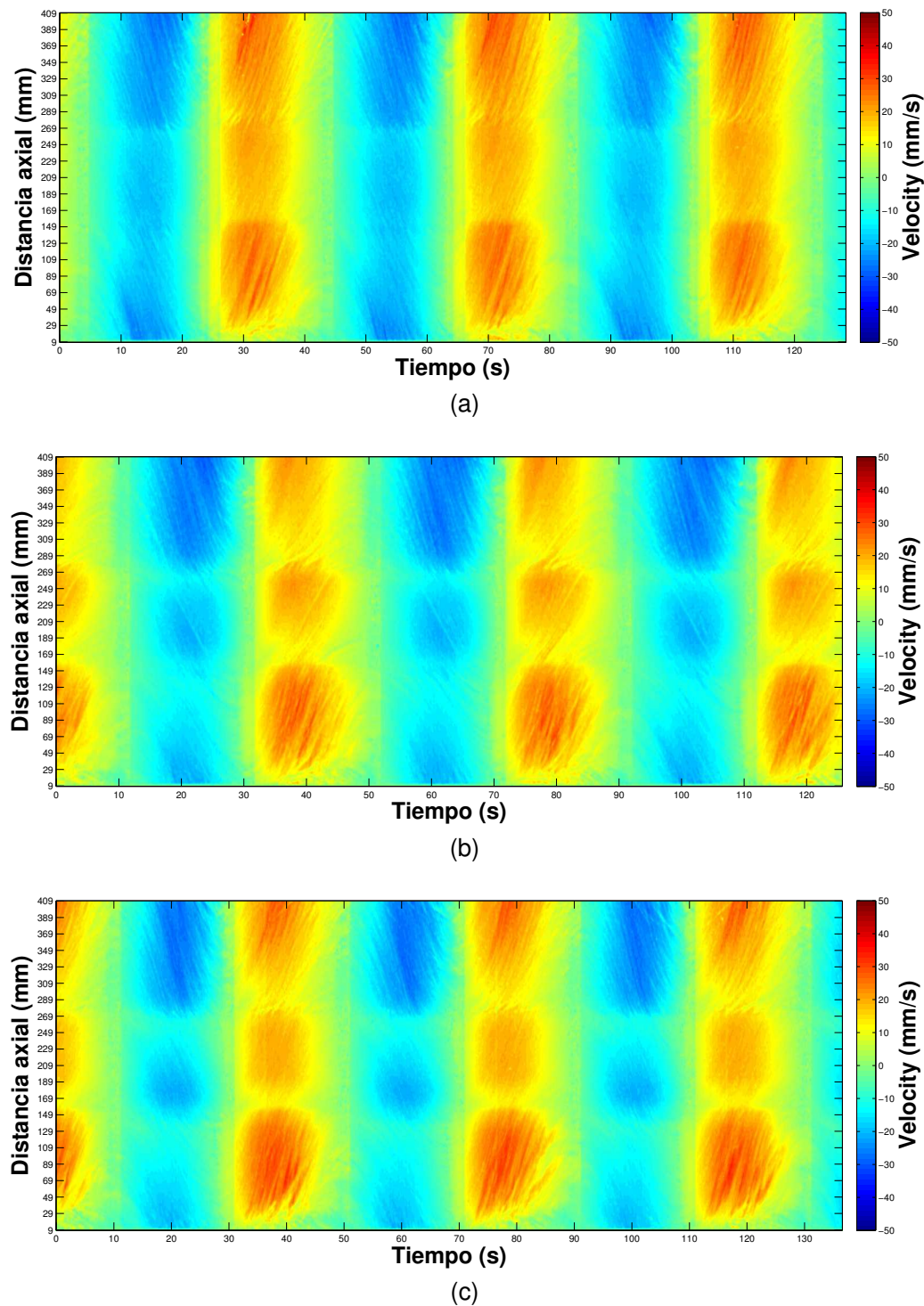
Fig. 4.7: Axial velocity map as a function of the axial distance and time with $R_\omega = 14.2$, $Ha = 24$, oscillation amplitude of 9.2 cm and for different measurement angles. (a): $\theta = 0°$. (b): $\theta = 2°$. (c): $\theta = 4°$.

(a)



(b)
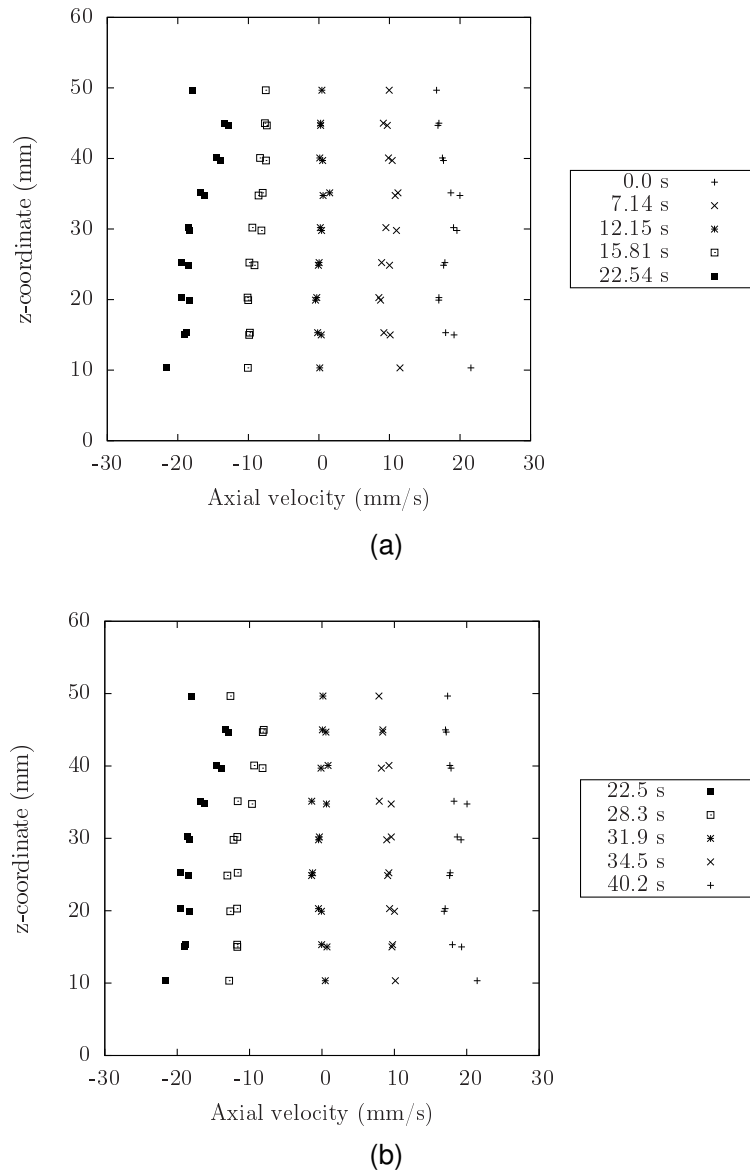
Fig. 4.8: Axial velocity profiles as a function of the $z$-coordinate at different times with $R_\omega = 14.2$, $Ha = 24$ and oscillation amplitude of 9.2 cm. (a) and (b) show the first and second half cycles, respectively.

From the velocity profiles at different $z$-positions, it is possible to calculate the averaged velocity in the transverse section of the oscillation duct as a function of time, which has a periodic bahavior, as shown in figure 4.9 for different vales of $R_\omega$. Again, note that the change in $R_\omega$ introduces a phase shift. Figure 4.10 shows the root mean square (RMS) of the average axial velocity in the oscillation duct duct for different $R_\omega$ values and two oscillation

amplitude values. From Figures 4.9 and 4.10, it can be observed that both the amplitude as well as the RMS value of the axial velocity component increase as $R_\omega$ increases.
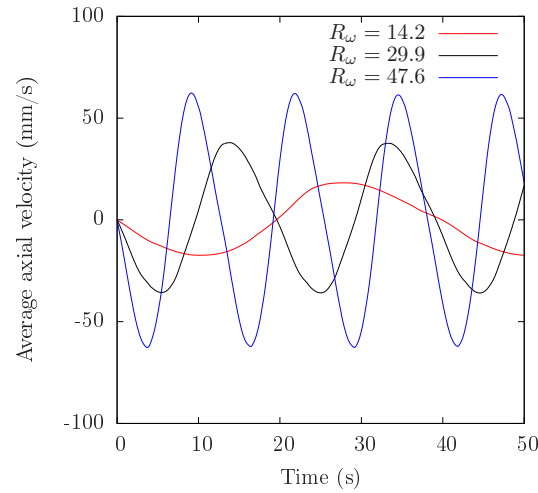


Fig. 4.9: Average axial velocity at the transversal mid plane of the magnets as a function of time for different $R_\omega$ values and $Ha = 24$ and oscillation amplitude of 9.2 cm.
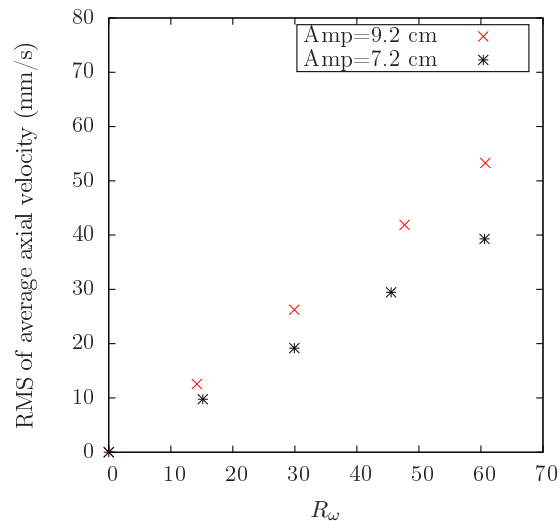


Fig. 4.10: RMS value of the average axial velocity at the transversal mid plane of the magnets as a function of $R_\omega$ for different amplitudes and $Ha = 24$.

## 4.2   Electric experimental results

Evidently, the electrical response of the LMMHD generator is linked to the driving source that powers the device. Therefore, as a result of the reciprocating linear movement of the piston transmitted to the liquid metal, the output electrical signals, that is, induced current and voltage, have an alternating behavior. As mentioned in chapter 3, the electrical behavior of the generator depends on several physical and geometrical parameters, namely, the size (volume) of the generator, the oscillation frequency and amplitude of the liquid metal, the internal and external electrical resistance of the generator, the strength and distribution of the applied magnetic field and the physical properties of the liquid metal. Once the design of the prototype was defined, some parameters remained fixed such as the size and internal resistance of the generator, the applied magnetic field and the properties of the liquid metal. This means that the Hartmann number takes the fixed value $Ha = 24$. The electrical response of the generator was then explored by varying the oscillation frequency and amplitude of the liquid metal as well as the external electric resistance (load factor). The variation of these parameters are in turn restricted by the limitations of the experimental prototype. Figures 4.11 and 4.12, respectively, show the induced current and voltage as a function of time for different values of the oscillation Reynolds number. The oscillation amplitude was 9.2 cm while the load factor and Hartmann number correspond to $K = 0.88$ and $Ha = 24$, respectively. First, notice that induced currents, inferred from the output of the Hall effect sensor, are of the order of magnitude of Ampéres (A) while induced voltages remain in the order of millivolts (mV). It can also be observed that the amplitude of induced currents and voltages increases as the oscillation frequency (i.e. $R_\omega$) increases, while a phase shift also appears with the variation of this parameter. In both figures the signal corresponding to the smaller frequency ($R_\omega$=94.3) shows a slight deformation with respect to a pure sinusoidal signal what could be due to perturbations introduced by the impeller system. A useful way to represent oscillatory values of the electrical output variables is through the root mean square (RMS), defined as the square root of the arithmetic mean of the squares of the instant values of the variable during one cycle. Figures 4.13 and 4.14 show, respectively, the RMS value of induced current and voltage as a function of the oscillation Reynolds number for different load factors with $Ha = 24$ and an oscillation amplitude of 9.2 cm. It can be observed that current and voltage increase almost linearly with respect to the oscillation frequency. For the induced current the fastest growth is found for the smallest load factor explored ($K = 0.88$) while the slowest corresponds to the higher load factor ($K = 0.97$). As expected, this behavior is inverted for the induced voltage although differences in growth rate for different load factors are rather small. For the lowest load factor explored ($K = 0.88$), the highest RMS values for the induced current and voltage are 7.4 A and 0.72 mV, respectively.

The performance of the alternate LMMHD generator is characterized to a large extent by the output electric power which can be obtained from the product of the induced current

and the induced voltage. Figure 4.13 shows the output electric power as a function of time for different oscillation Reynolds numbers with $K = 0.88$, $Ha = 24$ and oscillation amplitude of 9.2 cm. It can be observed that the amplitude of the output power increases as $R_\omega$ increases and reaches around 10 mW for the highest $R_\omega$ value shown ($R_\omega = 270.7$). Note also that the peak amplitude presents slight variations. The RMS value of the output electric power is shown in figure 4.16 as a function of the oscillation Reynolds number for different load factors with $Ha = 24$ and oscillation amplitude of 9.2 cm. A quadratic variation with the oscillation Reynolds number if found, the fastest growth corresponding to the largest $R_\omega$ value ($R_\omega = 270.7$).
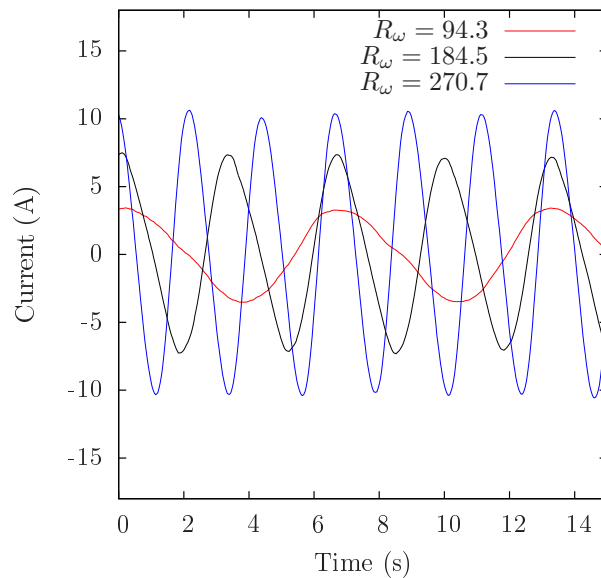
Fig. 4.11: Induced output current as a function of time for different oscillation Reynolds numbers with $K = 0.88$, $Ha = 24$ and oscillation amplitude of 9.2 cm.
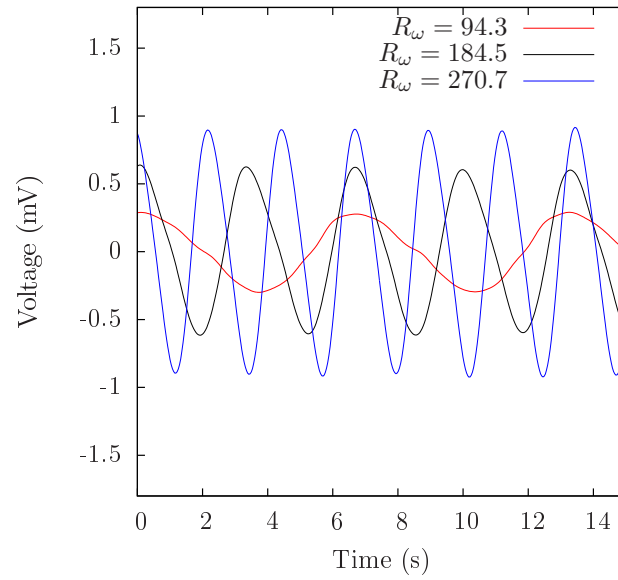
Fig. 4.12: Induced output voltage as a function of time for different oscillation Reynolds number with $K = 0.88$, $Ha = 24$ and oscillation amplitude of 9.2 cm.
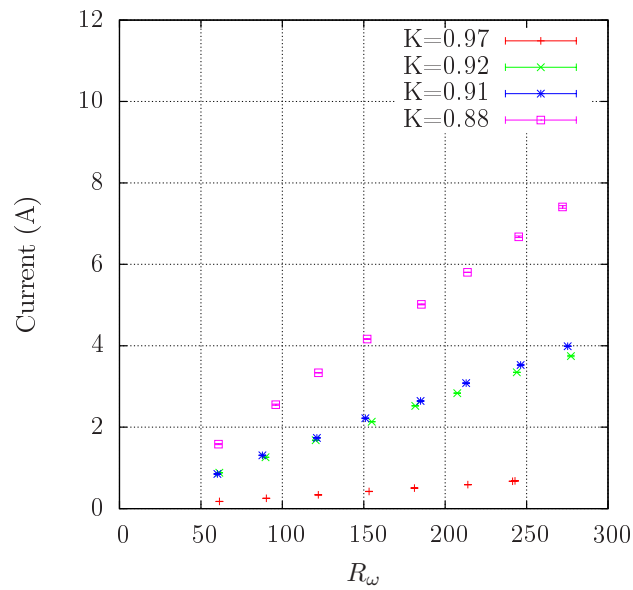


Fig. 4.13: RMS values of the induced output current as a function of the oscillatory Reynolds number for different load factors with $Ha = 24$ and oscillation amplitude of 9.2 cm.
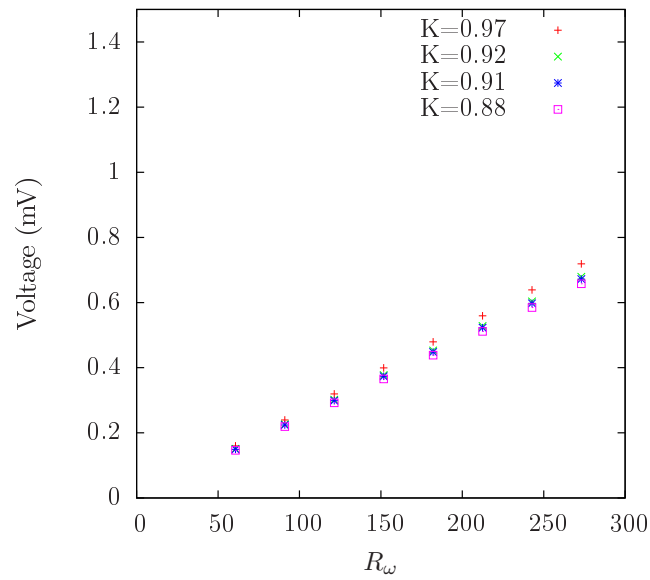
Fig. 4.14: RMS values of the induced output voltage as a function of the oscillation Reynolds number for different load factors with $Ha = 24$ and oscillation amplitude of 9.2 cm.
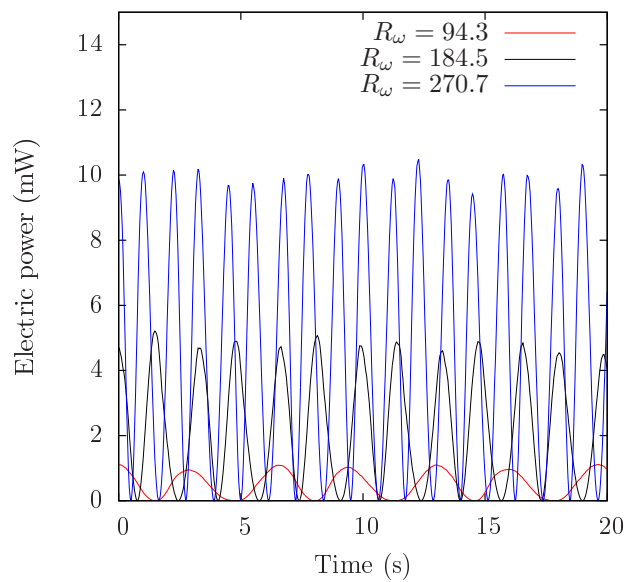


Fig. 4.15: Output electric power as a function of time for different oscillation Reynolds number with $K = 0.88$, $Ha = 24$ and oscillation amplitude of 9.2 cm .
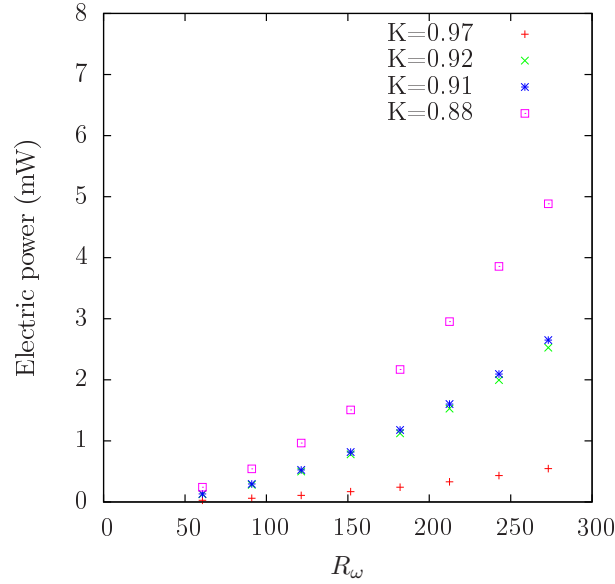
Fig. 4.16: RMS values of the output electric power as a function of the oscillation Reynolds number for different load factors with $Ha = 24$ and oscillation amplitude of 9.2 cm.

The electrical characterization of the alternate LMMHD generator requires the calculation of the efficiency. In section 1.5, the electrical isotropic efficiency was defined as the ratio of the output electric power, $P_e$, and the "push power" or mechanical power, $P_f$, required to overcome the Lorentz force exterted on the fluid due to its motion within the magnetic field, integrated over the total volume of the generator and over a whole time period or an integer number of periods, that is

$$\eta_e = \frac{P_e}{P_f} = \frac{\int dt \int_V \mathbf{J} \cdot \mathbf{E} dV}{\int dt \int_V (\mathbf{J} \times \mathbf{B}) \cdot \mathbf{u} dV}. \tag{4.1}$$

Note that the integral in the numerator is the product of the current and voltage. As it was mentioned before, $\eta_e$ gives the fraction of the mechanical work done by the liquid metal in overcoming the Lorentz force that is converted into useful electric power. Since it was not possible to estimate the push power directly from the experiments, an analytical estimation was used with the experimental parameters. Since the available experimental results involve integral quantities such as the RMS values of the flow velocity ($U_{RMS}$), current ($I_{RMS}$) and voltage ($\Phi_{RMS}$), the RMS value of the analytical estimation was used. The electrical efficiency can be estimated in the following way.

$$\eta_e = \frac{P_{e\_RMS}}{P_{f\_RMS}} = \frac{I_{RMS} V_{RMS}}{\left[\int_V (\mathbf{J} \times \mathbf{B}) \cdot \mathbf{u} dV\right]_{RMS}}. \tag{4.2}$$

Figure 4.17 shows the electrical efficiency estimated using the expression (4.2) as a function of the oscillation Reynolds number for different values of the load factor with $Ha = 24$ and oscillation amplitude of 9.2 cm. It can be observed that the highest efficiency ($\eta_e = 0.2$) is obtained for the smallest load factor explores ($K = 0.88$) while the lowest efficiency ($\eta_e = 0.085$) corresponds to the largest load factor ($K = 0.97$). For each load factor the efficiency remains practically constant in the whole range of $R_\omega$, although a very slight increase is found with this parameter. Figure 4.18 shows the electrical efficiency estimated from (4.2) as a function of the load factor for $R_\omega = 60$, $Ha = 24$ and oscillation amplitude 9.2 cm. The symbols represent the experimental data while the black line corresponds to a fit. Only one value of $R_\omega$ is presented due to the very small change of the efficiency with respect to this parameter, therefore, this curve is essentially the same for any other $R_\omega$ value. It can be observed that the maximum efficiency is obtained for $K = 0.88$, in agreement with Figure 4.17. Recall that maximum efficiency does not mean maximun power output which according to the analytical model (see section 1.5), is obtained when $K = 0.5$.

When compared with the values of output electric power and electrical efficiency predicted by the analytical model (see section 1.5), the values obtained experimentally are approximately, 50 % lower. This reflects in part the idealizations introduced in the analytical model which considers the flow in the MHD generator as two-dimensional and under a completely uniform magnetic field. The existence of lateral walls (electrodes), not considered explicitlly in the model, introduces additional friction losses as well as contact resistance effects between the copper walls and the liquid metal that affect the performance of the generator. In turn, the non-homogeneity of the magnetic field and the finite size of the magnets that produce it, originate modifications in the flow field as well as in the electrical response of the device. In particular, the abrupt variation of the magnetic field at the edges of the permanent magnets and the finite size of the electrodes give rise to end-effects which divert the induced electric currents out of the electrode area forming short-circuited loops outside the generation zone [63].

From equations (1.84), (1.86) and (1.94), it is found that the output electric power increases linearly with the electric conductivity of the fluid, the squared average flow velocity and the squared strength of the magnetic field. Since the variation in electric conductivity among different liquid metals (the best available working fluids) with adequate melting temperatures is rather small, an increase in the output power should rely mostly in the increase of both the flow velocity and the strenght of the applied magnetic field. The average flow velocity of the oscillating liquid metal in the MHD generator could be increased by a proper design and coupling with a WEC, while to increase the strength of the magnetic field it is required the use of improved magnetic materials and proper magnetic field configurations. Since MHD electric generation is a volumetric effect, the increase in size of the MHD generator and/or the coupling of several MHD generators could be an alternative to the increment of the output electric power.
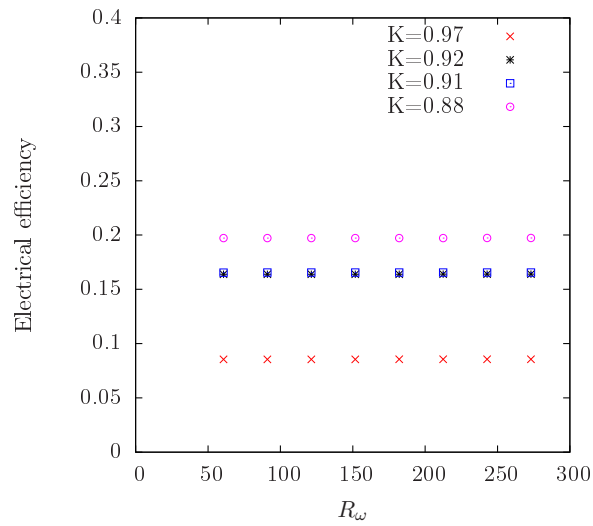
Fig. 4.17: Isotropic efficiency of the LMMHD generator as a function of the oscillatory Reynolds number for different load factor with $Ha = 24$ and a oscillation amplitude of 9.2 cm.
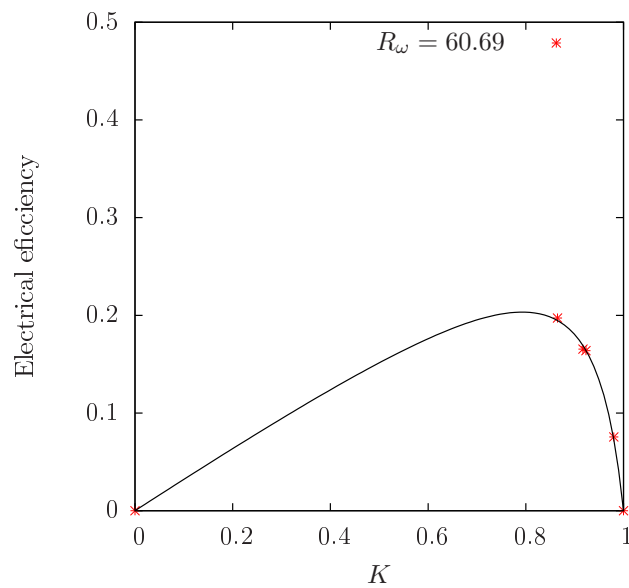


Fig. 4.18: Isotropic efficiency of the LMMHD generator as a function of the load factor, $K$, for $R_\omega = 60.69$ with $Ha = 24$ and oscillation amplitude of 9.2 cm.

## 4.3 Future experiments: coupling the LMMHD generator to a WEC

The main goal of the present work was to design, built and characterize experimentally an alternate LMMHD generator at laboratory scale. As it was presented in the previous sections, it was possible to analyze both the flow behavoir in the oscillation duct and the electrical response of the generator under the conditions imposed by the impeller system. Since this system reproduces an approximately regular oscillatory motion, the operation conditions of the prototype are still different from those that would take place if the generator were coulpled to a WEC. Therefore, the next step within the frame of CEMIE-O is to develop and test an experimental device operating in more realistic conditions. This involves the design, construction and characterization of an alternate LMMHD generator coupled to a WEC that can be tested in the wave channel facility of the Engineering Institute of UNAM. The new conceptual design presented here also includes changes aimed at improving the electrical performance of the generator. The wave channel is a rectangular cross section open channel with 80 cm at the base, 120 cm high and 39 m long. The laterals walls and the bottom of the wave channel are made with 12 mm thick tempered glass. Above the wave channel, two steel rails anchored to the laboratory roof and aligned with the channel, allow to support and fix the experimental devices to be characterized. The new design comprises an alternate LMMHD generator placed vertically, a wave energy converter coupled to the generator, the fastening system and different measurement systems. Figure (4.19) shows a sketch of the new experimental device to be installed in the wave channel. The main purpose of the new design is to replace the impeller system used in the laboratory prototype by a WEC able to transmit the wave motion of the water into an oscillatory motion of the liquid metal. This can be achieved by a buoy whose up and down motion caused by the water waves is communicated through a diaphragm to the liquid metal inside the vertical oscillation duct.

The new design of the LMMHD generator was adapted to the dimensions of the wave channel where it will be tested. The oscillation duct with a rectangular cross section is made of two acrilyc plates joined by screws and sealed by a linear seal. In the central zone of the duct (generation zone) two permanent magnets are placed externally in two of the duct walls and two copper electrodes are located at the side walls of the duct. The permanent magnets are rectangular prism with dimensions of 80 mm $\times$ 80 mm $\times$ 7 mm and magnetized in the direction normal to the larger face. The electrodes are copper plates of 8 cm width and 5 mm thick. The region that composes the MHD transducer has a rectangular cross section of 7 cm $\times$ 0.5 cm with a length of 8 cm. At one end of the duct a rolling diaphragm is used to seal the device and avoid direct contact of the liquid metal with other elements. The diaphragm is made of elastomeric materials, which offer the flexibility to deform allowing to pump the liqud metal. The other end of the duct

has an open area, which allows the liquid metal to oscillate as an oscillating colum. The most important differences between the new design of the LMMHD generator and the one presented in the chapter 2 are the dimensions of the generator, since the volume of liquid metal in the new version corresponds approximately to one tenth of the previous design. Another inmportant change is that, with the aim of increasing the mean velocity of the liquid metal and reducing the end effects produced by the abrupt change of the magnetic field at the edges of the permanent magnets, a reduction of the area of the rectangular cross section in the generation zone (i.e. where the magnets and the copper electrodes are located) was introduced in the oscillation duct. Figure 4.20 shows two section views of the new LMMHD generator design, where changes in the geometry of the oscillation duct are displayed. The fastening system is responsible for fixing and loading almost the entire weight of the experimental device, giving freedom of movement to the liquid metal. The oscillatory motion of the water generated in the channel is transferred to the liquid metal through a WEC consisting in a buoy attached to the lower part of the oscillation duct so that the wave motion is converted into a linear oscillatory movement in the vertical direction. The motion of the buoy is limited to the vertical direction by means of linear bearings, which serve as a guide to the shafts attached to the lateral ends of the buoy. The buoy is designed so that the buoyancy force is approximately twice the weight of the liquid metal. In the central area of the buoy the shaft responsible for transferring the linear oscillatory movement in the vertical direction to the diaphragm located at the lower end of the oscillation duct is located. The electrical characterization of the device will be carried out by measuring the magnetic field induced in the external load by means of a Hall effect sensor. Figure 4.21 shows a cross-section view of the oscillation duct, where the arrangement of the total electric load connected to the LMMHD generator is presented. The total electric load consist in two C-shape copper electrodes (lateral walls of the duct) and a metal bar which closes the circuit. Theoretically, the internal resistance of the LMMHD generator is approximately $50 \times 10^{-6}$ ohms. The external load consist of a metal sheet of 5 mm thick which connects the electrodes. To be able to characterize the performace of the LMMHD generator by varying the load factor, different metals can be used as well as different thicknesses of the metal sheet. The electrical resistance of the external circuit will be characterized by the four wire technique. Theoretically, an estimate of the electrical resistance of the total external circuit can be made for different electrical loads. The fixed electrical resistance corresponding to the two C-shape electrodes is approximately $17 \times 10^{-6}$ Ohms. Table 4.1 shows the different configurations of the metal sheets proposed to perform the electrical characterization of the generator with different load factors. Notice that these calculations do not take into account the contact resistance between the materials. With the different configurations of the electrical load it is possible to characterize a wide range of load factors.
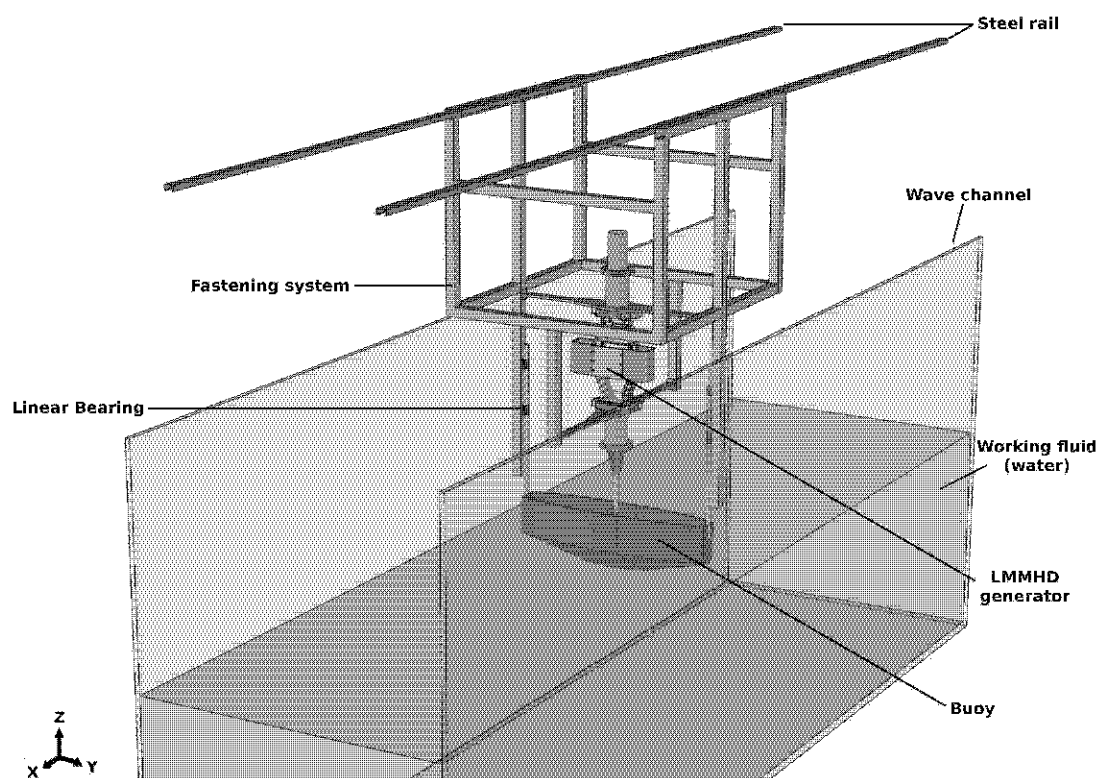
Fig. 4.19: Design of the LMMHD generator coupled to a wave channel.
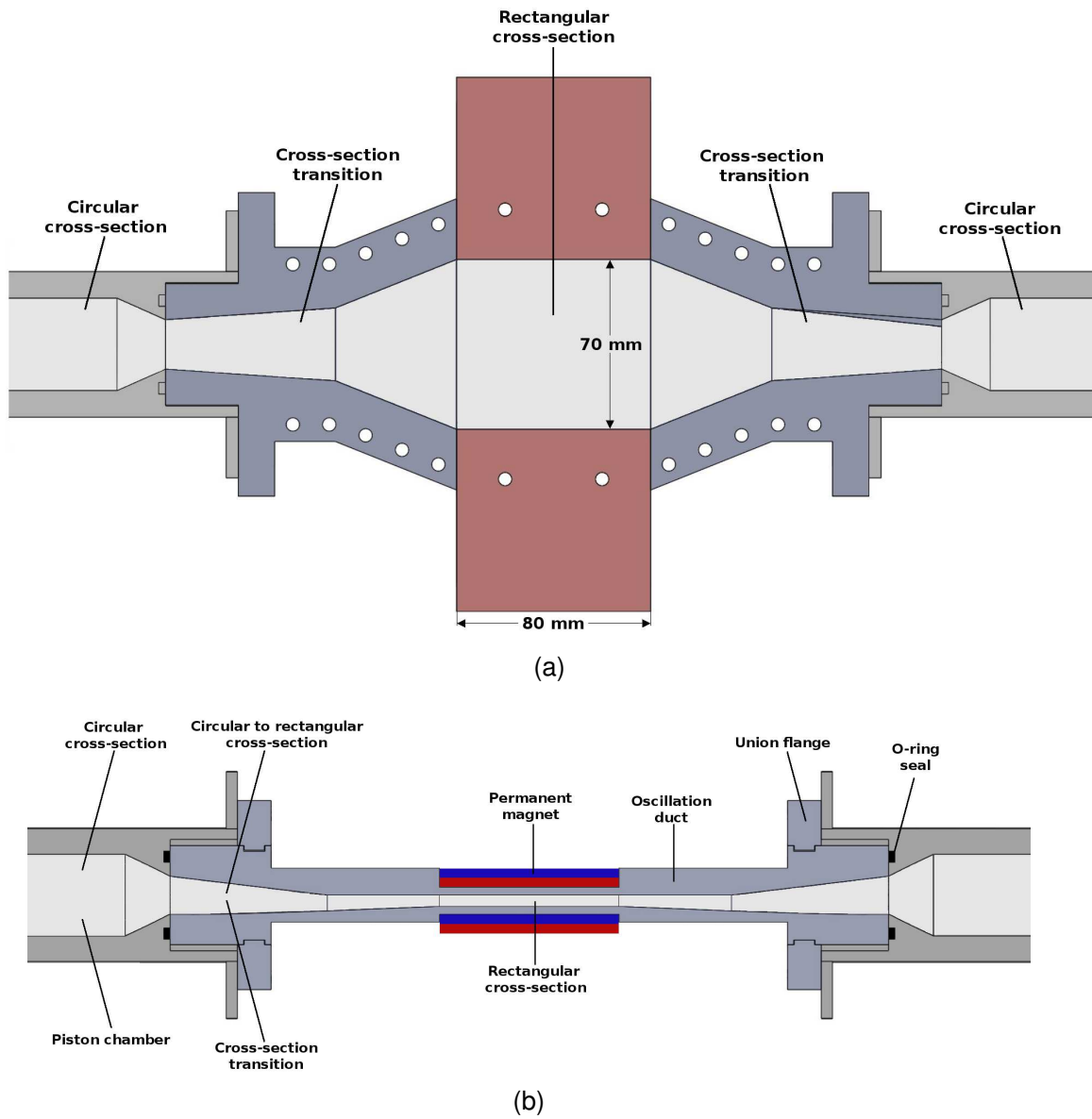
Fig. 4.20: Section views of the oscillation duct, where changes in the cross-section can be observed.
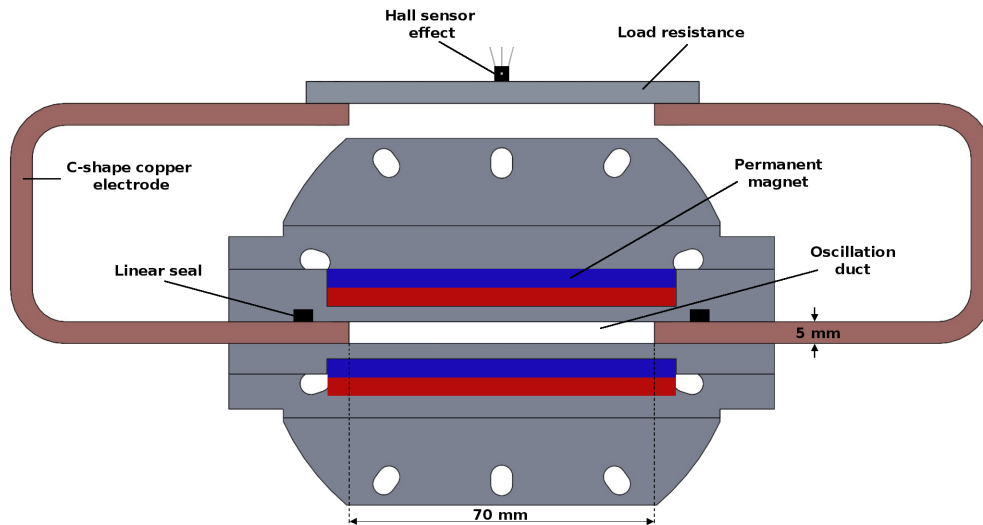
Fig. 4.21: Cross-section view of the LMMHD design.

| Material | dimensions | Electric resistance | Toltal electric resistance | K |
|---|---|---|---|---|
| steel | 90cm × 10cm × 0.5cm | 36 × $10^{-5}\Omega$ | 37.7×$10^{-5}\Omega$ | 0.88 |
| | 90cm × 20cm × 0.5cm | 18 × $10^{-5}\Omega$ | 19.7×$10^{-5}\Omega$ | 0.80 |
| | 90cm × 35cm × 0.5cm | 10 × $10^{-5}\Omega$ | 11.7×$10^{-5}\Omega$ | 0.70 |
| | 90cm × 60cm × 0.5cm | 6.0 × $10^{-5}\Omega$ | 7.7 × $10^{-5}\Omega$ | 0.60 |
| | 90cm × 80cm × 0.5cm | 4.5 × $10^{-5}\Omega$ | 6.2 × $10^{-5}\Omega$ | 0.55 |

Table 4.1: Properties of the different configuration of the external electric load.

# Chapter 5

# Conclusions

In the present work, a theoretical and experimental study of a liquid metal magnetohydro-dynamic (LMMHD) generator which has the potential of converting useful energy from marine waves into electricity was carried out. As direct power conversion systems, MHD generators present an alternative to linear generators where the main difference with these devices is the use of a fluid as conducting medium. MHD generators are also able to work at low frequencies, matching the low frequencies of ocean waves. The main motivation of the work was the understanding and modelling of the physical phenomena involved in the conversion process as well as the design, construction and experimental characterization of a prototype at laboratory scale of an alternate LMMHD generator.

After establishing the set of fundamental equations of magnetohydrodynamics, that comprise fluid dynamics and electromagnetic field equations, a two-dimensional analytical model of a laminar liquid metal duct flow driven by an oscillatory pressure gradient under the presence of a transverse magnetic field was analyzed. First, the attention was focused in the flow far from the edges of the generator where the magnetic field is uniform with the aim of exploring the phase lag produced by the Lorentz force between the velocity and the axial pressure gradient. The flow was analyzed by asymptotic techniques, obtaining solutions in the limits of low and high oscillation frequencies and for arbitrary Hartmann numbers. Solutions in the corresponding limits have terms in phase and out of phase with respect to the pressure gradient, where the importance of each term is affected by the magnitude of the applied magnetic field. The main results were conveniently synthesized graphically. In addition, the oscillatory flow of the liquid metal close to the edges of the magnets where the magnetic field is non-uniform was analyzed, paying a particular attention to the behavior of the oscillatory boundary layers (a combination of the Stokes and Hartmann layers) immersed in the spatially varying magnetic field. The solution was found using a perturbation method for high oscillation frequencies and assuming the small amplitude of oscillation approximation. It was found that non-linear effects give rise to a steady streaming vortices in the fringing magnetic field that are not expected to affect the

performance of the MHD generator. The analytical two-dimensional approach was also used to develop a theoretical model that describes the electrical performance of the generator, obtaining expressions for the total current, voltage, internal resistance, output power, flow power and isotropic efficiency. Although the analytical model incorporates strong simplifications, it offers a suitable description of the electrical behavior of the generator and a deeper insight of the underlying physical phenomena. In fact, it also served as a guide for the design of the experimental LMMHD generator.

The design of a prototype that could be tested experimentally in laboratory involved the requirement of having a system capable of emulating the oscillatory wave motion. This was solved by designing a device that allows to transform the rotary movement of an electric motor into a linear motion transferred to the liquid metal confined in the oscillation duct, where the MHD generator is located. Complementary equipment to carry out flow velocity and electrical measurements was also designed. The vast majority of the experimental prototype was manufactured at IER-UNAM, with the help of a computing numerical control (CNC) machine.

As the working fluid is a liquid metal, flow velocity measurements were done using the technique of Ultrasound Doppler Velocimetry. To the best of our knowledge, no reported experimental UDV data of oscillatory liquid metal duct flows exist in the specialized literature. By introducing the UDV transductor in the liquid metal at the extrem of the oscillation duct, the axial velocity component was measured along the duct axis for differents experimental conditions but always under laminar regime. The periodic behavior of the flow velocity was characterized by UDV velocity maps (that record the velocity magnitude as a function of time in the whole oscillation duct) as well as by velocity profiles as a function of time and the transversal coordinate. The braking effect caused by Lorentz forces when the liquid metal flows through the zone affected by the applied magnetic field was also detected. Moreover, it was found that for the explored range of governing parameters, the average axial velocity increases in a linear way with respect to the oscillatory Reynolds number.

A characteristic feature of LMMHD generators is to deliver low output voltages and high output currents so that typical measurement techniques do not work. To overcome this situation the electric current flowing in the external load was inferred from a Hall effect sensor while the load resistance was measured using a multimeter and applying the 4-wire technique. It was found that the RMS values of the current and voltage increase in a linear way as the oscillating Reynold number increases, while the output electric power, being the product of the current and voltage, increases quadratically as the oscillating Reynolds number increases. On the other hand, due to the smallness of the internal resistance of the generator, it was difficult to get load factor values close to K=0.5 where the highest output power is obtained (when the load resistance equals the internal resistance). Maximum RMS

values around 5 mW were reached for the lowest load factor explored ($K = 0.88$) and a high oscillation Reynolds number of 273. In turn, the highest isotropic efficiency estimated experimentally for $K = 0.88$ was about 20% in the whole range of $R_\omega$ explored. This is much lower than the efficiency predicted by the anlytical model due to several factors. In the first place, the analytical model is two-dimensional and assumes that the applied magnetic field is everywhere uniform which is far from reality. In fact, the non-homogeneity of the magnetic field and the finite length of the electrodes cause the end-effects of the generator, which are responsible for the biggest losses in the generator. This is an issue that has to be addressed in future designs with the aim at improving the efficiency of the generator.

In the last part of this work, a new experimental prototype able to operate in more realistic conditions was proposed. The objective of the new prototype is to test a LMMHD generator in a wave channel avoiding the impeller system used in the laboratory prototype. This implies to couple the generator to a wave energy converter, which is responsible for transferring the oscillating motion of the wave generated in the channel to the alternate LMMHD generator. The new design of the oscillation duct introduces modifications which will allow a better performance of the generator. In particular, a geometric modification of the oscillation duct which reduces the losses due to end-effects in the alternate LMMHD generator is considered.

Although there are still many challenges to overcome in order to apply the MHD technology in the field of ocean energy, the present work showed the feasibility of alternate LMMHD generators at laboratory scale, providing experimental results that will be of relevance for future designs. It deepened the understanging of the main physical phenomena involved in the energy conversion process and identified the relevant factors and parameters that affect the operation of the device. Although a more wide assessment is required, alternate LMMHD generators could be a suitable alternative to convert ocean wave energy into electricity at small-scale. For instance, the power supply to offshore scientific intstrumentation could be considered as an interesting application. If required, higher output power could be reached by coupling several generators. Among the remaining challenges is the development of a conversion system for transforming the electrical output of the alternate LMMHD generator, characterized by high currents and low voltages, to the standard requirements of conventional electric devices. It is expected that results obtained in the present work will set the basis for future research and development leading to a complete assessment of MHD technology for wave energy conversion.

# Appendix

The constants appearing in equation (1.63) are defined as follows:

$$\kappa_{t1} = \frac{\vartheta_{t1} + \vartheta_{t2}}{\vartheta_{t3}},$$

$$\kappa_{t2} = \frac{\vartheta_{t4} + \vartheta_{t5}}{\vartheta_{t6}},$$

$$\kappa_{t3} = \frac{U_0\,(\alpha' + i\beta')}{\gamma^2\,(\lambda^2 - 8i\alpha\beta - 4\alpha^2 + 4\beta^2)},$$

$$\kappa_{t4} = \frac{\vartheta_{t7}}{\gamma^2\lambda(\gamma + \lambda)^2(2\gamma + \lambda)},$$

where

$$\vartheta_{t1} = \quad 2U_0'\Big[\lambda^4 - \alpha^2\left(7\lambda^2 + 72\beta^2\right) + 48i\alpha^3\beta + 12\alpha^4 + 7\lambda^2\beta^2 + 12\beta^4$$
$$-2i\alpha\left(7\lambda^2\beta + 24\beta^3\right)\Big],$$

$$\vartheta_{t2} = -2\gamma U_0\left(\lambda^2 + 10i\alpha\beta + 5\alpha^2 - 5\beta^2\right)(\alpha' + i\beta'),$$

$$\vartheta_{t3} = \left(\lambda^3 - 4\gamma^2\lambda\right)\left(\lambda^2 - 2i\alpha\beta - \alpha^2 + \beta^2\right)^2,$$

$$\vartheta_{t4} = \quad -2U_0'[2\lambda^2 + 4\beta^2 + \alpha\left(-8i\beta + 3y\beta^2 + \lambda^2 y\right)$$
$$+\alpha^2(-4 - 3iy\beta) - y\alpha^3 + i\lambda^2 y\beta + iy\beta^3],$$

$$\vartheta_{t5} = 2U_0\,(\alpha' + i\beta')\left(-2i\beta + \alpha(-2 - 2iy\beta) - y\alpha^2 + y\beta^2 + \lambda^2 y\right)\big)\big),$$

$$\vartheta_{t6} = \gamma\left(\lambda^2 - 2i\alpha\beta - \alpha^2 + \beta^2\right)^2$$

97

$$\vartheta_{t7} = \quad 12\alpha^3 U_0' - 12i\beta^3 U_0' + \alpha^2\left[2U_0'(7\lambda + 18i\beta) - 5U_0\left(\alpha' + i\beta'\right)\right]$$

$$+\beta^2\left(-14\lambda U_0' + 5U_0\left(\alpha' + i\beta'\right)\right) + 2\alpha\left[2U_0'\left(\lambda^2 + 7i\lambda\beta - 9\beta^2\right)\right.$$

$$\left. -U_0(2\lambda + 5i\beta)\left(\alpha' + i\beta'\right)\right] - \lambda^2 U_0\left(\alpha' + i\beta'\right) + 4\lambda\beta i\lambda U_0'$$

$$+4\lambda\beta U_0\left(\beta' - i\alpha'\right).$$

The constants appearing in equation (1.68) are defined as follows:

$$\kappa_{s1} = \frac{\lambda_s\left(-2\alpha^2\left(\lambda_s^2 - \beta^2\right) + \alpha^4 + \left(\lambda_s^2 + \beta^2\right)^2\right)^2 \vartheta_{s1}}{(\gamma - \lambda_s)^2 \alpha^2 \left(\gamma\overline{\gamma}\right)^2},$$

$$\kappa_{s2} = \frac{\vartheta_{s2}}{(\gamma - \lambda_s)^2},$$

$$\kappa_{s3} = \frac{(\lambda_s - 2\alpha)^2(\lambda_s - \alpha + i\beta)^2 \vartheta_{s3}}{\alpha^2 \left(\gamma\overline{\gamma}\right)^2},$$

$$\kappa_{s4} = \frac{\lambda_s(\gamma + \lambda_s)^2 \left(\lambda_s^2 - 4\alpha^2\right)^2 \vartheta_{s4}}{\left(\gamma\overline{\gamma}\right)^2},$$

$$\kappa_{s5} = \frac{\lambda_s\left(\lambda_s^2 - 4\alpha^2\right)^2 \left(\lambda_s^2 + 2i\alpha\beta - \alpha^2 + \beta^2\right)^2 \vartheta_{s5}}{(\gamma - \lambda_s)^2 \left(\gamma\overline{\gamma}\right)^2},$$

$$\kappa_{s6} = 4\lambda_s(\gamma + \lambda_s)^2(\lambda_s - 2\alpha)^2(\lambda_s + 2\alpha)^2(\lambda_s + \overline{\gamma})^2(\lambda_s - \alpha + i\beta)^2,$$

where

$$\vartheta_{s1} = 2\lambda_s^2\alpha\beta^4\left(U_0' - yU_0\alpha'\right) - \lambda_s^2 U_0\beta^4\alpha' - 4U_0\alpha^6\left(\alpha' + 2y\beta\beta'\right)$$
$$- 8\alpha^5\beta\left(\beta\left(U_0' - yU_0\alpha'\right) + 3U_0\beta'\right) + 2U_0\left(\lambda_s^2 - 2\beta^2\right)\beta'\right)$$
$$+ U_0\alpha^4\left(\alpha'\left(\lambda_s^2 + 24\beta^2\right) + 2y\beta\left(\lambda_s^2 - 4\beta^2\right)\beta'\right)$$
$$+ 2U_0\alpha^2\beta^2\left(\lambda_s^2 y\beta\beta' - 2\alpha'\left(\lambda_s^2 - 3\beta^2\right)\right)$$
$$+ 2\alpha^3\beta\left(\beta\left(\lambda_s^2 - 4\beta^2\right)\left(U_0' - yU_0\alpha'\right)\right),$$

$$
\vartheta_{s2} = (\lambda_s^2 - 4\alpha^2)U_0'\Big[\alpha^6\left(2\beta^2 - 31\lambda_s^2\right) + 12\alpha^8 + \alpha^4\left(27\lambda_s^4 - 9\lambda_s^2\beta^2 - 34\beta^4\right)
$$

$$
+ \left(\lambda_s^2 + \beta^2\right)^2\left(\lambda_s^4 + \lambda_s^2\beta^2 - 2\beta^4\right) - \alpha^2\left(9\lambda_s^6 + 20\lambda_s^4\beta^2 + 45\lambda_s^2\beta^4 + 26\beta^6\right)\Big]
$$

$$
+ U_0\Big[\alpha\Big(20\alpha^8 - \alpha^6\left(41\lambda_s^2 + 108\beta^2\right) + \alpha^4\left(21\lambda_s^4 + \lambda_s^2\beta^2 - 156\beta^4\right)
$$

$$
+ \alpha^2\left(\lambda_s^6 + 58\lambda_s^4\beta^2 + 13\lambda_s^2\beta^4 - 36\beta^6\right) - \left(\lambda_s^2 + \beta^2\right)\left(\lambda_s^6 + 22\lambda_s^4\beta^2\right)
$$

$$
- \left(\lambda_s^2 + \beta^2\right)\left(21\lambda_s^2\beta^4 + 8\beta^6\right)\Big)\alpha' + \beta\Big(100\alpha^8 - \lambda_s^2(\lambda_s - \beta)(\lambda_s + \beta)\left(\lambda_s^2 + \beta^2\right)^2
$$

$$
\alpha^6\left(76\beta^2 - 107\lambda_s^2\right) - \alpha^4\left(15\lambda_s^4 + 69\lambda_s^2\beta^2 + 20\beta^4\right) + \alpha^2\left(23\lambda_s^6 + 66\lambda_s^4\beta^2\right)
$$

$$
+ \alpha^2(+39\lambda_s^2\beta^4 + 4\beta^6)\Big)\beta'\Big],
$$

$$
\vartheta_{s3} = 24\alpha^{10}U_0' + \lambda_s U_0\beta^4\alpha'\left(\lambda_s^2 + \beta^2\right)^2 + 2\alpha^9\left(44\lambda_s U_0' - 5U_0\alpha'\right)
$$

$$
+ 2\alpha\beta^4\left(\lambda_s^2 + \beta^2\right)\left(2U_0\alpha'\left(2\lambda_s^2 + \beta^2\right) - \lambda_s U_0'\left(\lambda_s^2 + \beta^2\right)\right)
$$

$$
+ \alpha^4\Big(-52\beta^6 U_0' - \lambda_s^5 U_0\alpha' + 6\lambda_s^3\beta^2\left(2\lambda_s U_0' + 17U_0\alpha'\right)
$$

$$
+ 2\lambda_s\beta^4\left(68U_0\alpha' - 59\lambda_s U_0'\right) - 32\lambda_s^4 U_0\beta\beta' - 44\lambda_s^2 U_0\beta^3\beta'
$$

$$
+ 10U_0\beta^5\beta'\Big) + 2\alpha^2\Big(2\lambda_s^5 U_0\beta^2\alpha' + \lambda_s\beta^6\left(11U_0\alpha'[x] - 13\lambda_s U_0'\right)
$$

$$
- 2\beta^8 U_0' + \lambda_s^3\beta^4\left(17U_0\alpha' - 9\lambda_s U_0'\right) + \lambda_s^2 U_0\beta^5\beta' - U_0\beta^7\beta'\Big)
$$

$$
+ 2\alpha^3\beta\Big(\beta\left(U_0'\left(\lambda_s^5 - 32\lambda_s^3\beta^2 - 31\lambda_s\beta^4\right) + U_0\alpha'\left(16\lambda_s^4 + 47\lambda_s^2\beta^2 + 9\beta^4\right)\right)
$$

$$
- 2\lambda_s U_0\left(\lambda_s^4 + 2\lambda_s^2\beta^2 - 3\beta^4\right)\beta'\Big) + \alpha^8\Big(2U_0'\left(63\lambda_s^2 + 2\beta^2\right)
$$

$$
- U_0\left(33\lambda_s\alpha' + 50\beta\beta'\right)\Big) + 2\alpha^7\Big(11\lambda_s U_0'\left(4\lambda_s^2 + \beta^2\right) - U_0 74\lambda_s\beta\beta'
$$

$$
+ U_0 3\alpha'\left(9\beta^2 - 7\lambda_s^2\right)\Big) + 2\alpha^6\Big(U_0'\left(15\lambda_s^4 + 17\lambda_s^2\beta^2 - 34\beta^4\right)
$$

$$
+ U_0\left(\lambda_s\alpha'\left(73\beta^2 - 13\lambda_s^2\right) - \beta\left(87\lambda_s^2 + 19\beta^2\right)\beta'\right)\Big) + 2\alpha^5\Big(U_0' 2\lambda_s^5
$$

$$
+ \left(14\lambda_s^3\beta^2 - 63\lambda_s\beta^4\right)U_0' + U_0\alpha'\left(-4\lambda_s^4 + 84\lambda_s^2\beta^2 + 39\beta^4\right)
$$

$$
- U_0 4\beta\left(13\lambda_s^3 + 9\lambda_s\beta^2\right)\beta'\Big),
$$

$$\vartheta_{s4} = -y\alpha^6 U_0' + \alpha^5 \left(U_0'(-4 + 2iy\beta) + yU_0\left(\alpha' - i\beta'\right)\right)$$

$$+ \alpha^2\left[\beta\left(U_0'\left(4i\lambda_s^2 + \beta\left(2\lambda_s^2 y + \beta(y\beta + 8i)\right)\right) + U_0\alpha'\left(2\beta(6 - iy\beta) - i\lambda_s^2 y\right)\right)\right.$$

$$\left. - U_0\beta'\left(-2i\lambda_s^2 + \lambda_s^2 y\beta + 2y\beta^3\right)\right] + \beta^2\left[\beta\left(U_0'\left(4i\lambda_s^2 + \beta\left(\lambda_s^2 y + \beta(y\beta + 6i)\right)\right)\right.\right.$$

$$\left.\left. - iU_0\alpha'\left(\lambda_s^2 y + \beta(y\beta + 2i)\right)\right) - U_0\beta'\left(2i\lambda_s^2 + \beta\left(\lambda_s^2 y + \beta(y\beta + 4i)\right)\right)\right]$$

$$+ \alpha\beta\left(\lambda_s^2\beta\left(2U_0' - yU_0\left(\alpha' - i\beta'\right)\right) + 2iy\beta^4 U_0' - 4i\lambda_s^2 U_0\alpha'\right.$$

$$+ \beta^3\left(-8U_0' + yU_0\left(\alpha' - i\beta'\right)\right) + 4U_0\beta^2\left(\beta' - i\alpha'\right)\Big)$$

$$+ \alpha^4\left(U_0'\left(\lambda_s^2 y + \beta(-y\beta + 2i)\right) + U_0\left(\alpha'(2 - iy\beta) - \beta'(y\beta + 4i)\right)\right)$$

$$+ \alpha^3\left(U_0\left(\alpha'\left(-\lambda_s^2 y + 2\beta(y\beta + 2i)\right) + i\beta'\left(4i\beta - 2y\beta^2 + \lambda_s^2 y\right)\right)\right.$$

$$\left. + 2U_0'\left(\lambda_s^2 - 6\beta^2 + 2iy\beta^3\right)\right),$$

$$\vartheta_{s5} = -y\alpha^6 U_0' + \alpha^5 \left(U_0'(-4 - 2iy\beta) + yU_0\left(\alpha' + i\beta'\right)\right) + \alpha^2\Big($$

$$\beta\left(U_0'\left(\beta\left(2\lambda_s^2 y + \beta(y\beta - 8i)\right) - 4i\lambda_s^2\right) + U_0\alpha'\left(2\beta(6 + iy\beta) + i\lambda_s^2 y\right)\right)$$

$$- U_0\beta'\left(2i\lambda_s^2 + \lambda_s^2 y\beta + 2y\beta^3\right)\Big) + \beta^2\Big(\beta\left(U_0'\left(\beta\left(\lambda_s^2 y + \beta(y\beta - 6i)\right) - 4i\lambda_s^2\right)\right.$$

$$\left. + U_0\alpha'\left(\beta(2 + iy\beta) + i\lambda_s^2 y\right)\right) - U_0\beta'\left(\beta\left(\lambda_s^2 y + \beta(y\beta - 4i)\right) - 2i\lambda_s^2\right)\Big)$$

$$+ \alpha\beta\Big(\lambda_s^2\beta\left(2U_0' - yU_0\left(\alpha' + i\beta'\right)\right) + 4i\lambda_s^2 U_0\alpha' - 2iy\beta^4 U_0'$$

$$+ \beta^3\left(-8U_0' + yU_0\left(\alpha' + i\beta'\right)\right) + 4U_0\beta^2\left(\beta' + i\alpha'\right)\Big)$$

$$+ \alpha^4\left(U_0'\left(\lambda_s^2 y - \beta(y\beta + 2i)\right) + U_0\left(\alpha'(2 + iy\beta) + \beta'(-y\beta + 4i)\right)\right)$$

$$+ \alpha^3\Big(2U_0'\left(\lambda_s^2 - 6\beta^2 - 2iy\beta^3\right) - U_0\alpha'\left(4i\beta(x) - 2y\beta(x)^2 + \lambda_s^2 y\right)$$

$$+ U_0\beta'\left(-4\beta(x) + 2iy\beta(x)^2 - i\lambda_s^2 y\right)\Big).$$

# Bibliography

[1] Mehmet Bilgili, Arif Ozbek, Besir Sahin, and Ali Kahraman. An overview of renewable electric power capacity and progress in new technologies in the world. *Renewable and Sustainable Energy Reviews*, 49:323 – 334, 2015.

[2] Arthur Pecher and Jens Peter Kofoed. *Handbook of ocean wave energy*. Springer International Publishing, first edition.

[3] Joao Cruz. *Ocean Wave Energy: Current Status and Future Prespectives*. Springer-Verlag Berlin Heidelberg, first edition.

[4] R. Bhattacharyya and M.E. McCormick. Chapter 1 - introduction. In R. Bhattacharyya and M.E. McCormick, editors, *Wave Energy Conversion*, volume 6 of *Elsevier Ocean Engineering Series*, pp. 1 – 6. Elsevier, 2003.

[5] Gunnar Mørk, Stephen Barstow, Alina Kabuth, and M. Teresa Pontes. Assessing the global wave energy potential, 2010. ASME. International Conference on Offshore Mechanics and Arctic Engineering, 29th International Conference on Ocean, Offshore and Arctic Engineering: Volume 3 .

[6] World Energy Council. World energy resource, marine energy, 2016.

[7] Andrew M. Cornett. A global wave energy resource assessment, in: Proceedings of the eighteenth international offshore and polar engineering conference, Vancouber, 2008.

[8] S. H. Salter. Wave power. *Nature*, 249:720 EP –, Jun 1974.

[9] Eugen Rusu and Florin Onea. A review of the technologies for wave energy extraction. *Clean Energy*, 2(1):10–19, 2018.

[10] Hosna Titah-Benbouzid and Mohamed Benbouzid. An up-to-date technologies review and evaluation of wave energy converters. *International Review of Electrical Engineering (IREE)*, 10(1), 2015. doi:10.15866/iree.v10i1.5159.

[11] António F. de O. Falcão. Wave energy utilization: A review of the technologies. *Renewable and Sustainable Energy Reviews*, 14(3):899 – 918, 2010.

[12] M. Dolores Esteban, José-Santos López-Gutiérrez, Vicente Negro, Marcelo Lavi na, and Pedro Mu noz Sánchez. A new classification of wave energy converters used for selection of devices. *Journal of Coastal Research: Special Issue 85 - Proceedings of the 15th International Coastal Symposium*, pp. 1286–1290, 2018.

[13] M. Dolores Esteban, José-Santos López-Gutiérrez, and Vicente Negro. Classification of wave energy converters. *Recent Adv Petrochem Sci*, 2(4):555593, 2017.

[14] Iraide López, Jon Andreu, Salvador Ceballos, Iñigo Martínez de Alegría, and Iñigo Kortabarria. Review of wave energy technologies and the necessary power-equipment. *Renewable and Sustainable Energy Reviews*, 27:413 – 434, 2013.

[15] S H Salter, J R M Taylor, and N J Caldwell. Power conversion mechanisms for wave energy. *Proceedings of the Institution of Mechanical Engineers, Part M: Journal of Engineering for the Maritime Environment*, 216(1):1–27, 2002.

[16] M. S. Lagoun, A. Benalia, and M. E. H. Benbouzid. Ocean wave converters: State of the art and current status. In *2010 IEEE International Energy Conference*, pp. 636–641, Dec 2010.

[17] L. Szabo, C. Oprea, I. Viorel, and K. A. Biro. Novel permanent magnet tubular linear generator for wave energy converters. In *2007 IEEE International Electric Machines Drives Conference*, volume 2, pp. 983–987, May 2007.

[18] Henk Polinder, Markus Mueller, Mattia Scuotto, and M. Goden de Sousa Prado. Linear generator systems for wave energy conversion. In *Proceedings of the 7th European Wave and Tidal Energy Conference, Porto, Portugal.*, 2007.

[19] N. Hodgins, O. Keysan, A. S. McDonald, and M. A. Mueller. Design and testing of a linear generator for wave-energy applications. *IEEE Transactions on Industrial Electronics*, 59(5):2094–2103, May 2012.

[20] Panagiotis E. Kakosimos, Evangelos M. Tsampouris, Nikolaos M. Kimoulakis, and Antonios Kladas. Overview of the alternative topologies of linear generators in wave energy conversion systems. In *Applied Electromagnetic Engineering for Magnetic, Superconducting and Nano Materials*, volume 721 of *Materials Science Forum*, pp. 281–286. Trans Tech Publications, June 2012.

[21] Matteo Bachetti, Marina M. Romanova, Akshay Kulkarni, Luciano Burderi, and Tiziana di Salvo. Qpo emission from moving hot spots on the surface of neutron stars: a model. *Monthly Notices of the Royal Astronomical Society*, 403(3):1193–1205, 2010.

[22] M. M. Romanova, G. V. Ustyugova, A. V. Koldoba, J. V. Wick, and R. V. E. Lovelace. Three-dimensional simulations of disk accretion to an inclined dipole. i. magneto-spheric flows at different . *The Astrophysical Journal*, 595(2):1009, 2003.

[23] V.R. Malghan. History of mhd power plant development. *Energy Conversion and Management*, 37(5):569 – 590, 1996.

[24] D. G. Elliott. Direct current liquid-metal magnetohydrodynamic power generation. *AIAA Journal*, 4(4):627–634, Apr 1966.

[25] H. Branover and S. Claesson. MHD systems for converting solar energy into electricity. *Chem. Scripta*, 19:209–223, 1982.

[26] Antoine Alemany, Armands Krauze, and Mahmoud AL Radi. Thermo acoustic - MHD electrical generator. *Energy Procedia*, 6:92 – 100, 2011.

[27] Baolin Liu, Jian Li, Yan Peng, Lingzhi Zhao, Ran Li, Qi Xia, and Ciwen Sha. Performance study of magnetohydrodynamic generator for wave energy. 24th International Offshore and Polar Engineering Conference, ISOPE, Busan, Korea, 15-20 June, 2014, pp. 545-548.

[28] L. Hu, H. Kobayashi, and Y. Okuno. Performance of a liquid metal mhd power generation system for various external forces. 12th International Energy Conversion Engineering Conference, American Institute of Aeronautics and Astronautics Inc., Cleveland, Ohio, USA, 2014.

[29] G. W. Swift. A liquidmetal magnetohydrodynamic acoustic transducer. *The Journal of the Acoustical Society of America*, 83(1):350–361, 1988.

[30] Antoine Alemany and Seyyed Mohammad Mirhoseini. Analytical study of thermoacoustic MHD generator. *Magnetohydrodynamics*, 51(3):519–530, 2015.

[31] A. A. Castrejn-Pita and G. Huelsz. Heat-to-electricity thermoacoustic-magnetohydrodynamic conversion. *Applied Physics Letters*, 90(17):174110, 2007.

[32] Cédric Vogin and Antoine Alemany. Analysis of the flow in a thermo-acoustic mhd generator with conducting walls. *European Journal of Mechanics - B/Fluids*, 26(4):479 – 493, 2007.

[33] Rynne Timothy M. Ocean wave energy conversion system, U.S Patent 5136173, Aug 04, 1992.

[34] Robert A. Koslover. Modular liquid-metal magnetohydrodynamic (LMMHD) power generation cell, U.S Patent 7166927B2, Jul 2005.

[35] Jian Li, Yan Peng, Baolin Liu, Ciwen Sha, Lingzhi Zhao, Yuyu Xu, Ran Li, and Xuelin Li. Analysis of liquid metal MHD wave energy direct conversion system. 18th International Offshore and Polar Engineering Conference, ISOPE, Vancouber, Canada, 06-1 July, 2008, pp. 388-392.

[36] Jian Li, Yan Peng, Baolin Liu, Ciwen Sha, Lingzhi Zhao, Yuyu Xu, Ran Li, and Xuelin Li. Preliminary experimental study on LMMHD wave energy conversion system. 20th International Offshore and Polar Engineering Conference, ISOPE, Beijing, China, 20-25 June, 2010, pp. 907-910.

[37] A. Khaligh and O.C. Onar. *Energy Harvesting: Solar, Wind, and Ocean Energy Conversion Systems*. Energy, Power Electronics, and Machines. CRC Press, 2009.

[38] L. Z. Zhao, H. L. Ye, A. W. Peng, Q. H. Zhang, Q. Xia, B. L. Liu, J. Li, F. Wang, and R. Li. MHD wave energy underwater recharging platforms for auvs. 26th International Ocean and Polar Engineering Conference, ISOPE, Rhodes, Greece, 26 June-2 July, 2016, pp. 480-483.

[39] Qinghe Zhang, Qi Xia, Aiwu Peng, and Lingzhi Zhao. Design of PCS for MHD wave energy underwater recharging platforms. 26th International Ocean and Polar Engineering Conference, ISOPE, Rhodes, Greece, 26 June-2 July, 2016, pp. 484-490.

[40] Angélica Felix, Edgar Mendoza, Valeria Chávez, Rodolfo Silva, and Germán Rivillas-Ospina. Wave and wind energy potential including extreme events: A case study of mexico. *Journal of Coastal Research: Special Issue 85 - Proceedings of the 15th International Coastal Symposium*, pp. 1336–1340, 2018.

[41] P. A. Davidson. *An Introduction to Magnetohydrodynamics*. Cambridge Texts in Applied Mathematics. Cambridge University Press, 2001.

[42] U. Müller and L. Bühler. *Magnetofluiddynamics in Channels and Containers*. Springer, 2001.

[43] H. K. Moffatt and J. Toomre. The annihilation of a two-dimensional jet by a transverse magnetic field. *Journal of Fluid Mechanics*, 30(1):6582, 1967.

[44] Guillermo Ibez, Sergio Cuevas, and Mariano Lpez de Haro. Optimization analysis of an alternate magnetohydrodynamic generator. *Energy Conversion and Management*, 43(14):1757 – 1771, 2002.

[45] L. Gary Leal. *Advanced Transport Phenomena: Fluid Mechanics and Convective Transport Processes*. Cambridge Series in Chemical Engineering. Cambridge University Press, 2007.

[46] H. Perales. *Numerical study of oscillatroy flows in ducts*. PhD thesis, Facultad de Ciencias, Universidad Autónoma del Estado de Morelos, México, Appril 2003, (in Spanish).

[47] H. Schlichting. *Boundary-Layer Theory*. McGraw-Hill, 7th edition, 1979.

[48] N Riley. Steady streaming. *Annual Review of Fluid Mechanics*, 33(1):43–65, 2001.

[49] Irwin S. Goldberg, Zongqin Zhang, and Minhtan Tran. Steady streaming of fluid in the entrance region of a tube during oscillatory flow. *Physics of Fluids*, 11(10):2957–2962, 1999.

[50] A. Gopinath. Steady streaming due to small-amplitude superposed oscillations of a sphere in a viscous fluid. *The Quarterly Journal of Mechanics and Applied Mathematics*, 47(3):461–480, 1994.

[51] J. T. Stuart. Double boundary layers in oscillatory viscous flow. *Journal of Fluid Mechanics*, 24(4):673687, 1966.

[52] S. Cuevas and E. Ramos. Steady streaming in oscillatory viscous flow under a transverse magnetic field. *Physics of Fluids*, 9(5):1430–1434, 1997.

[53] Tao Zhou, Hongli Chen, and Zhiyi Yang. Effect of fringing magnetic field on magnetohydrodynamic flow in rectangular duct. *Fusion Engineering and Design*, 86(9):2352 – 2357, 2011. Proceedings of the 26th Symposium of Fusion Technology (SOFT-26).

[54] A. Sterl. Numerical simulation of liquid-metal mhd flows in rectangular ducts. *Journal of Fluid Mechanics*, 216:161191, 1990.

[55] W.F. Hughes and F.J. Young. *The Electromagnetodynamics of Fluids*. Wiley, 1966.

[56] Yasushi Takeda. Measurement of velocity profile of mercury flow by ultrasound doppler shift method. *Nuclear Technology*, 79(1):120–124, 1987.

[57] A. Cramer, C. Zhang, and S. Eckert. Local flow structures in liquid metals measured by ultrasonic doppler velocimetry. *Flow Measurement and Instrumentation*, 15(3):145 – 153, 2004.

[58] Helmhotz Zentrum Dresden Rossendorf. Ultrasonic Doppler Velocimetry: https://www.hzdr.de/db/Cms?pOid=55354&pNid=226&pLang=en.

[59] Gabriel Ruiz, Edgar Mendoza, Rodolfo Silva, Gregorio Posada, Dulce Pérez, Germán Rivillas, Edgar Escalante, and Francisco Ruiz. Caracterización del régimen de oleaje y viento de 1948-2007 en el litoral mexicano. *Fundación para el Fomento de la Ingeniería del Agua*, 16(1):51–64, 2009.

[60] Gabriel Ruiz, Rodolfo Silva, Germán Rivillas, Gregorio Posada, Dulce Pérez, and Edgar Mendoza. Atlas de clima marítimo para las vertientes atlántica y pacífica del litoral mexicano. In *XXIII congreso latinoamericano de hidrulica*, 2008.

[61] S.A. Signal Processing. Dop 3000/3010 user manual, 2015. http://www.signal-processing.com.

[62] J. Yeager and J.F. Keithley. *Low Level Measurements: Precision DC Current, Voltage, and Resistance Measurements*. Keithley Instruments, 1998.

[63] L. Zhao, Y. Peng, C. Sha, R. Li, Y. Xu, B. Liu, and J. Li. End effect of liquid metal magnetohydrodynamic generator in wave energy direct conversion system. In *2009 International Conference on Sustainable Power Generation and Supply*, pp. 1–6, April 2009.